Microtechnology for In-vitro Ultrasound Neuromodulation Studies

MICROTECHNOLOGY FOR IN-VITRO ULTRASOUND NEUROMODULATION STUDIES

Dissertation

for the purpose of obtaining the degree of doctor
at Delft University of Technology,
by the authority of the Rector Magnificus prof. dr. ir. T.H.J.J. van der Hagen,
chair of the Board for Doctorates,
to be defended publicly on
Monday 24 March 2025 at 10:00 o'clock

by

Gandhika K. WARDHANA

Master of Science in Electrical Engineering,
Delft University of Technology, Delft, the Netherlands,
born in Bekasi, Indonesia.

This dissertation has been approved by the promotors.

Composition of the doctoral committee:

Rector Magnificus,	Chairperson
Dr. M. Mastrangeli,	Delft University of Technology, promotor
Dr. T.L. Costa,	Delft University of Technology, copromotor

Independent members:

Prof. dr. ir. W.A. Serdijn,	Delft University of Technology
Prof. dr. ir. R. Dekker,	Delft University of Technology
Dr. A.S. Savoia,	Roma Tre University
Dr. J. Meents,	Multi Channel Systems GmbH
Dr. J.P. Frimat,	Leiden University Medical Center
Prof. dr. P.J. French,	Delft University of Technology, reserve member

Keywords: ultrasound neuromodulation, piezoelectric ultrasound transducer, transducer efficiency, acoustic anti-reflective structure, acoustic lens.

Printed by: Johannes Gutenberg

Front & Back: Maede Shakeri

ISBN 978-94-6384-760-5

An electronic version of this dissertation is available at
http://repository.tudelft.nl/.

In the memory of Padma Widiawana, whose memory lives on these pages, and to my beloved Bernadette Melani, whose support and understanding made them possible.

CONTENTS

LIST OF FIGURES

LIST OF TABLES

SUMMARY

Brain disorders are a major cause of disability, and current treatments like pharmacological interventions and deep brain stimulation (DBS) have limitations, including side effects, limited efficacy, and invasiveness. Ultrasound neuromodulation is a non-invasive technique for stimulating neural activity and providing therapeutic intervention using ultrasound waves. Although ultrasound has been empirically proven effective in neuromodulation, its underlying mechanisms of action remain partially unclear. *In vitro* models, such as 2D and 3D cell cultures, are valuable for studying the mechanisms of ultrasound neuromodulation and optimizing stimulation parameters. However, conventional handheld ultrasound transducers and *in vitro* platforms are not ideally suited for this purpose due to incompatible sizes and undesirable acoustic reflections. Furthermore, efforts in miniaturizing piezoelectric ultrasound transducers, the most common transducer type used in ultrasound neuromodulation, still suffer from high inefficiency in the generation of ultrasound and have limited spatial resolution. This thesis presents novel microfabrication techniques to address these challenges, focusing on improving the performance of piezoelectric ultrasound transducers (PUTs) integrated on application-specific integrated circuits (ASICs) and minimizing acoustic reflection from the *in vitro* platform.

To enhance the transmit efficiency of PUTs on the silicon substrate typically found in ASICs, an integrated air-backing layer was incorporated into the silicon substrate. This air-backing layer, achieved through selective thinning of the silicon beneath the transducers, resulted in a significant improvement in output intensity. The optimal membrane thickness was determined to be 20 μm, balancing improved output intensity with mechanical stability.

A novel polymer-metal connection (PMC) method was developed to implement an acoustically-transparent top connection for the PUTs. This approach utilizes a microfabricated PDMS/Ti/Al membrane supported by a silicon frame, replacing traditional top connections that introduce significant acoustic losses. The PMC preserved 80% of the output intensity compared to an ideal reference, significantly outperforming conventional aluminum foil connections.

To further enhance focusing capabilities, a miniaturized Fresnel-zone plate (FPZP) lens was fabricated from PDMS using a single photolithography step. This approach enables precise control over lens geometry and acoustic properties, leading to improved focusing resolution compared to conventional methods. The fabricated FPZP lens demonstrated a focal gain of 19.95 dB and a high focusing resolution, thus enabling high-frequency ultrasound generation is suitable for *in vitro* ultrasound neuromodulation studies.

To address the challenge of acoustic reflection from conventional *in vitro* platforms, an anti-reflective microengineered substrate (ARMS) was proposed. This design incorporates an array of pillars at the interface between two polymer layers to distribute and reduce the amplitude of reflected waves. Simulations showed that the optimized ARMS

design significantly reduced echo amplitude and preserved stimulation signal fidelity compared to conventional glass substrates.

The combination of the advancements in piezoelectric transducer technology and acoustic design described in this thesis holds promise for improving the performance and versatility of *in vitro* ultrasound neuromodulation platforms. The development of miniaturized, efficient transducers and anti-reflective substrates could enable more precise and reliable stimulation of neural tissue, facilitating further research into the mechanisms and applications of ultrasound neuromodulation.

SAMENVATTING

Hersenaandoeningen zijn een belangrijke oorzaak van invaliditeit, en huidige behandelingen zoals farmacologische interventies en deep brain stimulation (DBS, diepe hersenstimulatie) hebben beperkingen, waaronder bijwerkingen, beperkte werkzaamheid en invasiviteit. Ultrasone neuromodulatie is een niet-invasieve techniek voor het stimuleren van neurale activiteit en het bieden van therapeutische interventie met behulp van ultrasone golven. Hoewel ultrasound empirisch bewezen effectief is in neuromodulatie, blijven de onderliggende werkingsmechanismen gedeeltelijk onduidelijk. In vitro modellen, zoals 2D- en 3D-celculturen, zijn waardevolle hulpmiddelen voor het bestuderen van de mechanismen van ultrasound neuromodulatie en het optimaliseren van stimulatieparameters. Conventionele ultrasound transducers en *in vitro* platforms zijn echter niet ideaal voor dit doel. Dit proefschrift presenteert nieuwe microfabricagetechnieken om deze uitdagingen aan te gaan, met de focus op het verbeteren van de prestaties van piëzo-elektrische ultrasound transducers (PUTs) geïntegreerd op applicatiespecifieke geïntegreerde schakelingen (ASICs) en het minimaliseren van akoestische reflectie van het *in vitro* platform.

Om de transmissie-efficiëntie van PUTs op silicium te verbeteren, werd een geïntegreerde luchtlaag in het siliciumsubstraat opgenomen. Deze luchtlaag, verkregen door selectieve verdunning van het silicium onder de transducers, resulteerde in een significante verbetering van de zendintensiteit. De optimale membraandikte werd bepaald op 20 μm, waarbij een balans werd gevonden tussen verbeterde zendintensiteit en mechanische stabiliteit.

Er werd een nieuwe polymeer-metaalverbindingsmethode (PMC) ontwikkeld om een akoestisch transparante topconnectie voor de PUTs te implementeren. Deze aanpak maakt gebruik van een microgefabriceerd PDMS/Ti/Al-membraan, ondersteund door een siliciumframe, ter vervanging van traditionele topconnecties die aanzienlijke akoestische verliezen introduceren. De PMC behield 80% van de zendintensiteit in vergelijking met een ideale referentie, wat aanzienlijk beter presteert dan conventionele aluminiumfolie-verbindingen.

Om de focusseringscapaciteit verder te verbeteren, werd een geminiaturiseerde Fresnel-zoneplaatlens (FPZP) vervaardigd uit PDMS doormiddel van een enkele fotolithografiestap. Deze aanpak maakt precieze controle over de lensgeometrie en akoestische eigenschappen mogelijk, wat leidt tot een verbeterde focusseerresolutie in vergelijking met conventionele methoden. De gefabriceerde FPZP-lens vertoonde een focale versterking van 19,95 dB en een hoge focusseerresolutie, waardoor deze geschikt is voor hoogfrequente ultrasoundtoepassingen.

Om de uitdaging van akoestische reflectie van conventionele *in vitro* platforms aan te pakken, werd een antireflecterend microgeconstrueerdsubstraat (ARMS) voorgesteld. Dit ontwerp bevat een reeks pilaren op het grensvlak tussen twee polymeerlagen om de amplitude van gereflecteerde golven te verdelen en te verminderen. Simulaties toon-

den aan dat het geoptimaliseerde ARMS-ontwerp de echo-amplitude aanzienlijk verminderde en de getrouwheid van het stimulatiesignaal behield in vergelijking met conventionele glassubstraten.

De combinatie van de ontwikkelingen in piëzo-elektrische transducertechnologie en akoestisch ontwerp die in dit proefschrift worden beschreven, belooft de prestaties en veelzijdigheid van *in vitro* ultrasound neuromodulatieplatforms te verbeteren. De ontwikkeling van geminiaturiseerde, efficiënte transducers en antireflecterende substraten zou een preciezere en betrouwbaardere stimulatie van neuraal weefsel mogelijk kunnen maken, wat verder onderzoek naar de mechanismen en toepassingen van ultrasound neuromodulatie faciliteert.

1

Introduction

Tiger got to hunt, bird got to fly;
man got to sit and wonder, 'Why, why, why?'
Tiger got to sleep, bird got to land;
man go to tell himself he understand.

Kurt Vonnegut

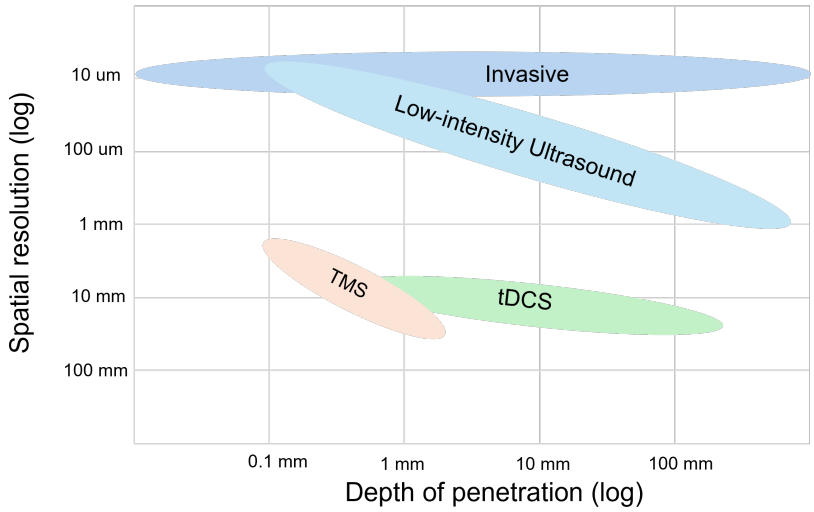

Figure 1.1: Graph showing the spatial resolution and depth penetration of different brain stimulation techniques [9], [10], [11], [12].

1.1. ULTRASOUND NEUROMODULATION

Despite recent advances in neuroscience, the complex network of communciating systems within the human brain is still largely unknown. Embedded within the complexity of the brain, brain disorders (BD) are one of the major causes of disability and loss of life. While pharmacological treatments have been the cornerstone of modern medicine, there are side effects resulting from their non-targeted nature, and limited efficacy due to the largely impermeable blood-brain barrier. Electronic-based or bioelectronic medicine, such as deep brain stimulation (DBS), offers a localized therapy for BD by delivering the treatment only to the required brain region. DBS has shown great efficacy for BD such as Parkinson's disease [1] and epilepsy [2], while reducing the dosage of pharmaceutical drug intake, and, consequently, reducing side-effects. However, DBS requires invasive surgery and carries risks, which necessitate careful evaluation, and limit its accessibility to patients [3],[4]. More accessible treatments for BD are being explored through non-invasive bioelectronic medicine utilizing magnetic [5] and electric fields [6], and focused ultrasound [7]. The use of focused ultrasound in particular has shown great promise due to its advantageous combination of high spatial resolution and depth of stimulation compared to other non-invasive modalities (Figure 1.1). Investigations have been reported in animal models and humans primarily in the form of transcranial focused ultrasound stimulation (tFUS), in which an ultrasound wave is applied through the skull with a specific waveform.

Despite the evidence for successful neuromodulation performed by focused ultrasound stimulation (FUS) across the literature [8], there still remain unknowns in the field limiting its potential for clinical application. Firstly, there is still no consensus on the optimal ultrasound waveform parameters, both in the time and amplitude domain [8]. In

human applications, the complexity and safety requirements of the experimental procedure limit the exploration of the optimal stimulation parameters. On the other hand, ultrasound-induced responses are typically obtained via recording modalities such as functional magnetic resonance imaging (fMRI) [13] and electroencephalogram (EEG) [14]. However, these global recording modilities limit the understanding of the effects of the ultrasound waveform parameters at the cellular level. In contrast, animal studies involving rats and monkeys offer more flexibility, albeit with potential translational challenges due to physiological differences with humans [15]. Notably, experiments utilizing anesthesia have indicated undesired effects on the experimental outcomes [16]. In addition, using sub-MHz ultrasound in rodents to mimic the frequency used in human studies can lead to unreliable functional and behavioral responses [17]. The resulting axial resolution of approximately 1-2 centimeters is acceptable in humans, whereas in rodents, this represents more than the entire depth of the brain [18]. *In vitro* models offer an alternative and valuable platform to delve into optimal parameters for ultrasound neuromodulation with significance towards human translation [19]. They allow for studies in human-derived neurons and organoids, where ultrasound parameters can be explored with fewer constraints and high-fidelity recordings can be obtained with high throughput [20]. However, progress in *in vitro* ultrasound neuromodulation research has encountered several challenges, which are described in the next sub-section.

1.1.1. CHALLENGES IN *in vitro* ULTRASOUND NEUROMODULATION

MINIATURIZED ULTRASOUND TRANSDUCERS

Conventional commercially-available transducers, often designed as handheld devices, pose challenges for inclusion within setups with confined spaces such as *in vitro* setups including microplates, microelectrode arrays (MEAs), and fluorescence microscope systems (Figure 1.2). The compatibility with the standard *in vitro* format is important in order to facilitate a large volume of research in the pre-clinical stage of treatment development. Previous attempts utilizing commercial ultrasound transducers required a bulky adaptation structure for positioning and manipulation of the transducer, thereby restricting experimental versatility to a singular setup or recording modality [21],[22]. Another challenge is to prevent cross-sensitivity of the cells to the electric field generated to drive the ultrasound transducer, which can confound the outcome of the experiment [23].

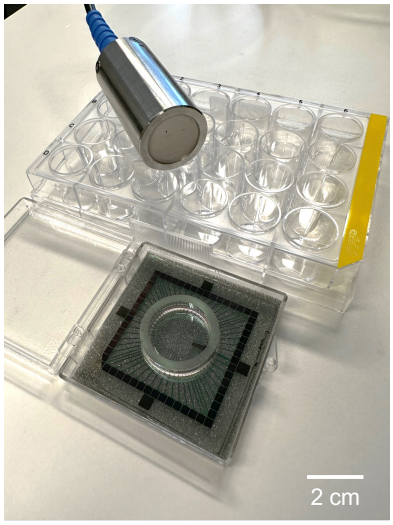

Figure 1.2: Size comparison of a commercial focused ultrasound transducer with typical *in vitro* platforms.

Advancing the field of *in vitro* ultrasound neuromodulation would ideally require

1

ultrasound transducers with compact form factor and high output efficiency, defined as the focal pressure-per-volt applied to the transducer, such that the required acoustic pressures can be achieved with low driving voltages, hence minimizing the risks of cross-sensitivity. There are three ultrasound transducer technologies when considering the landscape of miniaturized ultrasound transducers: piezoelectric ultrasound transducers (PUTs), capacitive micromachined ultrasound transducers (CMUTs), and piezoelectric micromachined ultrasound transducers (PMUTs) (Figure 1.3).

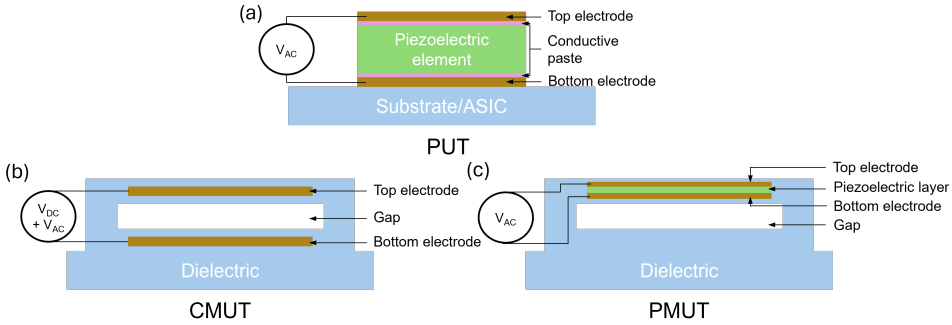

Figure 1.3: Simplified schematics of miniaturized ultrasound technologies: (a) Piezoelectric ultrasound transducers, alternating electric potential applied across the piezoelectric element through electrodes placed on two opposing sides. (b) CMUT consists of a dielectric membrane suspended over a cavity. Electrodes are positioned in the membrane and on the bottom of the cavity. An Electric field is applied across the electrode, causing movement of the membrane through electrostatic force. A direct current bias voltage is used to bring the membrane into collapse mode, and an alternating current voltage is used to generate the ultrasound wave. (c) PMUT, a piezoelectric membrane, is used instead of a dielectric membrane of a CMUT. Electric potential is directly applied to the piezoelectric membrane to actuate the membrane movement, thus eliminating the need for a bias voltage.

CMUTs have been developed in the past three decades and can be considered as the newer technology compared to piezoelectric transducers [24]. CMUTs have a clear competitive edge in miniaturization due to their complementary metal oxide semiconductor (CMOS)-compatible manufacturing process. By utilizing microfabrication technology, small transducers on a micrometer scale can be fabricated with high accuracy and high throughput. The performance of the transducer can be tailored by adjusting design parameters such as material choice, membrane dimensions, and gap size. Another advantage of CMUTs is their low Q-factor, which corresponds to a wide bandwidth. This characteristic is highly desirable in ultrasound imaging for producing sharp images. However, CMUTs have several drawbacks, namely, the need for high bias voltage and low transmit efficiency [24], [25]. The operation of CMUTs requires a high bias voltage to operate the device, which typically ranges from tens of volts to 200 V [25],[26]. The need for bias voltage limits the use of CMUTs in an application that has limited power supply voltages. Research of pre-charged CMUTs that circumvent this drawback has been shown in the literature [25]. Pre-charging was achieved by trapping electrical charge in a layer of Al_2O_3 placed above the bottom electrode [25]. In applications that require a reasonably high output pressure (e.g. neuromodulation, tissue ablation) or with limited power supply (e.g. wearable or implantable devices), a transducer with high transmit

efficiency and low loss is preferred. In these cases, the inherent damping characteristic of CMUTs, associated with their low Q-factor, is not ideal. Additionally, the reliability of CMUTs is a concern, as they consist of micrometer-thick membranes that are susceptible to damage and degradation over time [27].

PMUTs addressed the need for high bias voltage in CMUTs by using a piezoelectric effect to move the flexural membrane instead of electrostatic force [28]. Instead of a dielectric material, a piezoelectric material is incorporated into the membrane. AC voltage applied across the piezoelectric membrane causes the vibration that generates acoustic waves (Figure 1.3). The performance of PMUTs is determined by the membrane parameters and, more importantly, the choice of piezoelectric material [28]. A piezoelectric material is characterized by its coupling factor, which denotes the efficiency of conversion from electric energy to mechanical energy or vice versa. Lead zirconate titanate (PZT) based PMUTs have been shown to exhibit a high transmit efficiency [28], [29]. The use of a 2% Niobium doping in a sol-gel PZT-based PMUT was reported to yield an output efficiency of 30 kPa/V at 20 mm distance [29]. However, their fabrication using a sol-gel method is challenging and requires a poling process which causes a low yield and uniformity [28],[30]. Aluminum nitride (AlN) based PMUTs offer a CMOS-compatible process of PMUT at the cost of performance, especially in transmit efficiency due to the low piezoelectric coupling factor of AlN [28], [31]. Unlike PZT, AlN can be sputtered on a substrate and does not require a poling process [32]. To address the low transmit efficiency of AlN PMUTs, scandium was used as a dopant to improve the coupling factor of AlN in PMUTs. However, the transmit efficiency was still far below PZT-based PMUTs with an output efficiency of 12 kPa/V at 1.9 mm distance [31].

Compared to micromachined ultrasound transducers, PUTs are the more conventional transducer technology. PUTs utilize the bulk deformation of a piezoelectric material under an electrical field to generate ultrasound waves (Figure 1.3). Unlike PMUTs that typically use <10um-thick piezoelectric membrane, the thickness of PUTs ranges from a submillimeter to a few millimeters, depending on its frequency [33], [34]. At present, PUTs still offer better transmit efficiency compared to PMUTs and CMUTs [24], [28]. The fabrication of bulk piezoelectric elements used in PUTs have reached commercial maturation and are available in various configurations. This contrasts with MUTs, which require careful and expensive optimization of the membrane parameters to produce various ultrasound parameters, and its commercial availability is still limited to a few foundries. PUTs have been the industry standard for decades and can be found in most medical facilities as a safe and affordable imaging tool in the form of a handheld device. Several implementations of miniaturized PUTs have been used in clinics, such as intravascular ultrasound (IVUS) catheter [35] and intra-cardiac echo (ICE) probe [36]. The implementations of PUTs on application-specific integrated circuits (ASIC) have been shown for imaging applications [37], [38]. However, the technology developed for imaging transducers is typically optimized for wide bandwidth sacrifice transmit efficiency. Several works have demonstrated PUTs with output efficiency as high as 80 kPa/V at 15mm distance [39] and 160 kPa/V at 1 mm distance [40]. Both works were implemented on a flexible substrate. This efficiency was not yet reflected in PUTs on ASIC, which showed a transmit efficiency of 6 kPa/V [34] and 20 kPa/V [33]. Although, in theory, the output pressure range of PUTs can be extended with higher output voltage,

this is limited by the size and technology of the ASIC. When considering the efficiency and the ease of customizability, PUTs are the suitable technology for ultrasound neuromodulation study. However, its implementation on ASIC still needs to be improved in terms of transmit efficiency.

PRESERVING STIMULATION FIDELITY

Another challenge that needs to be addressed is the preservation of the stimulation waveform fidelity during the experiment [22]. Most *in vitro* and *ex vivo* setups comprise cells or tissue slices on a rigid substrate in a confined well typically made of polystyrene or glass. In contrast, ultrasound transducers are characterized in a large water tank to map their acoustic beam profile. Although the culturing well can be made large enough to reduce the impact on the fidelity of the ultrasound waves, the use of a hard substrate cannot be avoided in most cases [22]. Polystyrene and glass have an acoustic impedance that is highly mismatched to a liquid medium [22], [21]. An interface of two materials with highly mismatched acoustic impedance will cause a non-negligible reflection of waves that can interfere with the incoming waves. This interference can cause an incorrect correlation between stimulation parameters and the biological response. Prediction of the actual stimulation parameters in the presence of interference due to the substrate can be made in order to improve the stimulus-response correlation [21]. However, this necessitates complex models that require expertise and access to certain computational resources. Another approach is to minimize the reflection from the substrate by culturing cells on a thin film placed on top of water, thus having the cells positioned between two liquid media, the culture medium and water [19]. However, there is a practical limit on the amount of medium within the setup and reflection will still occur on the interface with either the container or air. Therefore, the efficacy of this approach is determined by the amount of medium past the cells to allow for the reflected wave to dissipate before reaching back to the cells. Additionally, this approach requires a dedicated setup that is unconventional in a typical medical research facility. In order to have a more inclusive platform to disseminate ultrasound neuromodulation research, anti-reflection strategies have to be implemented in a standard *in vitro* research platform.

1.2. MAIN QUESTION AND THESIS OBJECTIVES

This thesis aims to answer the following question: **How to create a focused ultrasound neuromodulation device seamlessly integrated into standard *in vitro* platforms?**.

To achieve this goal, two main components will be addressed: the transducer and the substrate for the cell culture. PUTs have been shown to have good transmit efficiency, which was however not seen when implemented on a silicon substrate such as an ASIC. The implementation of PUTs on ASIC is invaluable in neuromodulation studies, allowing for a millimeter-sized transducer that is capable of focus steering through a phased array. This would allow scientists to target specific neurons or groups of neurons and study their response to ultrasound. As the first step, this thesis aims to improve the transmit efficiency of PUTs on silicon. In addition, an alternative focusing technique is also explored, especially for cases where the implementation of a phased array transducer is not feasible. This thesis will also address the challenge of substrate reflection by exploring ways to reduce ultrasound reflection from an *in vitro* platform.

This thesis approached these challenges by first addressing the optimization of PUTs on silicon. A finite element model (FEM) was implemented to simulate the mechanical and acoustic interaction between various elements within PUTs. After analyzing the contribution of different elements and material combinations, an optimum design was derived. This design was then converted into a fabrication flow which can be implemented in a wafer-level fabrication process that combines standard microfabrication techniques and soft-polymer processing. The fabrication of the devices was conducted in the Else Kooi Laboratory (EKL) cleanroom of TU Delft. The fabricated devices were then assembled and characterized in an underwater acoustic characterization setup. Preliminary biological validation of the transducers was performed in collaboration with researchers from Leiden University Medical Center (LUMC). To tackle the challenge of reducing acoustic reflection, a numerical model was used to simulate the acoustic propagation of waves in a culture well. Combinations of microengineered structures and materials were compared with regard to reduction in acoustic reflection and implementation feasibility.

1.2.1. OUTLINE OF THE THESIS

This dissertation is organized into seven chapters.

Chapter 1 introduced the main motivation for the research, the challenges in the field as well as the outline of the work.

Chapter 2 introduces the theories and concepts in acoustic and ultrasound transducer design used throughout the dissertation.

Chapter 3 explores the first method used to optimize the transmit efficiency of PUTs on silicon by incorporating an air backing layer. The air-backing layer is implemented by creating a cavity underneath the transducer. The optimum thickness of the membrane and its impact on the transmit efficiency of the transducers were studied in FEM and experimental validation.

Chapter 4 explores the implementation of an acoustically-transparent top connection on PUTs. This chapter addressed the research gap in the top connection of PUTs, which to date proved challenging to implement using microfabrication techniques due to the relatively large size of bulk piezoelectric resonators. Using a polymer-metal layer on a microfabricated structure, this chapter proposes a top-level connection that can be implemented on an array of PUTs to maximize their transmit efficiency.

Chapter 5 explores an alternative ultrasound focusing technique to phased array that maximizes transmit efficiency. The chapter presented Fresnel Phasing Zone Plates that can be fabricated using a single photolithography process to allow cheap and rapid prototyping of focusing parameters.

Chapter 6 presents the anti-reflective substrate that can be implemented in microplates and MEAs by using a combination of polymers with structured interface. The proposed concept has been shown to reduce the amplitude of ultrasound echo by 60%.

Chapter 7 concludes the thesis and presents the outlook of the research.

BIBLIOGRAPHY

[1] M. C. Li and M. J. Cook, "Deep brain stimulation for drug-resistant epilepsy", *Epilepsia*, vol. 59, pp. 273–290, 2 Feb. 2018, ISSN: 15281167. DOI: 10.1111/epi.13964.

[2] A. L. Benabid, "Deep brain stimulation for parkinson's disease", *Current Opinion in Neurobiology*, vol. 13, pp. 696–706, 6 2003, ISSN: 09594388. DOI: 10.1016/j.conb.2003.11.001.

[3] H. R. Moes, J. M. ten Kate, A. T. Portman, *et al.*, "Timely referral for device-aided therapy in parkinson's disease. development of a screening tool", *Parkinsonism and Related Disorders*, vol. 109, Apr. 2023, ISSN: 18735126. DOI: 10.1016/j.parkreldis.2023.105359.

[4] V. A. Coenen, B. H. Bewernick, S. Kayser, *et al.*, "Superolateral medial forebrain bundle deep brain stimulation in major depression: A gateway trial", *Neuropsychopharmacology*, vol. 44, pp. 1224–1232, 7 Jun. 2019, ISSN: 1740634X. DOI: 10.1038/s41386-019-0369-9.

[5] W. Klomjai, R. Katz, and A. Lackmy-Vallée, "Basic principles of transcranial magnetic stimulation (tms) and repetitive tms (rtms)", *Annals of Physical and Rehabilitation Medicine*, vol. 58, pp. 208–213, 4 Sep. 2015, ISSN: 18770665. DOI: 10.1016/j.rehab.2015.05.005.

[6] D. Bennabi and E. Haffen, "Transcranial direct current stimulation (tdcs): A promising treatment for major depressive disorder?", *Brain Sciences*, vol. 8, 5 May 2018, ISSN: 20763425. DOI: 10.3390/brainsci8050081.

[7] W. J. Tyler, Y. Tufail, M. Finsterwald, M. L. Tauchmann, E. J. Olson, and C. Majestic, "Remote excitation of neuronal circuits using low-intensity, low-frequency ultrasound", *PLoS ONE*, vol. 3, 10 2008, ISSN: 19326203. DOI: 10.1371/journal.pone.0003511.

[8] J. Blackmore, S. Shrivastava, J. Sallet, C. Butler, and R. Cleveland, "Ultrasound neuromodulation: A review of results, mechanisms and safety", *Ultrasound in Medicine and Biology*, vol. 45, 7 2019, ISSN: 0301-5629. DOI: 10.1016/j.ultrasmedbio.2018.12.015.

[9] S. Luan, I. Williams, K. Nikolic, and T. G. Constandinou, "Neuromodulation: Present and emerging methods", *Frontiers in Neuroengineering*, vol. 7, JUL Jul. 2014, ISSN: 16626443. DOI: 10.3389/fneng.2014.00027.

[10] P. S. Balasubramanian, A. Singh, C. Xu, and A. Lal, "Ghz ultrasonic chip-scale device induces ion channel stimulation in human neural cells", *Scientific Reports*, vol. 10, 1 Dec. 2020, ISSN: 20452322. DOI: 10.1038/s41598-020-58133-0.

[11] M. Duque, C. A. Lee-Kubli, Y. Tufail, *et al.*, "Sonogenetic control of mammalian cells using exogenous transient receptor potential a1 channels", *Nature Communications*, vol. 13, 1 Dec. 2022, ISSN: 20411723. DOI: 10.1038/s41467-022-28205-y.

[12] S. Garcia-Sanz, K. A. Ghotme, D. Hedmont, *et al.*, "Use of transcranial magnetic stimulation for studying the neural basis of numerical cognition: A systematic review", *Journal of Neuroscience Methods*, vol. 369, Mar. 2022, ISSN: 1872678X. DOI: 10.1016/j.jneumeth.2022.109485.

[13] W. Legon, P. Bansal, R. Tyshynsky, L. Ai, and J. K. Mueller, "Transcranial focused ultrasound neuromodulation of the human primary motor cortex", *Scientific Reports*, vol. 8, p. 10 007, 2018. DOI: 10.1038/s41598-018-28320-1. [Online]. Available: www.simnibs.de.

[14] J. K. Mueller and W. J. Tyler, "A quantitative overview of biophysical forces impinging on neural function", *Physical Biology*, vol. 11, 5 2014, ISSN: 14783975. DOI: 10.1088/1478-3975/11/5/051001.

[15] D. Li, Z. Cui, S. Xu, *et al.*, "Low-intensity focused ultrasound stimulation treatment decreases blood pressure in spontaneously hypertensive rats", *IEEE Transactions on Biomedical Engineering*, vol. 67, pp. 3048–3056, 11 Nov. 2020, ISSN: 15582531. DOI: 10.1109/TBME.2020.2975279.

[16] W. Lee, P. Croce, R. W. Margolin, A. Cammalleri, K. Yoon, and S. S. Yoo, "Transcranial focused ultrasound stimulation of motor cortical areas in freely-moving awake rats", *BMC Neuroscience*, vol. 19, 1 Sep. 2018, ISSN: 14712202. DOI: 10.1186/s12868-018-0459-3.

[17] H. Guo, H. Salahshoor, D. Wu, *et al.*, "Effects of focused ultrasound in a "clean" mouse model of ultrasonic neuromodulation", *iScience*, vol. 26, 12 Dec. 2023, ISSN: 25890042. DOI: 10.1016/j.isci.2023.108372.

[18] P. C. Chu, H. Y. Yu, C. C. Lee, R. Fisher, and H. L. Liu, "Pulsed-focused ultrasound provides long-term suppression of epileptiform bursts in the kainic acid-induced epilepsy rat model", *Neurotherapeutics*, vol. 19, pp. 1368–1380, 4 Jul. 2022, ISSN: 18787479. DOI: 10.1007/s13311-022-01250-7.

[19] S. Yoo, D. R. Mittelstein, R. C. Hurt, J. Lacroix, and M. G. Shapiro, "Focused ultrasound excites cortical neurons via mechanosensitive calcium accumulation and ion channel amplification", *Nature Communications*, vol. 13, 1 Dec. 2022, ISSN: 20411723. DOI: 10.1038/s41467-022-28040-1.

[20] K. Lee, J. M. Lee, T. T. Phan, C. J. Lee, J. M. Park, and J. Park, "Ultrasonocoverslip: In-vitro platform for high-throughput assay of cell type-specific neuromodulation with ultra-low-intensity ultrasound stimulation", *Brain Stimulation*, Aug. 2023, ISSN: 1935-861X. DOI: 10.1016/J.BRS.2023.08.002.

[21] M. Saccher, S. Kawasaki, M. P. Onori, G. M. van Woerden, V. Giagka, and R. Dekker, "Focused ultrasound neuromodulation on a multiwell mea", *Bioelectronic Medicine*, vol. 8, 1 Dec. 2022, ISSN: 23328886. DOI: 10.1186/s42234-021-00083-7.

[22] I. M. Suarez-Castellanos, E. Dossi, J. Vion-Bailly, *et al.*, "Spatio-temporal characterization of causal electrophysiological activity stimulated by single pulse focused ultrasound: An ex vivo study on hippocampal brain slices", *Journal of Neural Engineering*, vol. 18, 2 Apr. 2021, ISSN: 17412552. DOI: 10.1088/1741-2552/abdfb1.

[23] S. Stern, A. Rotem, Y. Burnishev, E. Weinreb, and E. Moses, "External excitation of neurons using electric and magnetic fields in one- and two-dimensional cultures", *Journal of Visualized Experiments*, vol. 2017, 123 May 2017, ISSN: 1940087X. DOI: 10.3791/54357.

[24] C. D. Herickhoff and R. van Schaijk, "Cmut technology developments", *Zeitschrift fur Medizinische Physik*, vol. 33, pp. 256–266, 3 Aug. 2023, ISSN: 18764436. DOI: 10.1016/j.zemedi.2023.04.010.

[25] M. Saccher, S. Kawasaki, J. H. Klootwijk, R. Van Schaijk, and R. Dekker, "Modeling and characterization of pre-charged collapse-mode cmuts", *IEEE Open Journal of Ultrasonics, Ferroelectrics, and Frequency Control*, vol. 3, pp. 14–28, Jan. 2023. DOI: 10.1109/ojuffc.2023.3240699.

[26] E. B. Dew, A. K. Ilkhechi, M. Maadi, N. J. Haven, and R. J. Zemp, "Outperforming piezoelectric ultrasonics with high-reliability single-membrane cmut array elements", *Microsystems and Nanoengineering*, vol. 8, 1 Dec. 2022, ISSN: 20557434. DOI: 10.1038/s41378-022-00392-0.

[27] J. Munir, Q. Ain, and H. J. Lee, "Reliability issue related to dielectric charging in capacitive micromachined ultrasonic transducers: A review", *Microelectronics Reliability*, vol. 92, pp. 155–167, Jan. 2019, ISSN: 00262714. DOI: 10.1016/j.microrel.2018.12.005.

[28] K. Roy, J. E. Y. Lee, and C. Lee, "Thin-film pmuts: A review of over 40 years of research", *Microsystems and Nanoengineering*, vol. 9, 1 Dec. 2023, ISSN: 20557434. DOI: 10.1038/s41378-023-00555-7.

[29] P. Tipsawat, S. J. Ilham, J. I. Yang, Z. Kashani, M. Kiani, and S. Trolier-Mckinstry, "32 element piezoelectric micromachined ultrasound transducer (pmut) phased array for neuromodulation", *IEEE Open Journal of Ultrasonics, Ferroelectrics, and Frequency Control*, vol. 2, pp. 184–193, Aug. 2022. DOI: 10.1109/ojuffc.2022.3196823.

[30] G. D. Shilpa, K. Sreelakshmi, and M. G. Ananthaprasad, "Pzt thin film deposition techniques, properties and its application in ultrasonic mems sensors: A review", in *IOP Conference Series: Materials Science and Engineering*, vol. 149, Institute of Physics Publishing, Oct. 2016. DOI: 10.1088/1757-899X/149/1/012190.

[31] B. E. Eovino, Y. Liang, and L. Lin, "Concentric pmut arrays for focused ultrasound and high intensity applications", in *2019 IEEE 32nd International Conference on MIcro Electro Mechanical Systems (MEMS)*, IEEE, 2019, pp. 771–774, ISBN: 9781728116105.

[32] R. M. Pinto, V. Gund, C. Calaza, K. K. Nagaraja, and K. B. Vinayakumar, "Piezoelectric aluminum nitride thin-films: A review of wet and dry etching techniques", *Microelectronic Engineering*, vol. 257, Mar. 2022, ISSN: 01679317. DOI: 10.1016/j.mee.2022.111753.

[33] T. Costa, C. Shi, K. Tien, J. Elloian, F. A. Cardoso, and K. L. Shepard, "An integrated 2d ultrasound phased array transmitter in cmos with pixel pitch-matched beamforming; an integrated 2d ultrasound phased array transmitter in cmos with pixel pitch-matched beamforming", *IEEE Transactions on Biomedical Circuits and Systems*, vol. 15, 4 2021. DOI: 10.1109/TBCAS.2021.3096722. [Online]. Available: https://www.ieee.org/publications/rights/index.html.

[34] C. Chen, Z. Chen, D. Bera, *et al.*, "A front-end asic with receive sub-array beamforming integrated with a 32 × 32 pzt matrix transducer for 3-d transesophageal echocardiography", *IEEE JOURNAL OF SOLID-STATE CIRCUITS*, vol. 52, 4 2017. DOI: 10.1109/JSSC.2016.2638433. [Online]. Available: http://ieeexplore.ieee.org..

[35] Philips Healthcare, *Intravascular ultrasound (ivus)*, Accessed: 2024-08-16, 2024. [Online]. Available: https://www.usa.philips.com/healthcare/education-resources/technologies/igt/intravascular-ultrasound-ivus.

[36] Oldelft Ultrasound, *4d ice transducer*, Accessed: 2024-08-16, 2024. [Online]. Available: https://www.oldelft.com/products/4d/4d-ice-transducer/.

[37] D. M. Van Willigen, E. Kang, J. Janjic, *et al.*, "A transceiver asic for a single-cable 64-element intra-vascular ultrasound probe", *IEEE Journal of Solid-State Circuits*, vol. 56, pp. 3157–3166, 10 Oct. 2021, ISSN: 1558173X. DOI: 10.1109/JSSC.2021.3083217.

[38] Y. M. Hopf, B. W. Ossenkoppele, M. Soozande, *et al.*, "A pitch-matched transceiver asic with shared hybrid beamforming adc for high-frame-rate 3-d intracardiac echocardiography", *IEEE Journal of Solid-State Circuits*, vol. 57, pp. 3228–3242, 11 Nov. 2022, ISSN: 1558173X. DOI: 10.1109/JSSC.2022.3201758.

[39] V. Pashaei, P. Dehghanzadeh, G. Enwia, M. Bayat, S. J. Majerus, and S. Mandal, "Flexible body-conformal ultrasound patches for image-guided neuromodulation", *IEEE transactions on biomedical circuits and systems*, vol. 14, pp. 305–318, 2 Apr. 2020, ISSN: 1940-9990. DOI: 10.1109/TBCAS.2019.2959439. [Online]. Available: https://pubmed.ncbi.nlm.nih.gov/31831437/.

[40] C. Van Damme, G. K. Wardhana, A. I. Velea, V. Giagka, and T. L. Costa, "Feasibility study for a high-frequency flexible ultrasonic cuff for high-precision vagus nerve ultrasound neuromodulation", *IEEE Transactions on Ultrasonics, Ferroelectrics, and Frequency Control*, vol. 71, pp. 745–756, 7 2024, ISSN: 15258955. DOI: 10.1109/TUFFC.2024.3381923.

2

Introduction to Ultrasound Transducers

This chapter provides an introduction to piezoelectric transducers and acoustic theory, establishing the foundation for understanding the research presented in the thesis. The chapter begins with a detailed exploration of the piezoelectric effect, explaining how certain materials convert electrical energy into mechanical energy and vice versa. Key parameters governing transducer performance, such as the electromechanical coupling coefficient, Curie temperature, and mechanical quality factor, are also discussed. The chapter then examines important design considerations for piezoelectric transducers, including the relationship between transducer geometry, operating frequency, and focal distance. Additionally, the chapter explores relevant acoustic principles, such as wave propagation, acoustic impedance, reflection, transmission, and attenuation.

2

This chapter establishes a foundation in piezoelectric transducer technology and acoustic theory, providing the necessary background to understand the research presented in this thesis. It begins with exploring the piezoelectric effect, detailing how certain materials convert electrical energy into mechanical energy and vice versa. Key parameters that govern transducer performance, such as the electromechanical coupling coefficient, Curie temperature, and mechanical quality factor, are introduced and discussed. The chapter then examines important design considerations for piezoelectric transducers, including how transducer geometry and operating frequency determine the focal distance. Additionally, the chapter explores the acoustic principles relevant to transducer operation, such as wave propagation, acoustic impedance, reflection, transmission, and attenuation. This comprehensive overview provides the necessary context for understanding the subsequent chapters.

2.1. PIEZOELECTRICITY

2.1.1. PIEZOELECTRIC EFFECT

Piezoelectricity describes the reversible process of converting between electrical and mechanical energy in certain materials. This phenomenon stems from the lack of a center of symmetry in the crystal structure of piezoelectric materials, resulting in an uneven distribution of charges [1]. When an electric field is applied, these charges are displaced, causing the crystal lattice to deform and produce mechanical strain. Conversely, applying mechanical stress to the material induces an electrical charge. This bidirectional conversion between electrical signals and mechanical vibrations, known as the piezoelectric effect and inverse piezoelectric effect, respectively, is the foundation for many applications, including ultrasound transducers, actuators, and sensors [2].

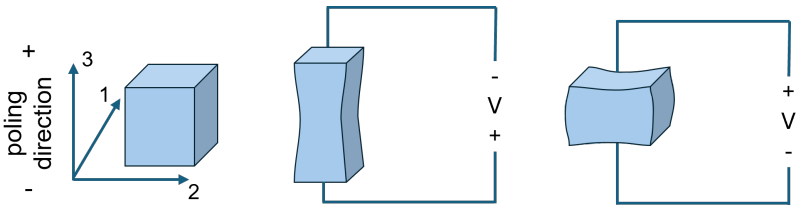

Figure 2.1: A schematic describing the piezoelectric effect: (left) piezoelectric element in the absence of electric field, (middle) piezoelectric element expands when an electric field is applied opposite of the poling direction, and (right) piezoelectric element contracts when an electric field is applied along the poling direction.

The efficiency of this electromechanical conversion is characterized by the electromechanical coupling coefficient (k), which quantifies the fraction of electrical energy converted to mechanical energy. k is defined as the ratio of the stored energy dissipated in the load (w_s) to the total energy (w_t) as seen in the following formula [3]:

$$k^2 = \frac{w_s}{w_t} \tag{2.1}$$

Therefore, k^2 represents the efficiency of electromechanical energy conversion for a material [1]. Due to the anisotropy of piezoelectric materials, the characteristics of

Table 2.1: Typical parameters of piezoelectric materials [1],[5].

Properties	PZT-4	PZT-5H	PMN-PT	NBT
k_t	0.47	0.52	0.57	0.47
k_{33}	0.69	0.75	0.90	0.55
T_c	350°C	200°C	90°C	85°C

a piezoelectric material are assigned with number 1,2 and 3 corresponding to the X, Y and Z axes of the Cartersian coordinate system (Figure 2.1). The direction of polarization established during the poling process is typically denoted as axis 3. When assessing the efficiency of a piezoelectric material, multiple coupling coefficients are denoted by k_{ij}, where i indicates the axis of electrical load connection and j represents the direction of stress/strain. This means that the piezoelectric properties of the material vary depending on the direction of the applied force or electric field. A widely-used coupling coefficient is k_{33}, which represents the coupling when the electrical load and the resulting stress/strain are along the axis 3. Another widely-used coupling coefficient is k_t, the thickness-mode coupling coefficient. k_t is a variant of k_{33} under the condition of zero lateral strain. k_t is used when the lateral dimension is larger than the longitudinal dimension, whereas k_{33} is applicable to transducers shaped as a tall, narrow bar [1]. Additionally, piezoelectric materials are sensitive to temperature, exhibiting degradation of their piezoelectric properties above a critical point called the Curie temperature (T_c) [4]. Therefore, the Curie temperature is a crucial consideration during both the fabrication and operation of piezoelectric transducers. Exceeding this temperature during fabrication can permanently damage the material's piezoelectric properties while operating temperatures near the Curie point can lead to performance degradation and potential device failure.

2.1.2. PIEZOELECTRIC MATERIALS

The choice of piezoelectric material depends on the specific application and desired properties. Lead zirconate titanate (PZT) is a widely-used piezoelectric material for ultrasound transducers due to its k. PZT is classified into soft and hard types. Soft PZT, such as PZT-5H, has a much higher piezoelectric coupling coefficient than hard PZT, making it suitable for applications requiring high efficiency or sensitivity [1]. Hard PZT, such as PZT-4, has a lower piezoelectric coupling coefficient but a higher Curie temperature, making it suitable for high-power and high-temperature applications [5]. Lead magnesium niobate doped with lead titanate (PMN-PT) offers an even higher coupling factor than PZT [1]. However, it presents fabrication challenges due to its brittleness and very low Curie temperature. Lead-free piezoelectric materials, such as sodium bismuth titanite (NBT) [5],[4], have garnered attention due to the health and environmental concerns associated with lead. Although their piezoelectric performance currently lags behind PZT, significant research efforts aim to improve their properties.

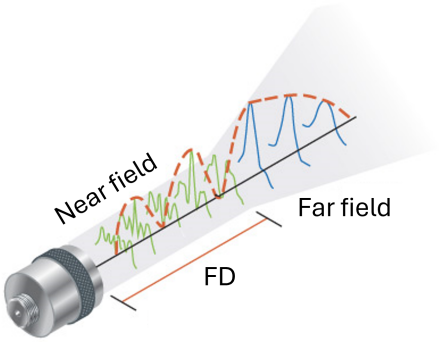

Figure 2.2: Schematic illustrating the near field and far field of an ultrasound transducer. The near field is characterized by complex pressure variations, while the far field exhibits a single main lobe and a more uniform decay of ultrasound intensity. The natural focal distance marks the transition between these zones, adapted from [6] .

2.2. TRANSDUCER DESIGN

2.2.1. FOCAL DISTANCE OF A TRANSDUCER

In an unfocused ultrasound transducer, the vibrations on the transducer generate pressure waves that propagate into the surrounding medium. The region directly in front of the transducer is known as the near field or Fresnel zone (Figure 2.2). In this region, the ultrasound beam exhibits complex interference patterns, with pressure variations and side lobes [1]. Beyond the near field lies the far field or Fraunhofer zone. In this region, the ultrasound beam diverges and the pressure field decays more uniformly with distance (Figure 2.2). The far field is characterized by a main lobe and progressively weaker side lobes [1]. At the transition between the near field and far field, lies the natural focal point of the transducer. The distance of the natural focal point from the transducer (F_D) depends on the diameter of the transducer (D), the speed of sound in the medium (c), and the frequency of the ultrasound (f), and, for circular transducer apertures, can be given by:

$$F_D = \frac{D^2}{4\lambda} = \frac{fD^2}{4c} \tag{2.2}$$

2.2.2. COMPONENTS OF PIEZOELECTRIC ULTRASOUND TRANSDUCER

The simplest form of piezoelectric transducer is a single-element ultrasound transducer, which uses a single piezoelectric element. Typically, the transducer consists of several components: the piezoelectric element, a matching layer, and a backing layer (Figure 2.3). The matching layer improves the acoustic coupling to the propagation medium by minimizing loss due to reflection [7]. The backing layer affects the mechanical quality factor of the transducer and, consequently, the bandwidth and transmit efficiency of the transducer [7]. In this particular case, wires are connected on the bottom and top (through a brass pipe) of the PZT to supply the driving signal.

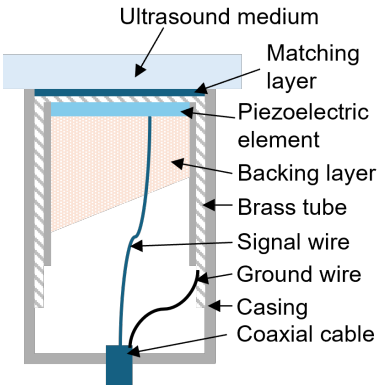

Figure 2.3: A cross-section of a typical single element transducer with matching layer and backing layer [8].

2.2.3. REFLECTION AND TRANSMISSION

When an acoustic wave encounters an interface between two different media, it undergoes both reflection and transmission [7]. The extent to which these phenomena occur depends on the acoustic impedance mismatch between the two media. Acoustic impedance (Z) is a property of a medium that characterizes the resistance to sound wave propagation and is defined as the product of the medium's density (ρ) and the speed of sound (c). In an interface of media with identical acoustic impedances, the wave passes through the interface without any reflection. However, if there is an impedance mismatch, part of the wave is reflected back into the first medium, and the remaining part is transmitted into the second medium. The reflection coefficient (R) quantifies the ratio of the reflected wave pressure amplitude to the incident wave pressure amplitude [7], which can be determined by the acoustic impedance of the two media (Z1 and Z2):

$$R = \frac{Z_2 - Z_1}{Z_2 + Z_1} \tag{2.3}$$

The transmission coefficient (T) quantifies the ratio of the transmitted wave amplitude to the incident wave amplitude and it is related to the reflection coefficient by the conservation of energy and thus can be calculated as:

$$T = 1 - R \tag{2.4}$$

2.2.4. MECHANICAL QUALITY FACTOR

The mechanical quality factor (Q) is a dimensionless parameter that describes how efficiently the transducer vibrates [1]. The vibration of a transducer with high Q will decay slower than a transducer with low Q (Figure 2.4(a)). Consequently, the mechanical energy stored in the resonator will dissipate more slowly for higher Q. The Q can be determined by observing the frequency response of the transducer (Figure 2.4(b)) [1], and it is defined as the ratio between the resonance frequency (fr) and the full-width half maximum bandwidth (Δf) [7]:

$$Q = \frac{f_r}{\Delta f} \tag{2.5}$$

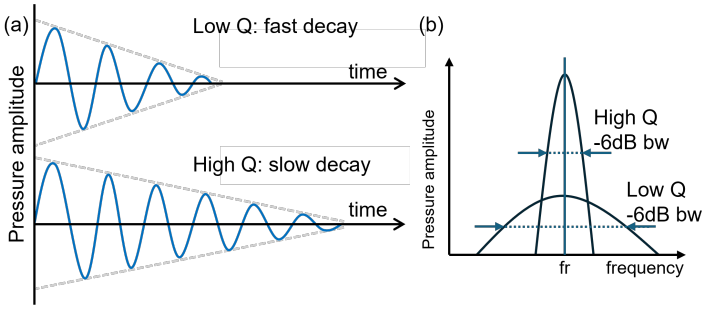

Figure 2.4: The effect of high and low Q:(a) it can be seen in the time domain that Q affects the vibration decay of a transducer, (b) consequently, Q affects the bandwidth and maximum amplitude in the frequency domain.

The quality factor of a transducer is influenced by the material properties and the construction of the transducer. Layers surrounding the piezoelectric element, such as the backing layer and the matching layer, can directly influence the vibration of the piezoelectric material due to transmission loss and damping of reverberation [7]. The choice of Q depends on the specific application; in ultrasound imaging, a short pulse length is desired to achieve high axial resolution, and therefore, transducers with low Q are preferred [7]. In contrast, applications that require high output pressure or high power efficiency prefer a transducer with high Q, causing less damping to minimize losses [5],[9].

2.2.5. ACOUSTIC ATTENUATION

As waves travel through a medium, they will experience loss due to absorption and scattering [10]. Absorption occurs when the mechanical energy is converted into heat by the friction of molecules, therefore reducing the amplitude of acoustic waves. Scattering describes the deviation of wave propagation due to inhomogeneity within the medium [10]. The scattered waves can interfere with each other and the original wave, which reduces the overall wave amplitude. The attenuation of a given material is often quantified by its attenuation coefficient α, which describes the loss in intensity over a unit distance, and it is typically expressed in dB/cm. The attenuation coefficient is frequency dependent, sometimes expressed in dB/cm/MHz [11]. The relationship between frequency and attenuation coefficient is nonlinear and instead follows a power law relationship [10].

$$\alpha = \alpha_0 \cdot f^n \tag{2.6}$$

, where α_0 is a material-specific frequency-dependent attenuation coefficient, f is the frequency of ultrasound waves, and n is the power exponent typically close to 1.

BIBLIOGRAPHY

[1] K. Nakamura, *Ultrasonic Transducers: Materials and Design for Sensors, Actuators and Medical Applications* (Woodhead Publishing Series in Electronic and Optical Materials). Woodhead Publishing, 2012, ISBN: 978-1845699895.

[2] M. C. Sekhar, E. Veena, N. S. Kumar, K. C. B. Naidu, A. Mallikarjuna, and D. B. Basha, "A review on piezoelectric materials and their applications", *Crystal Research and Technology*, vol. 58, 2 Feb. 2023, ISSN: 15214079. DOI: 10.1002/crat.202200130.

[3] R. S. C. Cobbold, *Foundations of Biomedical Ultrasound*. NY, USA: Oxford University Press, 2007, ISBN: 0195168313.

[4] S. Zhang, C. A. Randall, and T. R. Shrout, "Recent developments in high curie temperature perovskite single crystals", *564 ieee transactions on ultrasonics, ferroelectrics, and frequency control*, vol. 52, 4 2005.

[5] T. Zawada, T. Bove, K. Astafiev, E. Ringgaard, and R. Lou-Moeller, "Lead-free hifu transducers", *Ultrasound in Medicine and Biology*, vol. 48, pp. 2530–2543, 12 Dec. 2022, ISSN: 1879291X. DOI: 10.1016/j.ultrasmedbio.2022.08.010.

[6] Olympus, *Beam characteristics*, https://www.olympus-ims.com/id/ndt-tutorials/transducers/characteristics/, Accessed on April 14, 2024, 2024.

[7] T. L. Szabo, *Diagnostic Ultrasound Imaging: Inside Out*. Elsevier, 2014.

[8] E. P. Papadakis *et al.*, "Measurement of the nonlinearity parameter b/a of liquids", *The Journal of the Acoustical Society of America*, vol. 106, no. 3, pp. 1228–1239, 1999.

[9] H. S. Gougheri, A. Dangi, S. R. Kothapalli, and M. Kiani, "A comprehensive study of ultrasound transducer characteristics in microscopic ultrasound neuromodulation", *IEEE Transactions on Biomedical Circuits and Systems*, vol. 13, pp. 835–847, 5 Oct. 2019, ISSN: 19409990. DOI: 10.1109/TBCAS.2019.2922027.

[10] K. Ono, "A comprehensive report on ultrasonic attenuation of engineering materials, including metals, ceramics, polymers, fiber-reinforced composites, wood, and rocks", *Applied Sciences (Switzerland)*, vol. 10, 7 Apr. 2020, ISSN: 20763417. DOI: 10.3390/app10072230.

[11] H. Shankar and P. S. Pagel, "Potential adverse ultrasound-related biological effects: A critical review", *Anesthesiology*, vol. 115, pp. 1109–1124, 5 2011, ISSN: 15281175. DOI: 10.1097/ALN.0b013e31822fd1f1.

3

Integrated Air Backing Layer on Silicon Substrate

This chapter presents a novel approach to improve the transmit efficiency of piezoelectric ultrasound transducers (PUTs) by incorporating an air-backing layer within the silicon substrate. This integrated air-backing is achieved through microfabrication techniques, selectively thinning the silicon substrate beneath the transducers to create a suspended membrane. The membrane design was optimized at a thickness of 20 µm and demonstrated a significant improvement in output intensity by a factor of 5.11 compared to transducers on a standard 300 µm silicon substrate when measured at 8.5 MHz. Even when accounting for shifts in resonance frequency, the air-backed transducers showed a notable enhancement (average factor of 2.65) at their respective resonance frequencies. The integrated air-backing layer shows promise for enhancing the efficiency of PUTs-on-ASIC for ultrasound neuromodulation.

Parts of this chapter have been published in [1].

Piezoelectric ultrasound transducers (PUTs) have been the industry standard for decades in the ultrasound world [2]. Compared to micromachined ultrasound transducers, PUTs have typically higher transmit efficiency [2]. Although piezoelectric ultrasound transducers (PUTs) have reached commercial maturation, especially in handheld imaging devices (Figure 3.1(a)), several works have shown the integration of PUTs on ASIC to reduce the overall size of the transducer's driving electronics while enabling complex features such as phased array focusing (Figure 3.1(b)). ASIC technology alleviates the challenges of routing a large number of interconnects needed to implement a phased array, allowing scaling up the number of elements in the array while minimizing the total area of the system due to the low cable count (Figure 3.1(b)). In imaging, several implementations of PUTs on ASIC have been demonstrated such as for intravascular imaging [3] and intracardiac echocardiography [4]. In the context of neuromodulation, PUTs on ASIC offer a steerable stimulation in a small form factor, allowing for wearable or implantable stimulators for ultrasound neuromodulation [5].

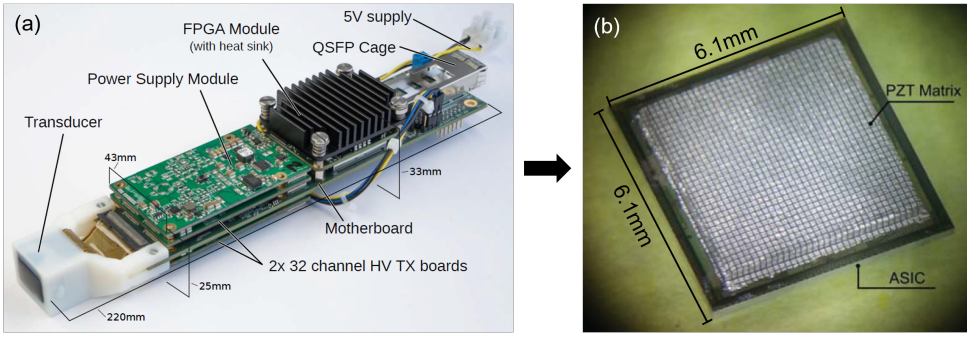

Figure 3.1: Comparison in dimensions between (a) PCB-based [6] and (b) ASIC-based phased array PUTs [7].

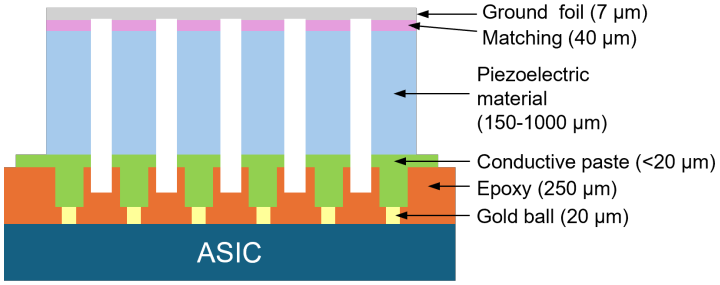

Figure 3.2: Cross section of PUTs-on-ASIC stack used in [3],[4].

Despite the developments of CMOS integrated PUTs, their performance still suffers from low output efficiency. Chen et al. reported a transmit efficiency of 6 kPa/V with a maximum pressure of 300 kPa [7]. Costa et al. reported a transmit efficiency of 20 kPa/V

with a maximum pressure of 100 kPa [5]. The transmit efficiency of the piezoelectric transducer on CMOS IC is still not optimum when compared to a more conventional approach of piezoelectric focused ultrasound transducer that can reach up to 80 kPa/V [8]. In theory, the pressure generated by a piezoelectric transducer scales linearly to the input voltage. In tissue ablation, the input voltage can go as high as 200 V to generate tens of MPa [9], [10]. However, technology constraints and transistor sizing limit the voltage supply capabilities of ASICs to the tens of V. More importantly, power dissipation in ASICs can lead to excessive heat. With a power density of 100 mW/cm^2 corresponding to 1 degree Celsius of temperature increase. if tens a power supply of tens of volts are needed, temperature can rise by several tens of degrees, which is a major concern for both wearable and implantable ultrasound neuromodulation devices, as well as for *in vitro* studies. Consequently, maximizing the transmit efficiency of the transducer becomes crucial to achieve the desired range of output pressures within the limitation of voltage supply and thermal dissipation. Therefore, optimization of the current implementation techniques is necessary to achieve the pressure required for ultrasound neuromodulation.

3.1. SIMULATION OF PUTS ON SILICON

3.1.1. PRELIMINARY SIMULATION SETUP

A finite element modeling (FEM) in COMSOL Multiphysics was performed to study the influence of different elements of ASIC/silicon-integrated ultrasound transducers. The simulation was performed using an axisymmetric model that utilize three physics modules: electrostatics, solid mechanics, and pressure acoustics. The electrostatic and solid mechanic module simulated the piezoelectric effect which became the acoustic source in the model. The simulation was performed in the frequency domain, which observed the harmonic steady state of the model. The simulation model consists of three primary geometries: the piezoelectric material, the propagation medium, and the backing substrate as seen in Figure 3.3. Water was chosen as the medium to mimic the acoustic properties of soft tissue, which will be used during the measurement stage. A lead zirconate titanate (PZT) type 5H with a thickness of 0.21 mm was used as the transducer, which corresponded to a resonance frequency of 10 MHz. An electrical potential was applied across the transducer along its poling axis. Due to the axisymmetric model, the rectangular definition of the transducer formed a cylinder in the 3D space. A perfectly matched layer (PML) was added to the outer boundaries of the model to prevent reflection due to the finite simulation space. The use of PML on the boundaries of the simulation space implies an infinitely large medium and backing layer.

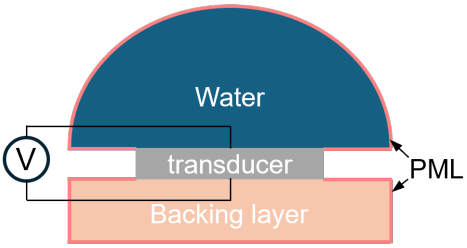

Figure 3.3: Diagram explaining the schematic of the FEM in COMSOL.

3.1.2. PRELIMINARY SIMULATION RESULTS

Three configurations of the backing layer consisting of water, silicon, and air, were assessed to see the implications of the backing layer on the acoustic pressure generated by the transducer. The material properties used during the simulation were provided by the COMSOL material database, with the exception of a few taken from the literature. The acoustic properties of the materials can be seen in Table 3.1

Table 3.1: A list of acoustic properties of materials used in the COMSOL FEM

Material	Speed of sound (m/s)	Density (kg/m^3)	Acoustic impedance $(MRayl)$
Water	1480	1000	1.48
PZT-5H	4600	7600	34.96
Silicon	8440	2330	19.67
Glass	5968	2200	13.13
Air [11]	343	1.293	0.00044
Epoxy [12]	2650	1150	3.05

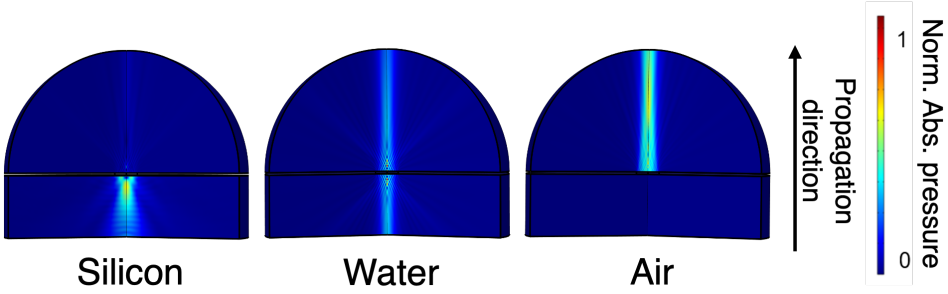

Figure 3.4: The effect of different backing layers on the normalized intensity of a piezoelectric ultrasound transducer.

The water backing layer was simulated as the baseline of the simulation. The deformation of a piezoelectric material under a symmetrical AC signal along the driving axis

is distributed equally in both directions. Therefore, the pressure profile generated on the top and the bottom of the transducer were identical, as shown in Figure 3.4(middle) The water-backed simulation also showed the beam profile of the transducer in the medium without the influence of reflection that might occur from the back of the transducer.

The silicon backing layer represents the integrated piezoelectric transducer on an ASIC. The use of silicon substrate significantly reduced the generated pressure that went toward the water medium. The reduction in overall pressure can be explained by the damping that is introduced by the substrate. It is also important to note that the reflection between the water-PZT interface is higher than the PZT-silicon interface due to the lack of a matching layer. The lower reflection on the PZT-silicon caused a significant pressure to be seen in the substrate. The reflection can be quantified by using Eq. 2.3, which indicates that higher reflection occurs in the interface of two materials with larger acoustic impedance mismatch. When compared to the water backing layer, the pressure generated by the transducer was reduced significantly with the presence of silicon substrate, which could explain the low transmit efficiency seen in the literature. The air backing layer was explored since it was widely used as a backing layer in handheld high-intensity ultrasound transducers[13]. This configuration resulted in the highest peak pressure among the three configurations. The highly mismatched acoustic impedance between air and PZT resulted in the absence of pressure going towards the backing layer, therefore reducing the probability of waves being reflected from the back of the transducer and interfering with the waves on the front side of the transducer. This model showed the efficacy of the air-backed transducers and, more importantly, the detrimental effect of having silicon substrate on the performance of piezoelectric transducers. However, the practical implementation of applying a more optimized backing on silicon is not straightforward. In a phased array transducer driven by ASIC, the piezoelectric transducers need to be driven by electric signals provided by the IC. Therefore, there has to be a direct interface between the piezoelectric transducers and the silicon substrate. In the next section, a new method to circumvent this limitation is proposed.

3.2. PROPOSED CONCEPT: INTEGRATED AIR BACKING THROUGH SUBSTRATE THINNING

One idea presented in this study is to thin down the silicon substrate selectively in order to create a more optimal backing layer by having an air-filled cavity underneath the transducers. Although a typical ASIC that utilizes complementary metal-oxide-semiconductor (CMOS) has a thickness of approximately 300 μm, the bulk of the thickness is present to provide mechanical support to the IC. The layer that includes the active devices (transistors and diodes) of an IC is contained within a few micrometers below the surface of the silicon, and underneath the thin metal stack. Several works have shown that thinning a CMOS IC below 20 µm can be done without affecting the performance of the IC [14],[15]. There are, however, other important factors when deciding how aggressive the ASICs can be thinned in the context of piezoelectric transducer integration, such as the mechanical stability of the IC, which might lead to damage during its handling. The integration process of piezoelectric elements on the ASIC also involves steps such as wafer dicing of the piezoelectric elements that require mechanical stabil-

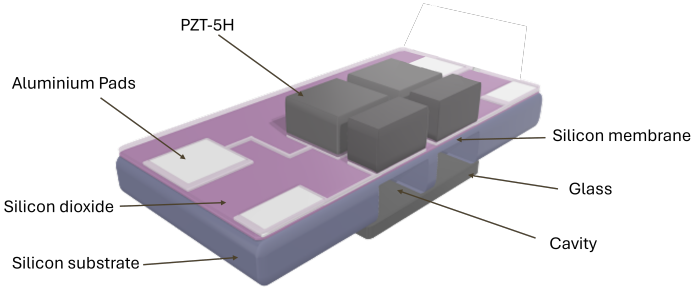

Figure 3.5: Schematic showing the selective thinning concept to create air backing layer in silicon.

ity. Since the backing layer is only needed below the transducers, a selective thinning of the silicon substrate provides a good balance between the mechanical stability of the IC and maximizing the transmit efficiency of the transducers. Despite prior work having demonstrated CMOS IC thinning [14],[15], and even though air-backing is common in handheld therapeutic ultrasound transducers, a study demonstrating the effects of progressively thinner silicon substrates on integrated piezoelectric transducers and its generated acoustic intensity was not yet performed. To investigate this, the concept of selective thinning of the silicon substrate can be seen in Figure 3.5. Cavities are selectively placed underneath every element. Piezoelectric elements were placed on top of the membranes that formed as a result of the cavities. Characterization of an ultrasound transducer would be done by submerging the transducer in water, which is used as the model of soft tissue. A layer of glass was added to the back of the silicon substrate to prevent water from entering the cavities during the characterization, thus forming an air-backing layer.

3.2.1. SIMULATION OF THE INTEGRATED AIR BACKING LAYER

During the preliminary simulations, an improvement over the generated pressure was seen when the transducer was placed directly on top of the air backing layer. The proposed concept tried to mimic this by having cavities below the piezoelectric elements. However, a silicon membrane is present between the piezoelectric elements and the air-backing layer, which can affect its efficacy. Further simulations with a model that better resembles the proposed concept were performed. The primary goal of the simulations was to identify the relationship between the thickness of silicon membranes and the transducers' transmit efficiency. As shown in the preliminary simulation, the presence of silicon reduces the transmit efficiency of the transducers. However, a thinner substrate could lead to lower fabrication yield and long-term reliability due to membrane rupture.

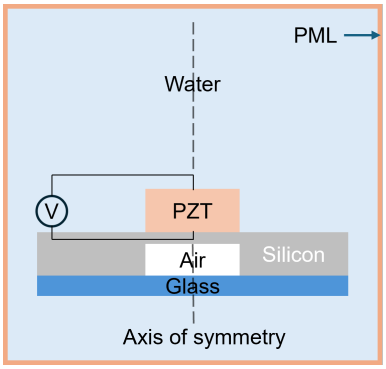

Figure 3.6: Schematic of the FEM setup in COMSOL using an axisymmetric model.

3.2.2. SIMULATION SETUP

Similar to the previous simulation, an axisymmetric simulation in the frequency domain was used. The same physics modules, solid mechanics, electrostatics, and pressure acoustics were used. A layer of PML was also applied on the boundary of the simulation space. The model included more complex geometries to represent a more realistic condition. The thickness of the substrate is no longer infinite; the silicon is assumed to be 300 μm-thick with a layer of silica glass underneath the substrate. The silicon thickness was chosen to mimic the typical thickness of ASICs. The water medium surrounding the transducer stack was applied to better represent the typical condition of ultrasound transducer characterization. A PZT-5H with a thickness of 0.27 mm was used which corresponds to a resonance frequency of 8.5 MHz, based on the study presented in [5]. The material properties used during the simulation can be seen in Table 3.1. The focal distance of the transducer is expected to be at around 12 mm distance, based on the formula Eq. 2.2. Additional information regarding the simulation setup, such as the thicknesses of all materials and the mesh properties can be seen in Table 3.2.

Table 3.2: Summary of the simulation parameters used in COMSOL

Parameters	value
PZT thickness	0.27 mm
PZT radius	1.5 mm
Silicon substrate thickness	0.3 mm
Silica glass thickness	0.3 mm
Driving frequency	8.5 MHz
Medium radius	5 mm
Mesh shape	Quadrilateral
Maximum mesh size	17.4 $\mu m(\lambda_{medium}/10)$

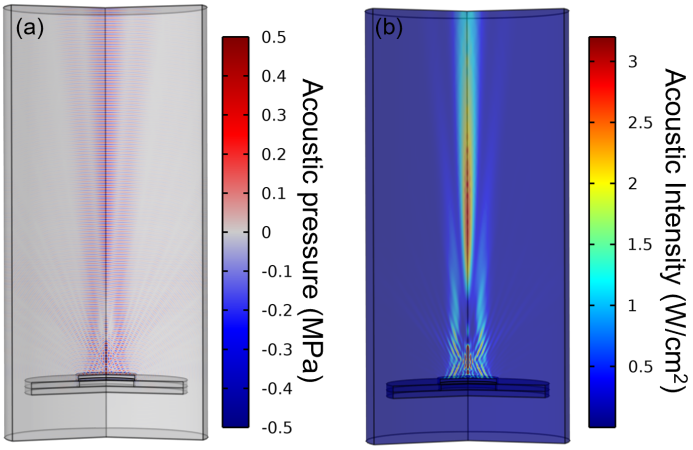

Figure 3.7: The FEM result of the integrated air-backing layer with a membrane thickness of 20 μm: (a) acoustic pressure field and (b) acoustic intensity field.

3.2.3. SIMULATION RESULTS

The pressure distribution generated by the transducer can be seen in Figure 3.7(a), which shows the maximum and minimum pressure within the simulation field. The corresponding intensity profile can be seen in Figure 3.7(b) where the spatial characteristics of the transducer can be observed. The intensity is defined as:

$$I_{rms} = \frac{P_{peak}^2}{2Z} \tag{3.1}$$

, where P_{peak} is peak pressure and Z is the acoustic impedance of the medium. The intensity signifies the acoustic energy in the unit area, and it is widely used in biomedical ultrasound to assess the safety and dosage of treatments [16].

The transducer generates a conical volumetric focal beam profile which can be seen in the intensity field. It is important to note that in the near field, peaks of intensity will occur due to interference of waves coming from different points of the transducer. Due to the significant variations in intensity in the near field, a comparison of the intensity of the transducers has to be done beyond the near field as indicated in Figure 3.8(a) and Figure 3.8(b). A 1D plot of the intensity was taken from the center point of the transducer, perpendicular to the surface (Figure 3.8(c) and Figure 3.8(d)). The plot shows the distance and intensity of the focal spot which was used to characterize the performance of the transducers. Due to the unfocused nature of the transducer, the focal spot covers a large volume. The transducer also generated a focal distance similar to the estimation as seen in the 1D plot. By observing the I_{rms} within the focal area between 5 to 15 mm distance from the transducer, a drastic improvement in the transducer with air backing can be seen.

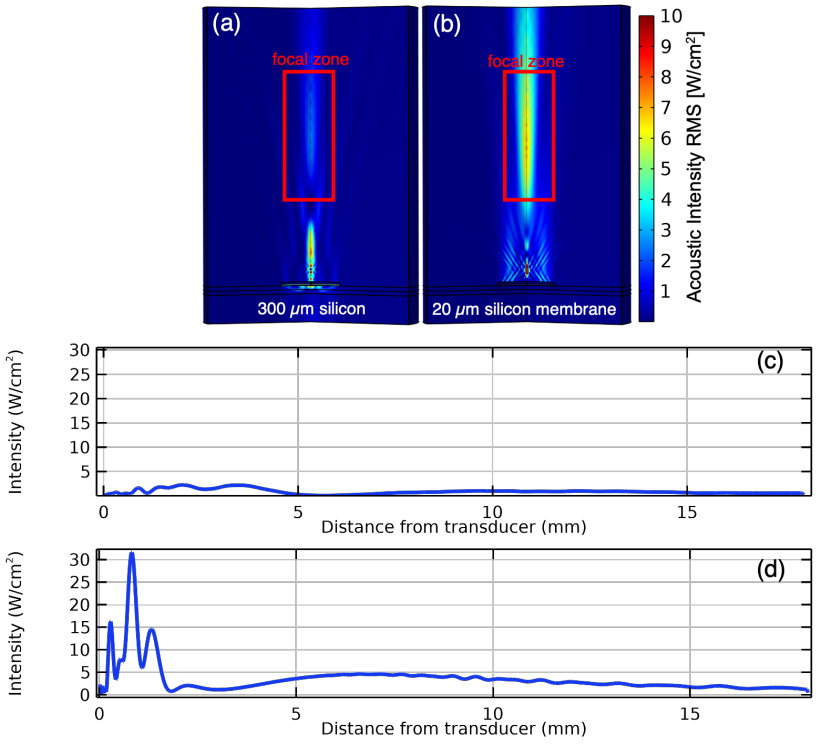

Figure 3.8: The FEM results in COMSOL showing the intensity profile of a transducer with (a) 300 μm silicon substrate, therefore no air backing layer. (b) 20 μm silicon membrane with air backing layer underneath. 1D plots of the intensity taken along the propagation direction from the center of the transducer with (C) no air backing layer and (d) with 20 μm silicon membrane and air backing layer.

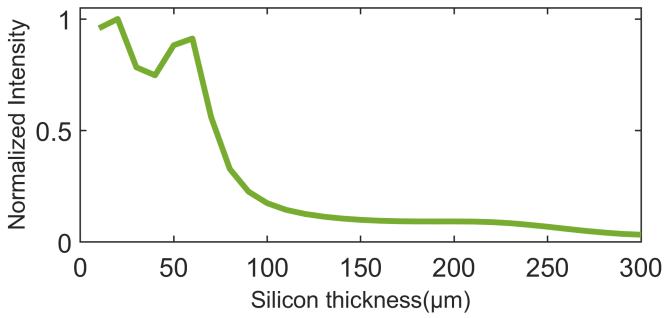

Figure 3.9: A 1D plot showing the measured I_{rms} of the transducer as a function of silicon thickness.

To uncover the full effect of different silicon thicknesses on I_{rms}, simulations were repeated with silicon thickness between 10 to 300 μm with a step of 5 μm, while other parameters were kept constant. During each iteration, the highest intensity within the focal area was collected and composed into a plot seen in Figure 3.9. No significant improvement was observed at membrane thickness above 100 μm, which corresponds to approximately 0.1λ of wavelength in the silicon. An inverse relation between intensity and membrane thickness can be seen at membrane thickness lower than 100 μm. There is a slope of -1.8/μm between 60 μm to 100 μm. Oscillation of performance can be seen at membranes thinner than 60 μm with positive peaks formed at 20 μm and 60 μm thickness. Negative peaks were formed at 10 μm and 40 μm. These positive and negative peaks can occur due to the interference with waves reflected from the membrane-air interface on the back of the transducer. The distance traveled by this reflection scale with the factor of two of the membrane thickness, which caused the oscillation to be more pronounced at thinner membranes. Regardless of the oscillation, the intensity still maintained an inverse relation with the membrane thickness. In agreement with the preliminary simulation, the intensity generated by the transducer was inversely related to the thickness of the membrane. The optimum intensity was obtained with a membrane thickness of 20 μm. A factor of 19.7 improvement was seen when comparing the transducer with a silicon substrate with a thickness of 300 μm and 20 μm.

3.3. EXPERIMENTAL VALIDATION

3.3.1. MICROFABRICATION TECHNIQUES

Test devices mimicking CMOS ICs were fabricated at a wafer scale using silicon-based micromachining or microfabrication Figure 3.9. The test device featured aluminum contact pads connected by interconnects which were used to drive piezoelectric transducers. Apart from the contact pads, aluminum layers were passivated using silicon dioxide to prevent unwanted conduction and leakage in the circuit. Several key techniques used in the fabrication are spin coating, photolithography, PECVD, sputtering, reactive ion etching (RIE), and deep reactive ion etching (DRIE).

SPIN COATING

Spin coating is a technique used for uniformly depositing thin film onto flat surfaces. The process started by depositing a polymeric solution onto a substrate, which, in this case, is a silicon wafer. The substrate is then spun at high speed within a controlled time. The centrifugal force from the spinning motion spreads the solution across the substrate. The thickness of the coating can be controlled consistently based on the speed and duration of the spinning. Typically, the spin coating process is followed by a heat treatment to polymerize the solution to create a solid coating on the substrate. The viability of the spin coating process is determined by the viscosity of the solution and the chemical affinity between the substrate and the solution.

PHOTOLITHOGRAPHY

Photolithography is a technique used to accurately impart patterns onto a photosensitive film using ultraviolet (UV) light. A cycle of the photolithography process starts with

applying a photosensitive polymer called photoresist onto a wafer. Prior to the application of the photoresist, the wafer is baked at 130°C to remove the moisture on the surface, while hexamethyldisilazane (HMDS) vapor is applied to improve the adhesion of the photoresist to the substrate. The photoresist is spin-coated onto the treated wafer and then followed with a baking step to harden the photoresist. UV light is selectively applied onto the photoresist. The selectivity is achieved by using a photomask made of patterned chromium on a quartz plate to block the incident light from reaching the photoresist. The exposure is followed by a post-exposure baking step. Chemical reactions occur in the exposed parts of the photoresist during the baking process, which changes the solubility of the photoresist. The final step in photolithography is the development of the photoresist. The photoresist is exposed to a chemical developer, which will react differently to the exposed and non-exposed parts. The exposed parts in the positive photoresist and the unexposed parts in the negative photoresist are dissolved in the developer, thus transferring the pattern from the photomask to the photoresist. The patterned photoresist can be used to protect the layer underneath during the following etching process.

REACTIVE ION ETCHING

RIE is a technique used to anisotropically remove metal and dielectric films on a wafer. The anisotropic nature of the etching allows for the etching of smaller features compared to the use of wet chemical etching. During RIE, plasma is generated under a low-pressure environment by ionizing gasses using a coil. A wafer is placed within the chamber with mechanical or electrostatic clamping with helium cooling on the back of the wafer. A separate bias voltage accelerates the charged ions towards the wafer, chemically reacting and physically removing the target materials on the wafer. In combination with photolithography, photoresists can block the incoming ions, which then protect the underlying layer, thus transferring the pattern from the photoresist to the layer underneath.

DEEP REACTIVE ION ETCHING

Deep reactive ion etching is a variation of RIE with the purpose of creating deep structures with a high aspect ratio. DRIE is performed in a cyclical manner with three primary steps: passivation, breakthrough, and etching, as seen in Figure 3.10. During the passivation step, a thin layer of C_4F_8 is deposited on the wafer. The C4F8 also coats the sidewall and the bottom of the trench made in the preceding cycles. In the breakthrough step, a reactive ion etching is performed for a short duration to remove the C_4F_8 coating on the bottom surface of the trenches. Due to the directionality of the RIE, the coating on the surfaces perpendicular to the ion direction is etched faster than the sidewall. In the case of silicon etching, SF6 gas is used to generate fluorine radicals that will etch the exposed silicon on the bottom of the trench. The remaining coating on the sidewall serves as a protection layer, which improves the anisotropic nature of the etching. The cycle is then continued from the passivation step until the desired depth is achieved.

3.3.2. FABRICATION PROCESS OF THE SUBSTRATE THINNED DEVICES

The fabrication of the device started with a double-sided polished (DSP) (100) silicon wafer with a thickness of 300 μm. Using PECVD (Figure 3.11(a)), one side of the wafer

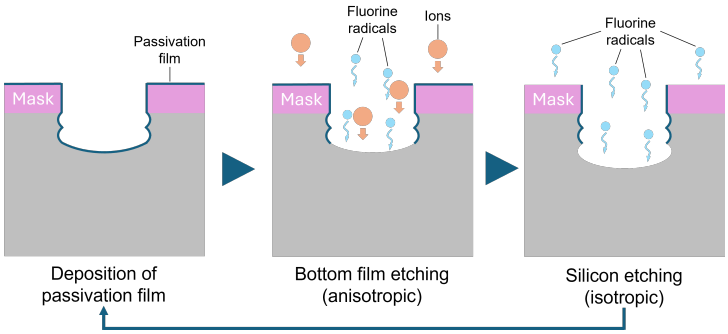

Figure 3.10: A schematic describing the cyclical process of DRIE starting with passivation, followed by a breakthrough of the passivation layer and etching of the silicon.

was coated with 2 μm silicon oxide, which will be used as a landing layer, and the supporting layer of the eventual membrane (Figure 3.11(b)). As the interconnects and pads, a 400 nm-thick aluminum with 1% silicon was deposited on the wafer using sputtering (Figure 3.11(c)). The inclusion of the 1% silicon was due to the availability of the material and was not critical in the process due to the minimal diffusion of silicon dioxide into aluminum. A layer of positive photoresist (SPR3012, MEGAPOSIT) with a thickness of 2.1 μm was spin-coated on the wafer using an automatic coater-developer (EVG120, EVG). Exposure of the photoresist was performed using a mask aligner (MA/BA8, Suss MicroTec). The photoresist was developed in the automatic coater-developer using a single puddle developer (MF-322, Microposit). The underlying aluminum layer was etched using RIE (Omega 201, Trikon). Following the etching, the photoresist was stripped from the wafer by using a plasma asher (PVA TePla 300, PVA TePla AG) and then cleaned in a 99% nitric acid bath. Another layer of 400 nm thick PECVD silicon dioxide was deposited to encapsulate the aluminum layer (Figure 3.11(d)). Contact openings were made by coating and patterning a layer of photoresist with a thickness of 2.1 μm, followed by etching of silicon dioxide in a buffered hydrofluoric acid (BHF 7:1) (Figure 3.11(e)). After photoresist stripping and wafer cleaning, the process was continued on the back side of the wafer by spin-coating 8 μm-thick photoresist (AZ-12XT-20PL-10, MicroChemicals GmbH). The photoresist was patterned to create the cavities for the air-backing layer underneath the transducers(Figure 3.11(f)). A DRIE of silicon on the back of the wafer was performed (Omega Rapier, SPTS Technologies). The depth and etch rate of the silicon etching were carefully monitored by using an optical profilometer (VK-250X, Keyence) (Figure 3.11(g)). Several membrane thicknesses of 0.8 μm, 20 μm, and 50 μm were made to see the effect of the membrane thickness on the performance of the transducers. The 0.8 μm membranes were made by etching completely the silicon layer, thus having a membrane consisting of 400 nm of silicon dioxide and 400 nm of aluminum. Afterward, the wafer was diced into individual dies. To ensure the survival of the membrane during the dicing process, the wafer was mounted with the membrane side facing the dicing foil. A dicing foil with UV-sensitive adhesive was used to allow for the release of the dies from the foil after UV exposure, thus minimizing the risk of membrane damage due to the adhesive. A glass cover plate was mounted on the cavity side of the dies. Non-conductive

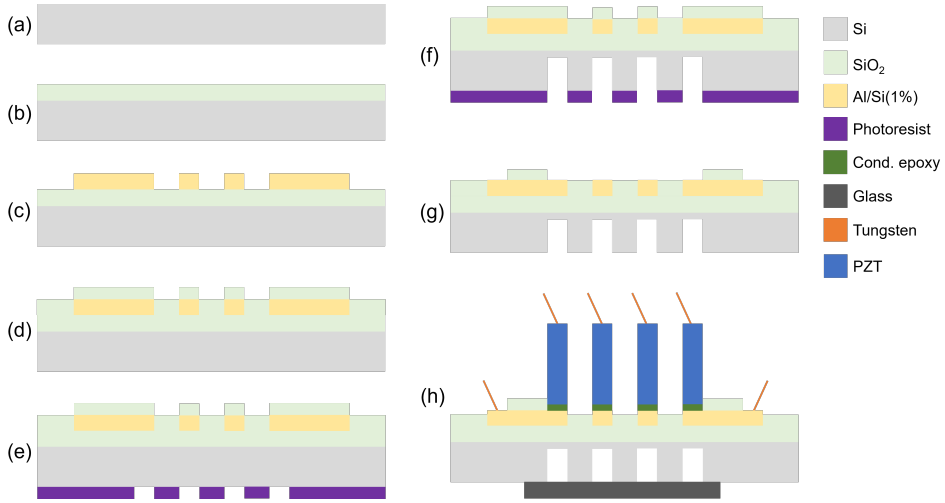

Figure 3.11: Process flow of substrate-thinned air backing layer. (a) The starting DSP 300 μm-thick wafer. (b) PECVD deposition of silicon oxide as substrate insulation. (c) Sputtering and patterning of the aluminum layer. (d) PECVD deposition of silicon dioxide as a passivation layer. (e) Patterning of the silicon dioxide to make contact openings with wet etching (f) spin-coating and photolithography of thick photoresist on the backside of the wafer. (g) DRIE of the backside of the wafer was followed by a cleaning step to remove the photoresist. (h) Post-processing of the wafer: dicing the wafer followed by attaching the glass cover and the PZT on the diced dies. Tungsten wires were bonded onto the contact pads and on top of the PZT with conductive epoxy.

epoxy (EPO-TEK 301-2FL, Epoxy technology) was used to bond the glass to the silicon and prevent liquid from entering the cavities. The epoxy was cured on a hotplate for 3 hours at 80°C. As the transducer, a film of pre-polled 270 um-thick PZT-5H (Piezo.com) was diced to 2.8 x 2.8 mm^2 to match the size of the contact pads on the silicon. These PZT pieces were mounted on the array and electrically connected to the pads by using silver-filled epoxy (EPO-TEK H20E, Epoxy technology). Tungsten wire with a diameter of 50 μm was attached on top of the PZT and the contact pads using the silver-filled epoxy. The tungsten wires were used to interface the driving signal to the transducers (Figure 3.11(h)). Tungsten wire was chosen due to its small footprint and excellent conductivity to minimize the impact of the wire bond, electrically and acoustically. Finally, encapsulation was needed to prevent electrical coupling and corrosion facilitated by the liquid medium. The encapsulation layer has to be thin and uniform to minimize attenuation and refraction, respectively. The entire device was encapsulated with 5 μm-thick CVD Parylene-C. Parylene-C was chosen due to its conformal and controllable deposition process at a few micrometer ranges. The finished devices can be seen in Figure 3.12.

3.3.3. CHARACTERIZATION OF THE INTEGRATED AIR BACKING LAYER

MEASUREMENT SETUP

The characterization of the transducer was performed using the setup sketched in Figure 3.13(a). The fabricated transducer was submerged in a 50 cm x 50 cm x 50 cm tank half-filled with deionized water and fixed to one of the tank walls by using a 3D-printed

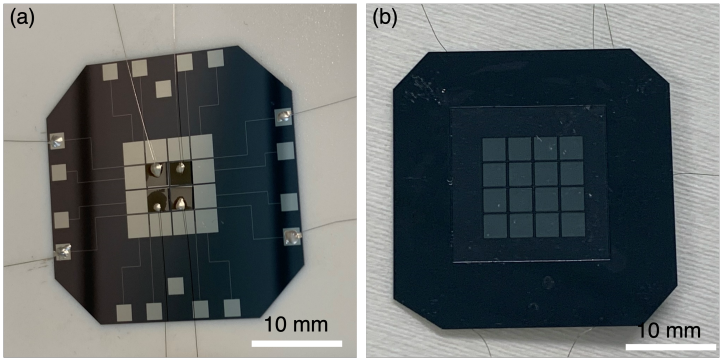

Figure 3.12: Photograph of the fabricated device with the transducers and wires mounted on the integrated air backing layer with 20 μm-thick membrane showing (a) the front side of the device and (b) the back side of the device.

holder. The transducer was connected to a function generator (DG4202, RIGOL), which provided the transducer with 10V driving signal. A needle hydrophone with a 1 mm tip diameter (NH1000, Precision Acoustics) was used to convert the pressure generated by the transducer at a given position into voltage. A photograph of the measurement setup can be seen in Figure 3.13(b). The output of the hydrophone was then displayed in an oscilloscope (DSO-X 3032A, Agilent Technologies). The hydrophone was pre-calibrated for the frequency range of 1-20 MHz. The needle hydrophone was mounted on a 3-axis motorized stage (VK-62000, GAMPT mbH) controlled by a stage controller (SFS630, GAMPT mbH). The motorized stage allows for precise positioning of the hydrophone to create a pressure map generated by the transducer. The movement of the hydrophone, data acquisition from the oscilloscope, and driving signal control in the function generator were done in a custom MATLAB GUI, which allows for synchronization of movement, driving bursts, and measurement in each location. A measurement protocol was then established by first finding the focal spot of the transducer by measuring it in the YZ plane with a large spacing that covers a large area. A low-resolution measurement in the XZ plane was done to check the focal distance and orientation of the transducer. A frequency sweep from 8 to 10 MHz was performed at the provisional focal spot to find the resonance frequency of the transducer. The driving frequency of the transducer was then set to its resonance frequency. After finding the focal spot coordinates and the resonance frequency, the acquisition of the YZ and XZ cross-sections with high resolution can be performed. During this study, four configurations of transducers with silicon thicknesses of 0.8, 20, 50, and 300 μm were fabricated. Within each configuration, four transducers were characterized.

TIME DOMAIN MEASUREMENTS

An example of the hydrophone readout can be seen in Figure 3.14(a). Electrical coupling between the transducer and hydrophone can generate electromagnetic interference (EMI), which can be seen in the hydrophone readout. The EMI can be seen in the oscilloscope instantaneously since it travels with the speed of light, while the ultrasound

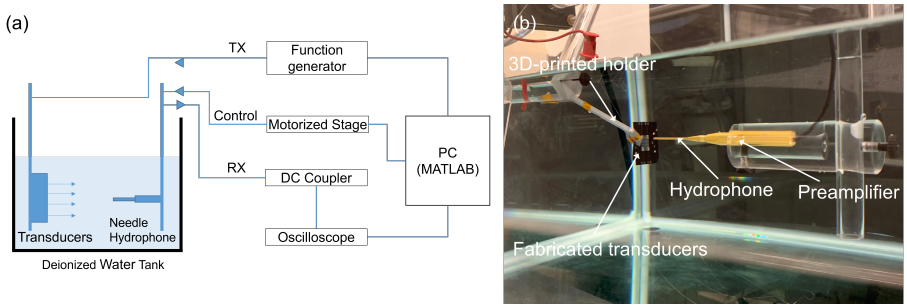

Figure 3.13: (a) Schematic of the measurement setup. (b) Photograph of the measurement setup with the 1 mm diameter hydrophone.

Table 3.3: Summary of the important parameters of the instruments used during the ultrasound characterization.

Parameters	values
Signal amplitude	10 V_{PP}
Driving frequency	8-10 MHz
Pulse repetition frequency	1 kHz
Signal per pulse	40
Oscilloscope averaging	16

pulse will be seen after a certain delay due to the much slower speed of sound. The distance between the hydrophone and the transducer can be calculated by dividing the time delay between the start of the driving signal burst and the burst seen in the hydrophone by the speed of sound in water. The ultrasound waves can be recorded twice due to reflection between the transducer and the hydrophone that propagate as follows: (1) the wave generated by the transducer propagated to the hydrophone which then recorded by for the first time, (2) the waves were partially reflected by the hydrophone back to the transducer, (3) the reflected waves were once again reflected by the transducer back to the hydrophone and recorded for the second time. This reflection can be identified by looking at the timing of the signal received to be approximately 3 times longer than the delay between the transducer and the hydrophone as seen in Figure 3.14(a), which corresponds to the 3 times longer pathway of the waves compared to the direct distance between the transducer and the hydrophone. During the comparison of each transducer, it is important to ensure that the EMI and the reflection do not overlap with the primary signal readout. This was done by ensuring a sufficient distance between the transducer and the hydrophone and also limiting the length of the bursts. The ultrasound pulse also has a transient period to reach a steady-state vibration as seen in Figure 3.14(b).

SPATIAL PROFILE MEASUREMENTS

A 2D cross-section of the beam profile generated by the transducer can be constructed by utilizing the motorized stage and the GUI to control the movement and data acquisition to create a raster map. The movement of the hydrophone during the acquisition

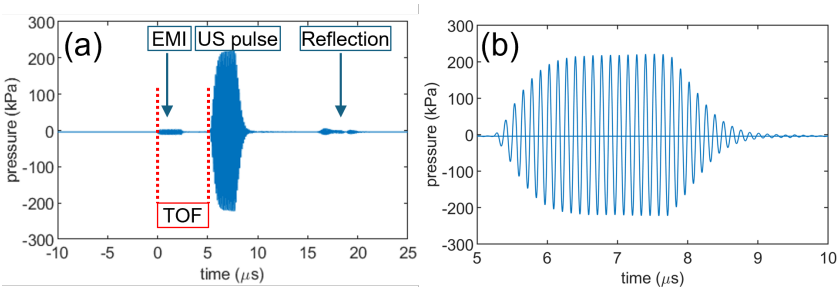

Figure 3.14: (a) A time domain measurement taken at the focal point of a transducer, showing the EMI, the ultrasound pulse, and the reflection of the pulse. (b) close-up view of the ultrasound pulse.

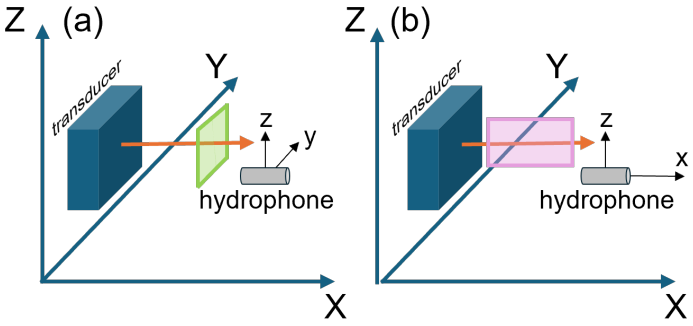

Figure 3.15: Schematics showing the acquisition process of a 2D cross-section of the acoustic beam profile in the (a) YZ plane and (b) XZ plane.

process in the YZ plane and XZ plane cross-sections can be seen in Figure 3.15(a) and (b).

The pressure information within an area was sampled into a grid of pixels with a determined spacing. In each pixel, time domain measurement was performed, and peak-to-peak pressure was measured to represent the data within the pixel. An example of the 2D cross-section in the YZ plane can be seen in Figure 3.16. The YZ cross-section provides information regarding defects in the transducer due to materials presence (e.g., epoxy, wire, air bubbles) or material defects (e.g., broken membrane or PZT) which would cause distortion in the generated acoustic field. It is vital to make sure that comparisons are made on samples with minimum distortion. The 2D cross-section in the XZ plane showed the focal distance of the transducer and also the orientation of the transducer relative to the hydrophone (Figure 3.17). To maximize the accuracy of the measurement, the transducer surface has to be parallel to the hydrophone tip, since misalignment of the orientation would cause a slanted beam profile in the XZ plane. Figure 3.18 shows the 2D cross-section in the YZ plane of the transducers with 0.8, 20, 50, and 300 μm membrane. In terms of pressure, the reference transducers with 300 μm-thick membrane showed the smallest output pressure in accordance with the FEM results. The membrane thickness did not affect the cross-section of the beam, with each

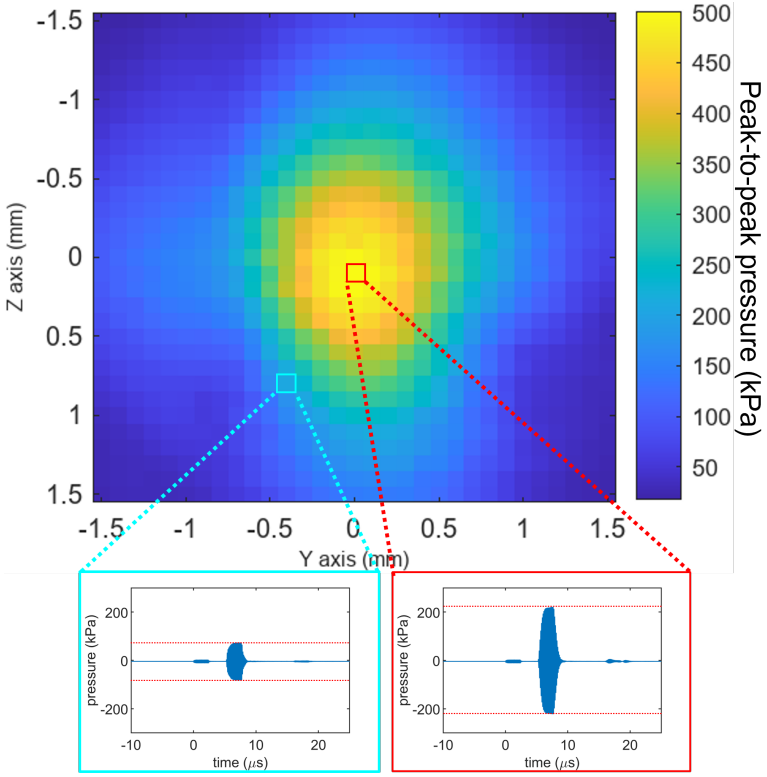

Figure 3.16: Example of a YZ plane cross-section, which was composed by taking the maximum peak-to-peak in the time domain in a raster map. A spacing of 0.1 mm was used.

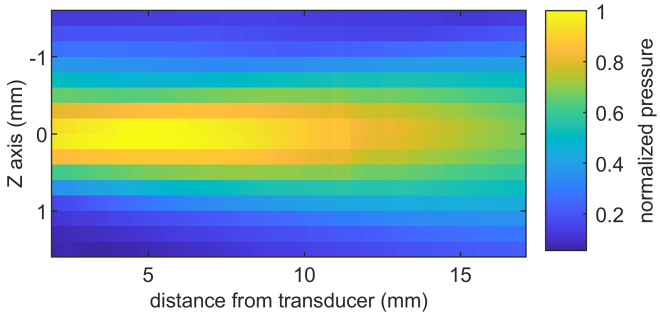

Figure 3.17: Example of an XZ plane cross-section with 0.2 mm resolution.

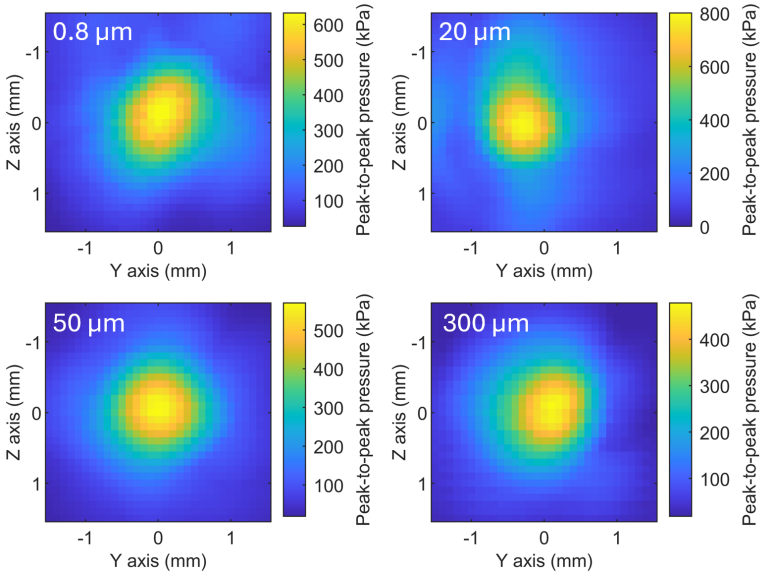

Figure 3.18: YZ plane cross-section of the transducers with 0.8, 20, 50, and 300 μm membrane thickness at its respective resonance frequency with scanning resolution of 0.1 mm.

transducer maintaining a similar shape and focal area in the YZ plane. The highest pressure was achieved by the configuration with 20 μm membrane thickness with a peak-to-peak pressure of 781 kPa.

FREQUENCY RESPONSE

At the volumetric focal spot, the frequency response of the transducer was measured by changing the driving frequency of the transducer between 8 and 10 MHz with a step of 0.1 MHz. The frequency response of a transducer will typically have a peak that corresponds with its resonance frequency. The sweep in frequency will affect the focal distance of the transducer in the order of 3 mm within the 2 MHz frequency range, as expected from equation Eq. 2.2. Since the transducers were unfocused, as seen in the XZ plane cross-section in Figure 3.17, this change in focal distance will have a minimum contribution to the change of the intensity. Figure 3.19 shows the frequency response of each configuration of the transducers. Along with changes in the intensity, the resonance frequency of the transducers was also influenced by the thickness of the membrane. The transducers with 20 and 50 μm membranes had lower resonance frequency on average compared to the transducers with 300 μm-thick substrate. A resonance frequency of 8.5 MHz was expected based on the thickness of the PZT film, which was shown by transducers placed on membranes. The reference transducers with 300 μm-thick silicon showed a higher mean resonance frequency at 9.13 MHz. This observation aligned with the study reported in metal-filled epoxy backing which the resonance frequency of the transducer became higher at denser backing layers [17],[18]. The results of a 0.8 μm-thick membrane were more distributed compared to other configurations. This was

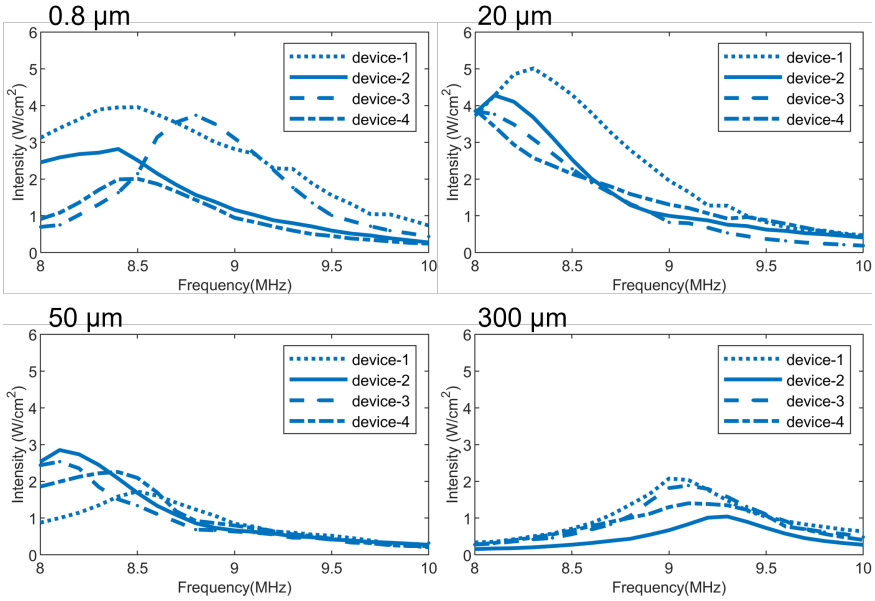

Figure 3.19: A 1D graph showing the acoustic intensity of the transducers as a function of frequency measured at the volumetric focal spot of the transducers with 0.8, 20, 50, and 300 μm membrane thickness, with four transducers measured for each category.

likely due to the lack of mechanical stability of the membranes, which are prone to cracking, especially during the operation of the transducer. Damage on the membrane during the operation of the transducer was challenging to observe because the PZT film and the adhesive applied supported the membrane.

3.3.4. DISCUSSION

The summary of the characterization of the integrated air-backing substrate can be seen in Table 3.4. The acoustic intensity of the transducers was influenced by the thickness of the silicon substrate underneath the piezoelectric element. The optimum membrane thickness to yield the highest output intensity was achieved by configuration with 20 μm-thick membrane. Compared to the reference group with 300 μm-thick silicon substrate, typically used in ASIC, the air-backed transducers consistently show an average improvement with a factor of 2.65 times when comparing the peak intensity at its respective resonance frequency. Similar to the comparison made in the FEM result, a comparison of the output intensities as a function of membrane thickness was also made assuming a fixed frequency which was the expected center frequency of 8.5 MHz. At a fixed frequency, the transducers with an air-backing layer showed a higher average improvement factor of 5.11 when compared to the reference transducers. The comparison between the simulated and measured output intensity as a function of substrate thickness can be seen in Figure 3.20. The experimental results showed a significant improvement in the output intensity by using the proposed integrated air-backing substrate. The

Table 3.4: The mean output intensity measured at the resonance frequency and at a fixed frequency of 8.5 MHz of transducer with different membrane thicknesses (n=4).

Membrane thickness (μm)	intensity at resonance - mean±SD (W/cm^2)	intensity at 8.5 MHz- mean±SD (W/cm^2)	Resonance frequency - mean±SD (MHz)
0.8	3.13±0.90	2.65±0.89	8.55±0.15
20	4.26±0.54	2.81±1.0	8.13±0.16
50	2.34±0.48	1.71±0.31	8.38±0.16
300	1.61±0.47	0.55±0.20	9.13±0.11

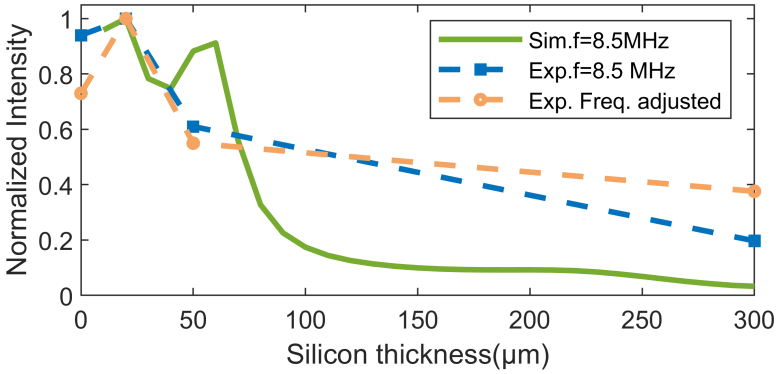

Figure 3.20: Comparison between the simulation and the experimental results at fixed frequency and adjusted at respective resonance frequencies

discrepancy with the simulation result can be attributed to the simplification of the simulation model and the difference in material properties used in the model and the measurement. The effect of the fabricated air-backing layer could also be suppressed due to the inclusion of conductive epoxy, which was manually applied on the top and the back of the transducers.

3.4. CONCLUSION

This chapter proposed an integrated air-backing layer in a silicon substrate that can be applied to a piezoelectric ultrasound transducer on ASIC to improve its transmit efficiency. Microfabrication techniques were used to thin the silicon substrate selectively underneath the transducers, thus creating a suspended membrane in the air. The thickness of the membrane presented a trade-off between improvement in output intensity and mechanical stability. Four configurations of devices with different silicon thicknesses were fabricated and characterized. The characterization of these transducers showed a consistent improvement when using the proposed integrated air-backing layer when compared to a transducer on 300 μm-thick silicon substrate. Both simulation and measurement showed the optimum membrane thickness of 20 μm, which, on average,

improved the output intensity of the transducers with a factor of 5.11 at 8.5 MHz driving frequency. The improvement can partially be attributed to the shift in resonance frequency of the transducer on a silicon substrate. However, regardless of the frequency shift, the air-backed transducers demonstrated an improvement over the reference at its respective resonance frequency with an improvement factor of 2.65. As a future work, the concept of the integrated air-backing layer will be implemented on PUTs-on-ASIC for ultrasound neuromodulation to improve its transmit efficiency.

BIBLIOGRAPHY

[1] G. K. Wardhana, M. Mastrangeli, and T. L. Costa, "Maximization of transmitted acoustic intensity from silicon integrated piezoelectric ultrasound transducers", in *Proceedings of 2022 IEEE International Ultrasonics Symposium*, 2022. DOI: 10.1109/IUS54386.2022.9957646.

[2] C. D. Herickhoff and R. van Schaijk, "Cmut technology developments", *Zeitschrift fur Medizinische Physik*, vol. 33, pp. 256–266, 3 Aug. 2023, ISSN: 18764436. DOI: 10.1016/j.zemedi.2023.04.010.

[3] D. M. Van Willigen, E. Kang, J. Janjic, *et al.*, "A transceiver asic for a single-cable 64-element intra-vascular ultrasound probe", *IEEE Journal of Solid-State Circuits*, vol. 56, pp. 3157–3166, 10 Oct. 2021, ISSN: 1558173X. DOI: 10.1109/JSSC.2021.3083217.

[4] Y. M. Hopf, B. W. Ossenkoppele, M. Soozande, *et al.*, "A pitch-matched transceiver asic with shared hybrid beamforming adc for high-frame-rate 3-d intracardiac echocardiography", *IEEE Journal of Solid-State Circuits*, vol. 57, pp. 3228–3242, 11 Nov. 2022, ISSN: 1558173X. DOI: 10.1109/JSSC.2022.3201758.

[5] T. Costa, C. Shi, K. Tien, J. Elloian, F. A. Cardoso, and K. L. Shepard, "An integrated 2d ultrasound phased array transmitter in cmos with pixel pitch-matched beamforming; an integrated 2d ultrasound phased array transmitter in cmos with pixel pitch-matched beamforming", *IEEE Transactions on Biomedical Circuits and Systems*, vol. 15, 4 2021. DOI: 10.1109/TBCAS.2021.3096722. [Online]. Available: https://www.ieee.org/publications/rights/index.html.

[6] P. A. Hager, D. Speicher, C. Degel, and L. Benini, "Ultralight: An ultrafast imaging platform based on a digital 64-channel ultrasound probe", *2017 IEEE International Ultrasonics Symposium (IUS)*, pp. 1–5, 2017. [Online]. Available: https://api.semanticscholar.org/CorpusID:44249570.

[7] C. Chen, Z. Chen, D. Bera, *et al.*, "A front-end asic with receive sub-array beamforming integrated with a 32 × 32 pzt matrix transducer for 3-d transesophageal echocardiography", *IEEE JOURNAL OF SOLID-STATE CIRCUITS*, vol. 52, 4 2017. DOI: 10.1109/JSSC.2016.2638433. [Online]. Available: http://ieeexplore.ieee.org..

[8] V. Pashaei, P. Dehghanzadeh, G. Enwia, M. Bayat, S. J. Majerus, and S. Mandal, "Flexible body-conformal ultrasound patches for image-guided neuromodulation", *IEEE transactions on biomedical circuits and systems*, vol. 14, pp. 305–318, 2 Apr. 2020, ISSN: 1940-9990. DOI: 10.1109/TBCAS.2019.2959439. [Online]. Available: https://pubmed.ncbi.nlm.nih.gov/31831437/.

[9] F. Ma, Z. Huang, C. Liu, and J. H. Wu, "Acoustic focusing and imaging via phononic crystal and acoustic metamaterials", *Journal of Applied Physics*, vol. 131, 1 Jan. 2022, ISSN: 10897550. DOI: 10.1063/5.0074503.

[10] P. B. Rosnitskiy, P. V. Yuldashev, O. A. Sapozhnikov, *et al.*, "Design of hifu transducers for generating specified nonlinear ultrasound fields", *IEEE Transactions on Ultrasonics, Ferroelectrics, and Frequency Control*, vol. 64, pp. 374–390, 2 Feb. 2017, ISSN: 08853010. DOI: 10.1109/TUFFC.2016.2619913.

[11] H. Shankar and P. S. Pagel, "Potential adverse ultrasound-related biological effects: A critical review", *Anesthesiology*, vol. 115, pp. 1109–1124, 5 2011, ISSN: 15281175. DOI: 10.1097/ALN.0b013e31822fd1f1.

[12] Y. Wang, J. Tao, F. Guo, *et al.*, "Magnesium alloy matching layer for high-performance transducer applications", *Sensors (Switzerland)*, vol. 18, 12 Dec. 2018, ISSN: 14248220. DOI: 10.3390/s18124424.

[13] J. Jang and J. H. Chang, "Design and fabrication of double-focused ultrasound transducers to achieve tight focusing", *Sensors (Switzerland)*, vol. 16, 8 Aug. 2016, ISSN: 14248220. DOI: 10.3390/s16081248.

[14] S. Moazeni, E. H. Pollmann, V. Boominathan, *et al.*, "19.2 a mechanically flexible implantable neural interface for computational imaging and optogenetic stimulation over 5.4×5.4mm 2 fov", in *2021 IEEE International Solid-State Circuits Conference (ISSCC)*, 2021, ISBN: 9781728195490. DOI: 10.1109/ISSCC42613.2021.9365796.

[15] S. Zucca, M. Manghisoni, L. Ratti, *et al.*, "Effects of substrate thinning on the properties of quadruple well cmos maps", *IEEE Transactions on Nuclear Science*, vol. 61, pp. 1039–1046, 2 2014, ISSN: 00189499. DOI: 10.1109/TNS.2014.2307960.

[16] J. Blackmore, S. Shrivastava, J. Sallet, C. Butler, and R. Cleveland, "Ultrasound neuromodulation: A review of results, mechanisms and safety", *Ultrasound in Medicine and Biology*, vol. 45, 7 2019, ISSN: 0301-5629. DOI: 10.1016/j.ultrasmedbio.2018.12.015.

[17] A. A. Abas, M. P. Ismail, S. Sani, and M. N. I. Ahmed, "Effect of backing layer composition on ultrasonic probe bandwidth", in *RnD Seminar 2010: Research and Development Seminar 2010*, Bangi, Malaysia: Malaysian Nuclear Agency, 2010, p. 5.

[18] S. T. Siewe, S. Callé, F. V. Meulen, *et al.*, "High acoustic impedance and attenuation backing for high-frequency focused p(vdf-trfe)-based transducers", *Sensors*, vol. 23, 10 May 2023, ISSN: 14248220. DOI: 10.3390/s23104686.

4

POLYMER METAL CONNECTION

This chapter introduces a novel polymer-metal connection (PMC) method to implement top-level electrical connections on a piezoelectric ultrasound array. This approach utilizes a microfabricated PDMS/Ti/Al membrane supported by a silicon frame, replacing traditional top connections that introduce significant acoustic losses. The key finding is the significant improvement in preserved output intensity (80%) compared to an ideal reference, contrasting with the state-of-the-art aluminum foil connection, which only achieves 22.5%. The PMC was successfully implemented on a 2x2 transducer array and validated through preliminary biological testing, demonstrating its ability to stimulate neuronal and endothelial cells.

Parts of this chapter have been published in [1].

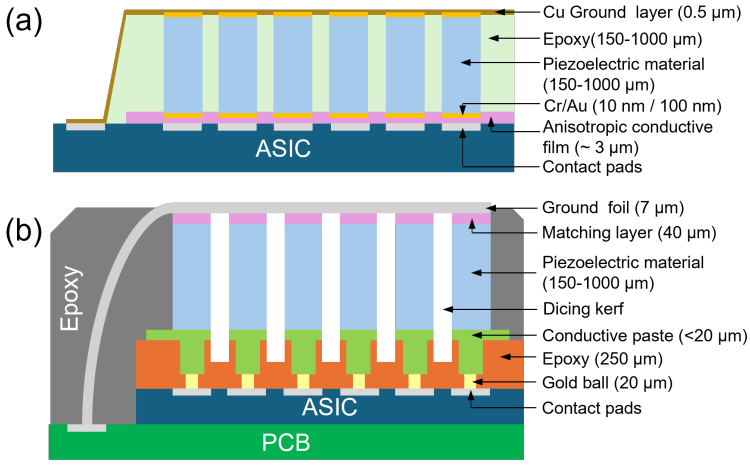

Figure 4.1: The schematic of top metal connection implementation using (a) dice-and-fill [4] and (b) using aluminum ground foil [2].

4.1. INTRODUCTION

TOP CONNECTION OF PIEZOELECTRIC ULTRASOUND TRANSDUCERS

The previous chapter discussed methods for improving the transmit efficiency of a piezoelectric ultrasound transducer through silicon substrate engineering. However, the transducer implementation still relied on individual wires placed on top of each piezoelectric element, which is impractical and not scalable. Therefore, implementing the top connection in a piezoelectric ultrasound transducer is another crucial aspect. As previously discussed, driving a piezoelectric element as an ultrasound transducer requires the application of an alternating electric field. In phased array ultrasound transducers, piezoelectric elements are integrated into an IC, and the bottom side of the piezoelectric element connects to the IC's contact pads [2],[3],[4]. These contact pads supply each element in the array with phase-varied alternating voltages to focus and steer the generated ultrasound waves. To complete the electrical circuit, the top side of each piezoelectric element connects to a common ground node, which is then connected back to the IC or PCB [2],[3]. Therefore, a vertical connection as thick as the piezoelectric film is needed, which, depending on the desired resonance frequency, can range from a few hundred micrometers to a few millimeters. This thickness can be challenging to implement, especially when using thin film technology in microfabrication processes [4],[5].

4.1.1. STATE-OF-THE-ART TOP CONNECTION

Several works have implemented piezoelectric transducers on ASICs [2],[4],[3],[5],[6]. However, current top connection implementations are not optimized for transmit efficiency [2]. Generally, there are two main approaches. The first approach involves using conductive aluminum foil (7–15 μm-thick) glued to the top of the array with conductive paste [2],[3], as seen in Figure 4.1(b). The foil can be directly interfaced with open

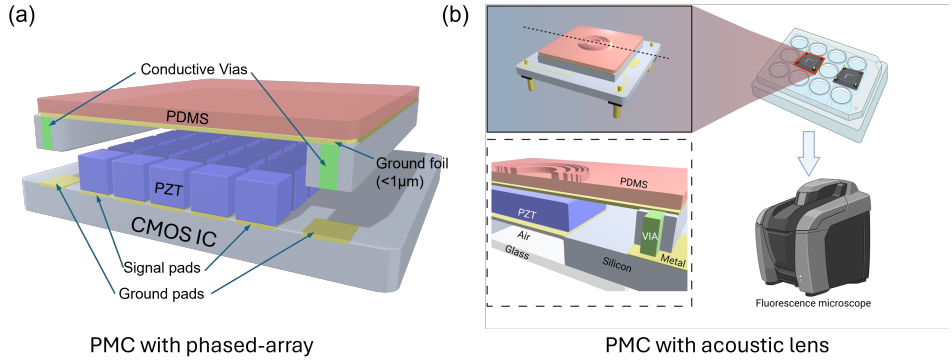

Figure 4.2: The schematic of the PMC concept used in two scenarios: (a) the PMC on an array of transducers which use phased-array to focus and (b) the PMC on a single element transducer which use an acoustic lens to focus.

pads on the IC or PCB using a similar conductive paste (Figure 4.1(b)) [2], [3]. Despite its thinness, the aluminum introduces an additional interface that can cause reflection and propagation attenuation. This approach, used in an imaging array, showed a low transmit efficiency of 6 kPa/V [2], far from the 80 kPa/V [7] efficiency demonstrated by a piezoelectric transducer array with discrete components. The second approach is dice-and-fill [4], [5], where the dicing kerfs (small gaps) between array elements are filled with a non-conductive material, such as epoxy, to planarize the array surface. A thin metal layer (<1 μm-thick) is then deposited onto the planarized surface to create a common ground connection (Figure 4.1(a)). Although this approach minimizes losses from the top metal layer, the epoxy within the kerfs could dampen piezoelectric vibrations, reducing transducer efficiency. This implementation exhibited a higher transmit efficiency of 20 kPa/V [4], though differences in the backing layer may also contribute to this difference. Therefore, the ideal top connection to maximize transmit efficiency should be a combination of the two approaches where a thin layer of metal is placed on top of the transducer to minimize without using kerf filler, which could dampen the vibration of the piezoelectric element.

4.1.2. IDEAL TOP CONNECTION

We envision a platform enabling scalable top-level connections for piezoelectric transducers. This scalability allows for various piezoelectric film thicknesses, enabling operation at different ultrasound frequencies. The platform should be implementable for a single or multiple elements Figure 4.2(a-b). This design builds upon the concepts of an air-backing layer (Chapter 3) and a lossless top connection. The acoustically lossless top connection also creates space on the transducer surface for an acoustic lens, offering a cheaper and more accessible alternative to phased array focusing. Lens implementation will be discussed in the following chapter. This chapter focuses on the design and proof-of-concept of acoustically lossless top connection, and validation of the concept was mainly performed with single-element transducers. The validation of the concept

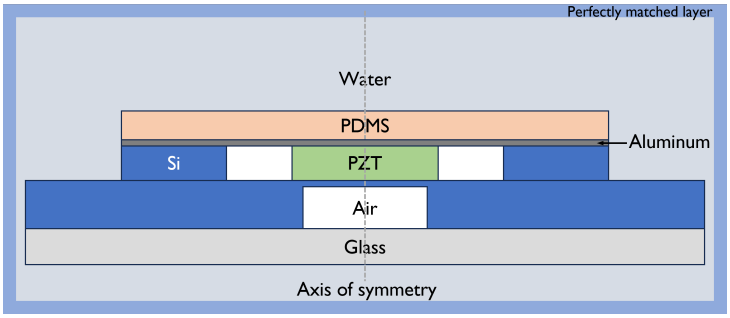

Figure 4.3: Schematic of the simulation setup of the PMC used in COMSOL Multiphysics.

was later performed on a 2x2 array.
The acoustically lossless connection consists of a customizable frame with conductive vias and a thin metal sheet serving as the common ground connection. A sub-micrometer metal layer lacks the mechanical support to cover the typical mm² aperture size needed for a focal distance of a few millimeters. Therefore, mechanical support is needed to prevent breakage of the thin metal layer. This mechanical support must be flexible to avoid dampening piezoelectric vibrations and acoustically-transparent to maximize transmit efficiency. Combining a polymer supporting layer and the thin metal layer creates the polymer-metal connection (PMC). This approach provides a scalable and efficient solution for top-level connection in piezoelectric transducers. Polydimethylsiloxane (PDMS) is a widely used polymer in microfabricated biomedical devices, such as soft encapsulation of implants [8] and organ-on-chip applications [9], due to its biocompatibility. Its fabrication using thin-film technology allows for accurate deposition control of sub-millimeter-thick layers. Additionally, its acoustic impedance is similar to that of water and soft tissue, minimizing reflection when interfaced with liquid media. This combination of properties makes PDMS a suitable candidate for the supporting polymer layer in the PMC. In combination with PDMS, aluminum is a suitable candidate for the metal layer due to its high conductivity and compatibility with microfabrication processes.

4.2. DESIGN OF PMC

4.2.1. SIMULATION SETUP

A finite element model in COMSOL Multiphysics was used to design the PMC concept. The transducer consists of three components: the air-backed substrate, the piezoelectric element, and the PMC (Figure 4.3). An axisymmetric model utilizing three physics modules (electrostatics, solid mechanics, and pressure acoustics) was used for the simulation. The electrostatics and solid mechanics modules simulated the piezoelectric effect, which acted as the acoustic source in the model. The propagation of acoustic waves in the field was then simulated by the pressure acoustic module while taking into account the acoustic attenuation. The frequency-domain simulation analyzed the harmonic steady-state of the model in a water propagation medium. A perfectly-matched layer (PML) on the outer boundaries of the model prevented reflections due to the finite

Table 4.1: key simulation parameters for the PMC simulation.

Parameter	Value
Frequency	8.5 MHz
Maximum mesh size	$\lambda_{medium}/10$
Mesh shape	Quadrilateral
PZT thickness	0.27 mm
PZT radius	1.5 mm
Silicon substrate thickness	0.3 mm
Silicon membrane thickness	0.02mm
Attenuation in PDMS [10]	4.3 dB/cm/MHz
PDMS acoustic impedance	1.045 MRayl
Attenuation in Al [11]	0.07 dB/cm/MHz
Al acoustic impedance	8.37 MRayl

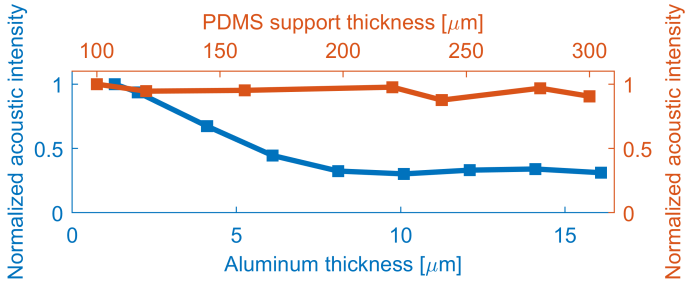

Figure 4.4: The acoustic intensity of the simulated transducer as a function of the PDMS thickness and the Aluminum thickness normalized to the intensity at minimum thickness.

simulation space. The important parameters of the model are shown in Table 4.1.

4.2.2. EFFECT OF MEMBRANE THICKNESS

Integral to the PMC concept is the polymer-metal stack that serves as the top connection of the piezoelectric transducer. The relationship between the layer thickness of the metal and polymer and the transducer output intensity was observed. The aluminum and PDMS layers in the PMC were swept individually, and their effects on the output intensity at the focal spot were observed. The PDMS thickness was varied between 100 μm and 300 μm, while the aluminum layer thickness was varied between 1 μm and 16 μm. PDMS has a much higher attenuation coefficient (4.3 dB/cm/MHz) than aluminum (0.07 dB/cm/MHz). As shown in Figure 4.4, the PDMS thickness has minimal effect within this thickness range. A 10% drop in output intensity was observed when comparing 100 μm-thick PDMS to 300 μm-thick PDMS. In contrast, the aluminum thickness significantly affected the transducer's output intensity. The normalized output intensity decreased linearly with a rate of $0.1/\mu m$ up to 8 μm thickness and then plateaued at approximately 30% output intensity. The loss when using the aluminum layer was dominated by the acoustic reflection due to the mismatch between PZT-Al-Water, which theoretically ex-

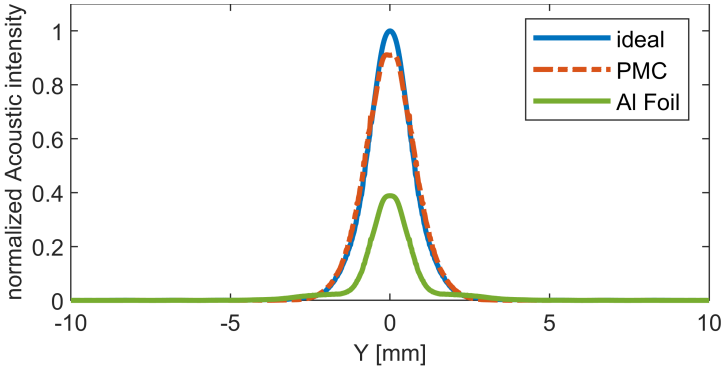

Figure 4.5: The simulation result comparing an ideal transducer, transducer with PMC top connection and transducer with 15 μm Aluminum top connection.

hibits a 0.32 intensity transmit coefficient (Eq. 2.3). These results demonstrate the importance of minimizing aluminum thickness to improve the transducer's output intensity.

4.2.3. COMPARISON WITH STATE OF THE ART

The performance of PMC was compared to two reference simulations: an ideal condition and a ground foil top connection with 15 μm-thick aluminum. The reference simulations used the same model as in Figure 4.3, replacing the PDMS and aluminum layers with water for the ideal condition and with 15 μm-thick aluminum for the ground foil. The comparison results, shown in Figure 4.5, indicate that the ground foil reduces the output intensity by 61.2% compared to the ideal reference. For the PMC, a 100 μm-thick PDMS and 1 μm-thick aluminum layer resulted in a 10% loss in output intensity compared to the ideal reference. These simulations exemplify the need to reduce the metal layer thickness, which significantly affects the transmit efficiency of piezoelectric ultrasound transducers. Using PDMS as a mechanical support for the sub-micrometer metal film is promising from an acoustic perspective. A free-standing 100 μm-thick PDMS layer was mechanically stable enough for use as a soft implant [8]. Based on these promising simulation results, it was decided to proceed with the experimental validation of this concept using a 100 μm-thick PDMS layer and a thin metal layer.

4.3. FABRICATION OF PMC

4.3.1. FABRICATION FLOW

The PMC device fabrication process is illustrated in the flowchart in Figure 4.6. Fabrication began with double-sided polished (DSP) wafers matching the thickness of the piezoelectric material (Figure 4.6(a)). Fine thickness control of the wafer can be achieved using deep reactive ion etching (DRIE) or chemical-mechanical polishing (CMP). A 4 μm-thick silicon dioxide layer was deposited on the top side of the wafer using plasma-enhanced chemical vapor deposition (PECVD) (Figure 4.6(b)). This silicon dioxide layer served as a landing layer for the subsequent DRIE process and as temporary support

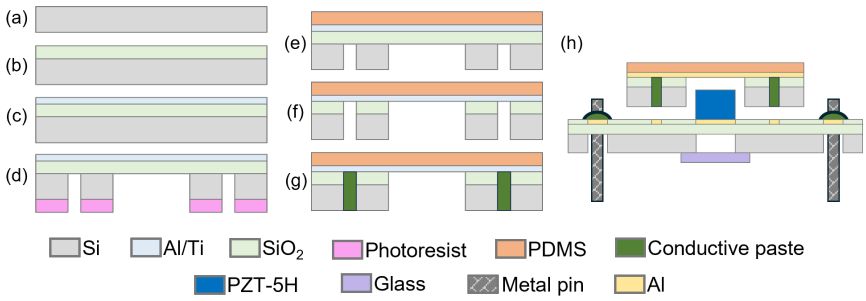

Figure 4.6: The schematic of the PMC fabrication flow: (a) Process start with a DSP wafer, (b) silicon oxide deposition, (c) Al/Ti deposition, (d) DRIE on the backside of the wafer with thick photoresist masking layer, (e) PDMS deposition, (f) silicon dioxide wet etching, (g) conductive paste application into the trenches to create conductive vias,and (h) assembly of the PMC onto an air-backed substrate and PZT.

for the metal membrane before polymer support deposition. A 400 nm-thick aluminum layer was deposited using sputtering, followed by a 50 nm-thick titanium layer, both at 50 °C (Figure 4.6(c)). An 8 μm-thick layer of AZ12XT photoresist (MicroChemicals GmbH) was spin-coated and patterned using photolithography on the backside of the wafer. DRIE of the silicon was performed on the backside of the wafer using an Omega Rapier (SPTS Technologies) with the previously deposited silicon dioxide as the landing layer (Figure 4.6(d)). Due to the thickness of the silicon oxide, the silicon layer was over-etched to ensure complete removal and prevent it from blocking access to the underlying aluminum layer in the subsequent process. The etching depth was monitored using an optical profilometer (VK-250X, Keyence). The etching continued until the trench depth remained constant, indicating that the silicon dioxide layer had been reached (Figure 4.7(b)). After DRIE, the photoresist was stripped using a PVA TePla 300 plasma asher (PVA Tepla AG). To prevent damage to the fragile membrane during the pumping and venting process, the wafer was placed horizontally. During DRIE, some lateral titanium etching can occur due to fluorine gas leakage to the backside of the wafer (Figure 4.7(a)). However, this effect was negligible, as it was confined to the wafer's corners. The wafer was cleaned in a 100% HNO_3 bath and rinsed with deionized water. A 100 μm-thick layer of PDMS (Sylgard 184, Dow) was spin-coated on the metal side of the wafer (Figure 4.6(e)). The PDMS, mixed with a 10:1 ratio of monomer and curing agent, was mixed and degassed (ARE-250, Thinky). The PDMS was cured at 90 °C for 1 hour in a convection oven. After curing the PDMS, the silicon dioxide layer was removed using buffered hydrofluoric acid (BHF). Due to the relatively thick silicon dioxide layer, the estimated etch duration was 13 to 16 minutes, assuming an etch rate of 250-300 nm/minute for PECVD silicon oxide (Figure 4.6(f)). The wafer was mounted membrane-side down on dicing foil with a UV release mechanism (ELEGRIP, Denka) to enable release of the diced PMC without damaging the membrane (Figure 4.7(c)). After dicing, the PMC was placed membrane-side down on a Teflon plate, and the cavities on the sides were filled with silver conductive paste (AA42469) to create conductive vias (Figure 4.7(d)). The conductive paste was applied to the cavities using a brush, planarized to the cavity openings using a razor blade, and cured on a hotplate at 93 °C for 15 minutes (Figure 4.6(g)). Due

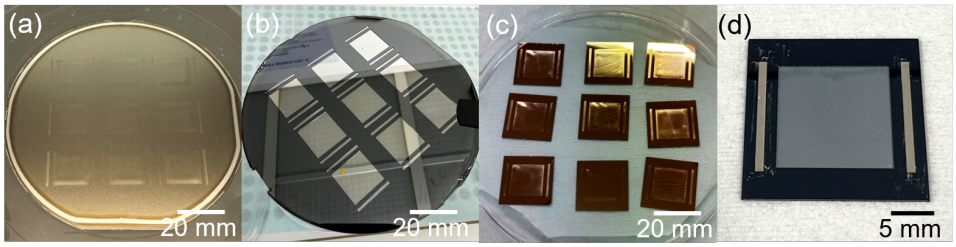

Figure 4.7: Fabrication of the PMC at different stages of processing: (a) top side view of the PMC wafer after DRIE, (b) back side view of the PMC wafer after DRIE. (c) the PMC after dicing, and (d) the PMC with the conductive vias filled with conductive epoxy.

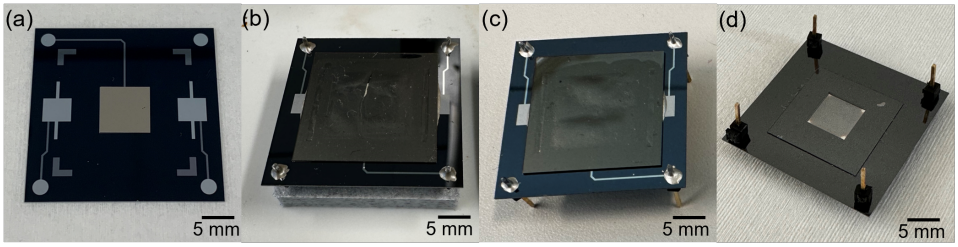

Figure 4.8: Assembly of a piezoelectric transducer with PMC and an air-backed substrate: (a) air-backed substrate with PZT element, (b) pin mounting using a 3D-printed aligner, (c) top view of the assembled transducer with PMC, and (d) back view showing the air-backed membrane and pin connections.

to shrinkage during curing, the conductive paste application and curing process were repeated twice to ensure complete filling of the cavities. Membrane conductivity, measured between the two vias, ranged from 0.8 to 1.6 Ω.

4.3.2. ASSEMBLY OF PMC ON AIR-BACKED SUSBTRATE

The PMC can be integrated with an air-backed substrate (Chapter 3). The design of the interconnects on the substrate was altered to allow for compatibility with the PMC. The new design included two ground pad connections that align with the PMC design, with contact pads that can be interfaced with pin connections to allow for easier electrical interfacing (Figure 4.8(a)). The integration of the PMC to the substrate started with an air-backed substrate that housed PZT elements placed on top of a hot plate (Figure 4.6(h)). To attach the PMC on top of the substrate, silver conductive paste (42469, Alfa Aesar) was thinly spread on the PZT elements, and conductive epoxy (EPO-TEK H20e, Epoxy technology) was applied onto both ground pads. Conductive epoxy was used due to its higher mechanical strength compared to conductive paste. Curing was performed in two stages: the first stage at 95 °C for 15 minutes to cure the conductive paste, followed by 80 °C for 3 hours to bake the conductive epoxy. Conductive pins can be inserted into the contact pads. A custom printed structure was used to assist in supporting and aligning the pins (Figure 4.8(b)). The pins were bonded using conductive epoxy and cured for 2.5 hours at 120 °C on a hot plate while enclosed in a glass chamber, followed by an-

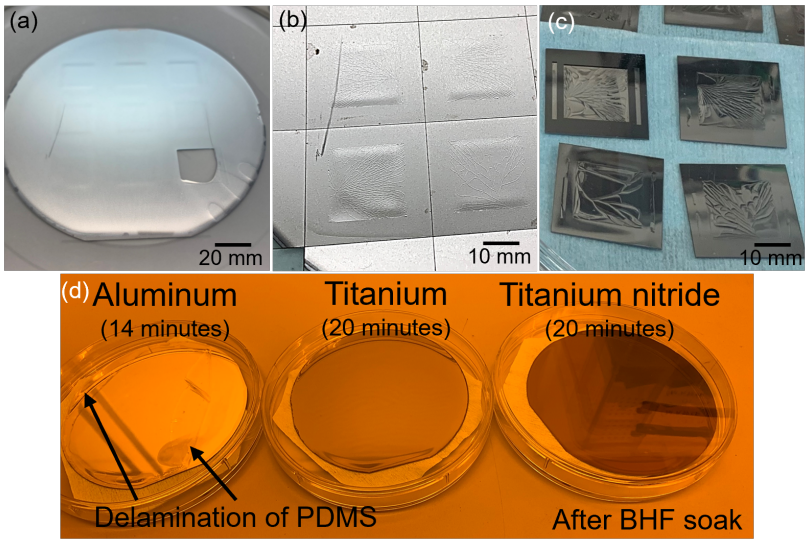

Figure 4.9: Challenges encountered during PMC fabrication: (a) PMC wafer with an aluminum metal layer before dicing. (b) Close-up of the PMC wafer after dicing, showing cracks in the aluminum layer caused by stress during the process. (c) Individual PMC after release from the dicing foil. (d) PDMS adhesion on aluminum, titanium, and titanium nitride substrates after BHF soak, demonstrating improved adhesion with titanium and titanium nitride.

other hour of curing at 100 °C with the device placed upside down in a similar setup. The higher temperature was used to compensate for the gap between the epoxy and the surface of the hotplate. The resulting transducer can be seen in Figure 4.8(c & d). The final step of the fabrication was to coat the device with 5 μm-thick of Parylene to waterproof the device during characterization.

4.3.3. FABRICATION CHALLENGES

During the development of the PMC fabrication process, aluminum was initially used as the metal layer. However, challenges arose due to PDMS delamination from the aluminum during the extended BHF soak required to etch the silicon dioxide layer (Figure 4.9(d)). An alternative fabrication process was explored, involving dicing the wafer before exposing the backside of the chip to BHF. However, during dicing, the combination of vacuum from the substrate and dicing stress caused the silicon dioxide layer to crack, with cracks propagating to the aluminum layer (Figure 4.9(a-c)). The use of an alternative metal, either titanium or titanium nitride, was considered. Sheet resistance was measured using a four-point probe (Resmap 178, CDE). Both titanium and titanium nitride exhibited significantly higher sheet resistance than aluminum (Table 4.2). The high resistance can cause a voltage drop in the driving signal, potentially reducing transducer transmit efficiency. However, stacking the metal on top of an aluminum layer could leverage the conductivity of aluminum and the adhesion properties of the alternative metal to PDMS. PDMS adhesion in BHF was tested using three wafers: one without

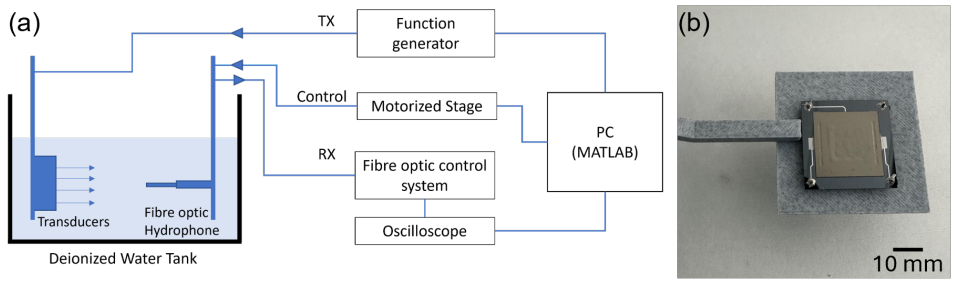

Figure 4.10: (a) Schematic of ultrasound characterization setup. (b) the fabricated transducer mounted on a 3D printed holder.

an adhesion layer, one with a 50 nm titanium adhesion layer, and one with a 50 nm titanium nitride adhesion layer. The PDMS on wafers with titanium and titanium nitride adhesion layers remained adhered for over 20 minutes in BHF, while the PDMS on aluminum delaminated after only 14 minutes (Figure 4.9(d)). Based on these results, an Al/Ti stack was selected as the metal layer in the PMC to ensure both conductivity and adhesion during the fabrication process.

Table 4.2: Sheet resistance measurement of metal stacks.

Parameter	Al	Ti	Al/Ti	TiN	Al/TiN
Thickness (nm)	400	400	400/50	400	400/50
Sheet resistance (Ω/sq)	0.03	1.2	0.05	5.5	0.08

4.4. ULTRASOUND CHARACTERIZATION

4.4.1. CHARACTERIZATION SETUP

The schematic of the measurement setup can be seen in Figure 4.10(a). The fabricated transducer was fixed in the tank half-filled with de-ionized water on a 3D-printed holder as shown in Figure 4.10(b). The transducer was driven by a function generator (DG4202, RIGOL) which was controlled by a custom MATLAB interface. A fiber optic hydrophone (FOHS V2, Precision Acoustics) mounted on an XYZ motorized stage (VK62000, GAMPT mbH) was used to measure the ultrasound waves generated by the transducer and characterize the pressure field. The readout of the hydrophone was collected by an oscilloscope (DSO-X 3032A, Keysight), and the data was integrated into a custom MATLAB interface. The voltage readout collected from the oscilloscope was compared to the calibration data of the hydrophone to convert it into acoustic pressure and intensity. The signal used to characterize the transducers was bursts of 40 square waves with an amplitude of 10 Vpp and pulse repetition frequency (PRF) of 1 kHz; this PRF was chosen to give sufficient delay to avoid interference from the previous burst.

4.4.2. EFFECT OF EPOXY KERF FILLING

A measurement was conducted to assess the effect of kerf filling on the pressure generated by a transducer. This investigation is crucial for understanding the impact of different fabrication techniques on transducer performance. Measurements were performed on 2.8 x 2.8 mm² PZT transducers on a silicon substrate with a 50 μm-thick tungsten wire top connection. One group of transducers had their sides coated with non-conductive epoxy (EPO-TEK 301-2fl, Epoxy technology) cured at 80 °C for 3 hours, while the other group served as a reference. A clear drop in output pressure was observed at the transducer focal distance when comparing the two groups. The transducers with epoxy surrounding the PZT element generated only 19.8% of the output pressure compared to the reference group. This result aligns with the low output pressure obtained in [4], which utilized a dice-and-fill approach using similar epoxy material. Therefore, the dice-and-fill approach is not suitable for acoustically efficient transducer design. The reduced pressure output likely stems from the epoxy mechanically damping the PZT vibrations and hindering efficient energy transfer to the surrounding medium.

4.4.3. PERFORMANCE OF PMC

To evaluate the experimental performance of the PMC, its performance was compared to that of an aluminum foil top connection. A 10 x 10 mm² PZT transducer was used for the comparison. The cross-section of the intensity field parallel to the transducer surface was taken at the focal distance. A transducer with 50 μm-thick tungsten wire connection served as an ideal reference, mimicking the ideal condition (Figure 4.12(a)). The wire was placed on the edge of the PZT with a minimal footprint to minimize interference with the acoustic field. A 15 μm-thick aluminum foil was used, consistent with the thickness used in the simulation (Figure 4.5). The performance of the transducer with the aluminum foil top connection can be seen in Figure 4.12(b). Figure 4.12(c) shows the performance

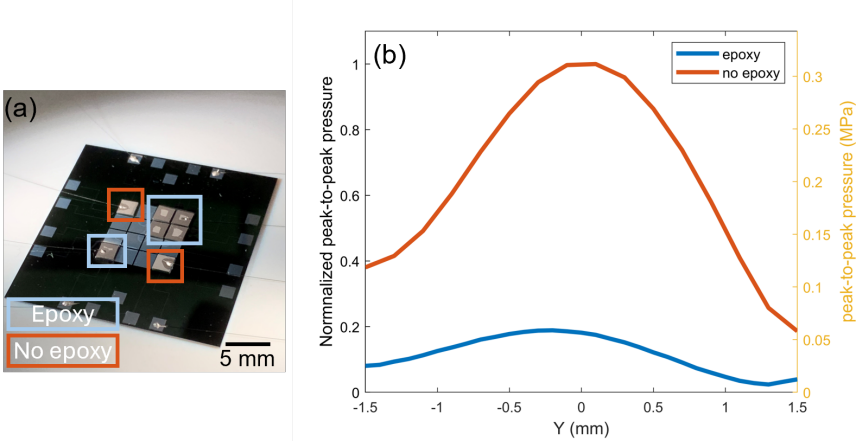

Figure 4.11: (a) The transducer used to observe the effect of kerf filling. Transducers indicated in blue were coated on the side with epoxy, while transducers indicated in orange were used as reference. (b) The 1D plot of the output pressure measured across the focal spot compares the transducer with and without epoxy.

of the transducer with PMC top connection. A 1D plot of the intensity along the Y-axis across the focal spot was extracted from the cross-sectional intensity field of each transducer, as shown in Figure 4.12(d). The measurement results reasonably matched the simulation results in Figure 4.5. As expected, the reference generated the highest intensity, followed by the transducer with PMC, which exhibited a 20% reduction. The use of PMC significantly improved the performance compared to the transducer with a 15 μm-thick aluminum foil connection, which generated 77.5% less intensity than the reference. Comparing the intensity field profiles of the reference (Figure 4.12(a)) and the PMC transducer (Figure 4.12(c)) shows that the PMC did not cause distortion to the intensity field. These findings highlight the effectiveness of the PMC concept as a top metal connection for ultrasound transducers.

4.4.4. PMC ON A TRANSDUCER ARRAY

To assess the feasibility of implementing the PMC concept on an array, a 2x2 array of 2.8 x 2.8 mm² PZT elements was fabricated with a PMC. The PMC was placed on top of the PZT array after applying conductive paste to the membrane. To ensure bonding between the PZT array and the PMC membrane, a circular acrylic mass (weighing approximately 0.1 gram) was placed on top of the array during curing. The characterized output intensity of the transducer at a 12 mm distance is shown in Figure 4.13(c). The intensity profile shows four distinct focal spots with relatively similar amplitudes. The top right focal spot generated the highest intensity, while the bottom right focal spot generated the lowest. Non-uniform contact between the array elements and the PMC may have caused the intensity differences. Additionally, the uneven surface of the PMC, particularly the imprint from the weight, could have caused refraction of the generated waves. Despite these variations, this result demonstrates the feasibility of applying PMC to an array of transducers. Future work could focus on improving the uniformity of the PMC and optimizing the bonding process to minimize intensity variations across the array's elements. Optimization of the bonding process between the PMC and the PZT array can be achieved by using a pick-and-place tool that allows for controllable and uniform force across the PZT elements during the application. The pick-and-place is also instrumental in scaling down the PMC to work on smaller transducer arrays, which require higher precision and capability to handle smaller PMC structures. This successful implementation of the PMC on an array opens possibilities for developing more complex and efficient ultrasound transducer arrays for various applications.

4.5. PRELIMINARY BIOLOGICAL VALIDATION

Preliminary biological validation of ultrasound neuromodulation using the transducer with PMC was performed in collaboration with the Leiden University Medical Center. Fluorescence calcium imaging was performed using a BZ-X800 (Keyence) on human induced pluripotent stem cell (hiPSC)-derived neurons and human umbilical vein endothelial cells (HUVECs). These cell types were chosen for their relevance in studying neuronal and vascular responses to ultrasound stimulation, especially due to the presence of mechanosensitive Piezo-1 ion channels in both cell types. A Fluo-4 calcium imaging kit (Thermo Fisher) was used to visualize cell activity. The Fluo-4 dye perme-

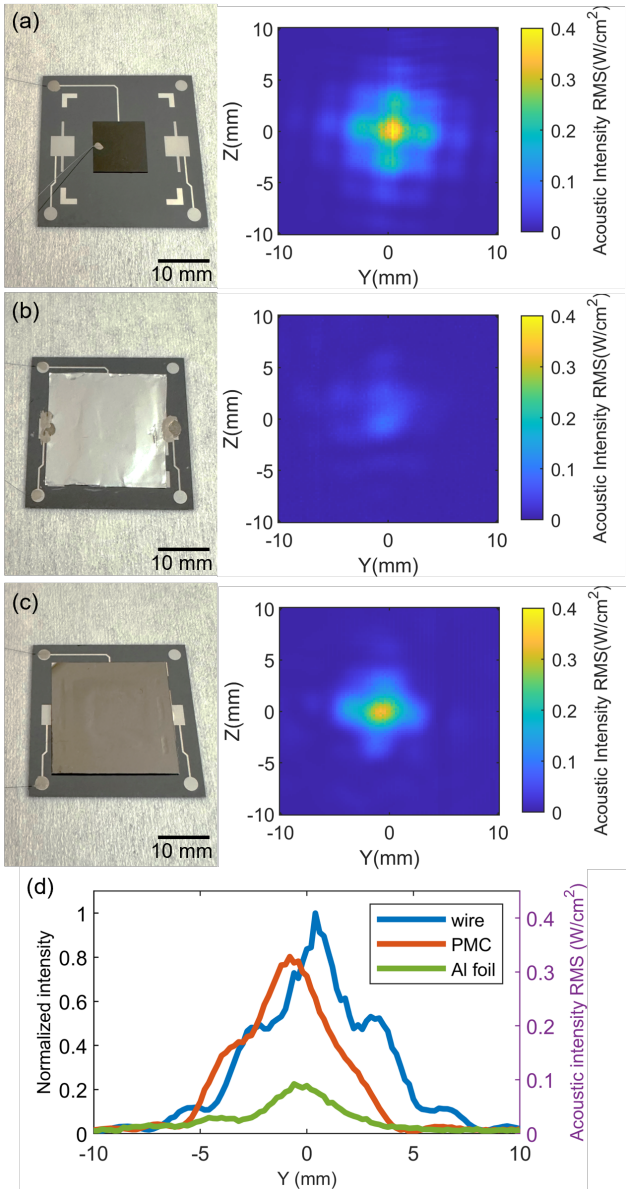

Figure 4.12: Comparison of transducer performance with different top connection methods: (a) reference transducer with wire connection, (b) transducer with 15 µm thick aluminum foil connection, and (c) transducer with polymer-metal connection (PMC). The cross-sectional beam profiles at the focal spot are shown for each transducer. (d) Comparison of the intensity profiles, demonstrating the superior performance of the PMC compared to the aluminum foil connection.

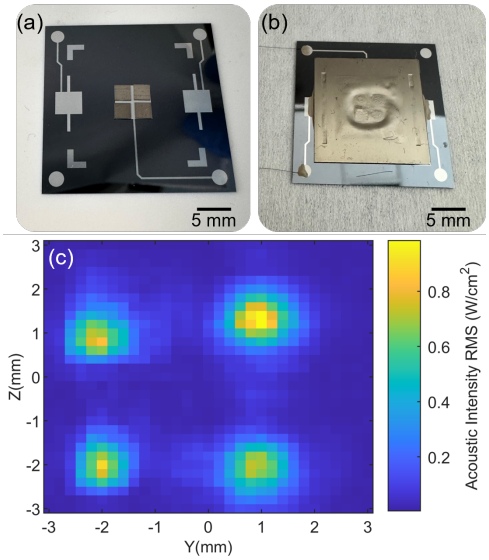

Figure 4.13: Implementation of a polymer-metal connection (PMC) on a 2x2 transducer array: (a) transducer array before PMC application, (b) transducer array after PMC application, and (c) intensity profile at a 12 mm distance, showing four distinct focal spots corresponding to the individual elements.

ates into the cells. During an influx of Ca^{2+} ions, such as during action potentials, the dye exhibits increased fluorescence by binding with Ca^{2+} ions, which is recorded by the microscope. The ultrasound transducer was mounted on a 3D-printed adapter to interface the device with a commercial 12-well plate platform. A custom user interface set the transducer stimulation parameters based on hydrophone calibration measurements. The experiments were based on the literature which consisted of the following steps: 3 minutes of baseline cell activity recording, 3 minutes of cell stimulation, and 3 minutes of post-stimulation recording [12]. The stimulation parameters were 200 kPa peak-to-peak pressure, 9 MHz center frequency, 1 ms pulse repetition duration, and 0.2% duty cycle. Preliminary results showed that both hiPSC-derived neurons and HUVECs responded to the ultrasound stimulus. Increased spiking activity, indicated by brief increases in fluorescence, was observed and correlated with the ultrasound stimulus. For neurons, spiking activity was accompanied by an increase in baseline fluorescence intensity as seen in Figure 4.14. A similar increase, though less pronounced, was observed in the HUVECs response (Figure 4.15). This change in fluorescence contrasts with the typical decrease in intensity due to photobleaching and warrants further investigation. While the study's biological impact remains to be fully elucidated, the observed cellular responses encourage further investigation using this setup.

4.6. CONLUSION

This chapter presented a novel approach for implementing a top metal connection in an ultrasound transducer to optimize transmit efficiency. The proposed concept utilizes

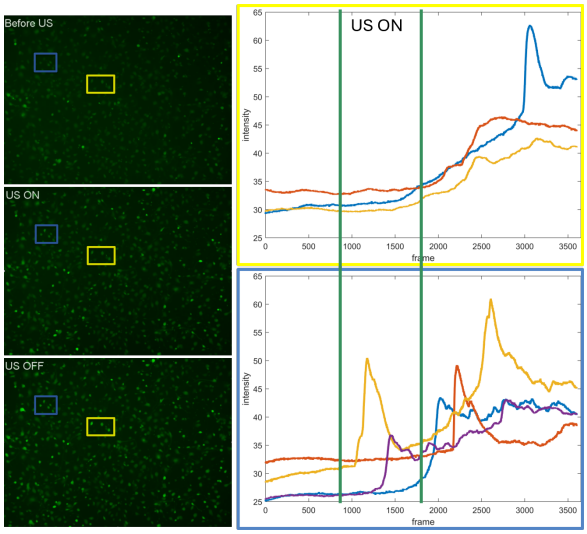

Figure 4.14: (left)The fluorescence imaging of the hIPSC-derived neurons before, during and after the ultrasound stimulation.(right) The fluorescence intensity of neurons over time within the blue and yellow areas, respectively.

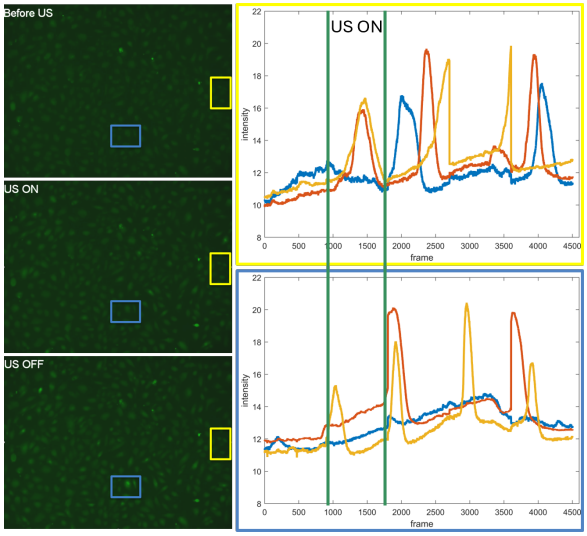

Figure 4.15: (left)The fluorescence imaging of the HUVECs before, during and after the ultrasound stimulation.(right) The fluorescence intensity of HUVECs over time within the blue and yellow areas, respectively.

microfabrication technology to create a polymer-metal membrane supported by a silicon frame. The membrane consists of a PDMS/Ti/Al stack with a total metal thickness of 450 nm. The concept was designed and simulated in COMSOL Multiphysics to analyze the effect of PDMS and metal thicknesses on transducer output intensity. Experimental

validation showed that the PMC preserved 80% of the output intensity compared to an ideal reference. This represents an improvement over the state-of-the-art using a 15 μm-thick aluminum film, which achieves only 22.5% of the ideal output intensity. The PMC was validated on a 2x2 transducer array, demonstrating its ability to connect all elements within the array. Preliminary biological validation using the PMC transducers was performed with calcium fluorescence microscopy on hiPSC-derived neurons and HUVECs. Both cell types responded to the ultrasound generated by the fabricated transducer, encouraging further study using this setup.

The use of PMC shows promising results and potential. Using microfabrication technology, the metal layer on the PMC can be patterned, enabling addressable top connections, which can be useful for implementing row-column array ultrasound. Future work will focus on further optimization and implementation of the PMC on a phased array transducer integrated on ICs. This research has the potential to significantly improve the performance and reducing the power consumption of ultrasound transducers.

BIBLIOGRAPHY

[1] G. K. Wardhana, T. L. Costa, and M. Mastrangeli, "An acoustically transparent electrical cap for piezoelectric ultrasound transducers on silicon", in *Proceedings of XXXV EUROSENSORS Conference*, 2023. DOI: 10.3390/proceedings2024097050.

[2] C. Chen, Z. Chen, D. Bera, *et al.*, "A front-end asic with receive sub-array beamforming integrated with a 32 × 32 pzt matrix transducer for 3-d transesophageal echocardiography", *IEEE JOURNAL OF SOLID-STATE CIRCUITS*, vol. 52, 4 2017. DOI: 10.1109/JSSC.2016.2638433. [Online]. Available: http://ieeexplore.ieee.org..

[3] D. M. Van Willigen, E. Kang, J. Janjic, *et al.*, "A transceiver asic for a single-cable 64-element intra-vascular ultrasound probe", *IEEE Journal of Solid-State Circuits*, vol. 56, pp. 3157–3166, 10 Oct. 2021, ISSN: 1558173X. DOI: 10.1109/JSSC.2021.3083217.

[4] T. Costa, C. Shi, K. Tien, J. Elloian, F. A. Cardoso, and K. L. Shepard, "An integrated 2d ultrasound phased array transmitter in cmos with pixel pitch-matched beamforming; an integrated 2d ultrasound phased array transmitter in cmos with pixel pitch-matched beamforming", *IEEE Transactions on Biomedical Circuits and Systems*, vol. 15, 4 2021. DOI: 10.1109/TBCAS.2021.3096722. [Online]. Available: https://www.ieee.org/publications/rights/index.html.

[5] C. Shi, X. Luo, J. Guo, Z. Najdovski, T. Fukuda, and H. Ren, "Three-dimensional intravascular reconstruction techniques based on intravascular ultrasound: A technical review", *IEEE Journal of Biomedical and Health Informatics*, vol. 22, pp. 806–817, 3 May 2018, ISSN: 21682208. DOI: 10.1109/JBHI.2017.2703903.

[6] Y. M. Hopf, B. W. Ossenkoppele, M. Soozande, *et al.*, "A pitch-matched transceiver asic with shared hybrid beamforming adc for high-frame-rate 3-d intracardiac echocardiography", *IEEE Journal of Solid-State Circuits*, vol. 57, pp. 3228–3242, 11 Nov. 2022, ISSN: 1558173X. DOI: 10.1109/JSSC.2022.3201758.

[7] V. Pashaei, P. Dehghanzadeh, G. Enwia, M. Bayat, S. J. Majerus, and S. Mandal, "Flexible body-conformal ultrasound patches for image-guided neuromodulation", *IEEE transactions on biomedical circuits and systems*, vol. 14, pp. 305–318, 2 Apr. 2020, ISSN: 1940-9990. DOI: 10.1109/TBCAS.2019.2959439. [Online]. Available: https://pubmed.ncbi.nlm.nih.gov/31831437/.

[8] A. I. Velea, S. Vollebregt, G. K. Wardhana, and V. Giagka, "Wafer-scale graphene-based soft electrode array with optogenetic compatibility", in *2020 IEEE 33rd International Conference on Micro Electro Mechanical Systems (MEMS)*, 2020, pp. 421–424. DOI: 10.1109/MEMS46641.2020.9056367.

[9] H. Aydogmus, M. Hu, L. Ivancevic, *et al.*, "An organ-on-chip device with integrated charge sensors and recording microelectrodes", *Scientific Reports*, vol. 13, 1 Dec. 2023, ISSN: 20452322. DOI: 10.1038/s41598-023-34786-5.

[10] Y. Hosono, Y. Yamashita, and K. Itsumi, "Effects of fine metal oxide particle dopant on the acoustic properties of silicone rubber lens for medical array probe", *IEEE Transactions on Ultrasonics, Ferroelectrics, and Frequency Control*, vol. 54, pp. 1589–1595, 8 Aug. 2007, ISSN: 08853010. DOI: 10.1109/TUFFC.2007.429.

[11] K. Ono, "A comprehensive report on ultrasonic attenuation of engineering materials, including metals, ceramics, polymers, fiber-reinforced composites, wood, and rocks", *Applied Sciences (Switzerland)*, vol. 10, 7 Apr. 2020, ISSN: 20763417. DOI: 10.3390/app10072230.

[12] H. B. Kim, K. M. Swanberg, H. S. Han, *et al.*, "Prolonged stimulation with low-intensity ultrasound induces delayed increases in spontaneous hippocampal culture spiking activity", *Journal of Neuroscience Research*, vol. 95, 3 2017, ISSN: 10974547. DOI: 10.1002/jnr.23845.

5

FRESNEL PHASING ZONE PLATE

This chapter presents a Fresnel Phasing Zone Plate (FPZP) made of Polydimethylsiloxane that was fabricated using a single photolithography step. The FPZP builds upon the PMC structure demonstrated in the previous chapter. The FPZP offers a simpler alternative to focus ultrasound waves compared to phased arrays and better efficiency and scalability compared to conventional convex/concave lenses. The fabricated FPZP demonstrated a focal gain of 19.95 dB at a 15 mm focal distance and a lateral resolution of 0.25 mm at 9.1 MHz.

In the realm of biomedical ultrasound, focused ultrasound (FUS) offers a significant enhancement in spatial resolution and energy efficiency compared to conventional unfocused transducers [1],[2]. The ability to concentrate acoustic energy at a designated target area has spurred extensive research into its diverse applications, encompassing high-resolution ultrasound imaging [3],[4], wireless power transfer of implanted medical devices [5], targeted tissue ablation in deep brain regions [6], and neuromodulation to treat neurological diseases [7],[8]. Within the specific domain of neuromodulation, the spatial resolution of the ultrasound transducer directly impacts the precision of the neurostimulation [9]; the enhanced resolution achieved through FUS translates to more targeted modulation, potentially reducing unintended side effects associated with off-target stimulation [9],[10].

5.1. CONCEPT OF FOCUSED ULTRASOUND

Leveraging the shared nature of waves, acoustic focusing exhibits parallels with techniques employed in light [1],[11] and electromagnetic wave manipulation [12],[13]. All three share the fundamental properties of wave propagation, allowing for the application of similar principles for focusing. In essence, the core concept involves manipulating wave propagation within a medium to achieve constructive interference at a designated point of interest. Focusing techniques can be broadly categorized into two primary approaches in achieving constructive interference at a specific location: spatial manipulation using lenses to physically alter the outgoing wave path and temporal manipulation by strategically controlling the phase difference of multiple wave sources. However, the implementation of temporal manipulation requires complex and precise individual control over elements within an array of acoustic sources. These control signals are typically generated by multiple bulky circuit boards or are expensive to develop by using complementary metal-oxide semiconductor (CMOS) chips [14],[15], which are not explored in this chapter.

5.1.1. CONVENTIONAL LENS

Similar to light, acoustic focusing can be obtained through convex (Figure 5.1(a))[16] and concave lenses (Figure 5.1(b))[3]. The use of either lens depends on the ratio of the speed of sound between the lens (c_{lens}) and propagation medium (c_{medium}), which is called refractive index (n), as given by Eq. 5.1. At $n < 1$, a concave lens is used to focus the outgoing wave, while at n >1, a convex lens is used.

$$n = \frac{c_{medium}}{c_{lens}} \tag{5.1}$$

The focal distance (FD) of convex and concave lenses are determined by their radius (R_{lens})[17]:

$$FD_{convex} = \frac{R_{lens}}{(n-1)}; \qquad c_{lens} < c_{medium} \tag{5.2}$$

$$FD_{concave} = \frac{R_{lens}}{(1-n)}; \qquad c_{lens} > c_{medium} \tag{5.3}$$

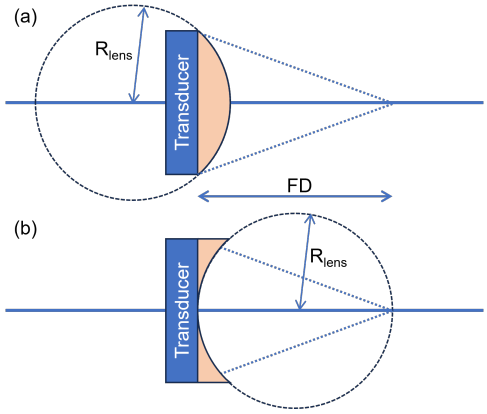

Figure 5.1: (a) The geometry of a plano-convex lens. (b) The geometry a plano-concave lens.

Therefore, as the focal distance of an acoustic lens increases, the required lens size also grows. This larger size can negatively impact acoustic transmission efficiency due to propagation loss along the lens. Transmission efficiency is also affected by the acoustic impedance, a characteristic parameter of a material, which influences the reflection at the lens interfaces as dictated by Fresnel's equation (Eq.2.3). Polymers are generally the preferred material group mainly due to their acoustic impedance similarity with water and soft tissue [3],[16],[18]. Commonly used polymers include silicon rubber[18], typically used for convex lenses, and epoxy[3], which is better suited for concave lenses.

Table 5.1: Acoustic properties of lens materials.

Material	Velocity (m/s)	Density (kg/m^3)	Impedance (MRayls)
Water	1480	1000	1.48
Epoxy[3]	2640	1080	2.85
Silicone rubber[3]	950	1580	1.5

When assuming water as the propagation medium, the refractive index of epoxy and silicone rubber are 0.56 and 1.56, respectively. Therefore, the radius of the lens with both materials is approximately half of the intended focal distance, which leads to bulky lens geometry. The focusing ability of an acoustic lens is also subject to Abbe's diffraction limit, which theoretically limits the smallest spatial resolution a lens can achieve [1].

5.1.2. FRESNEL LENS

The concept of the Fresnel lens was invented to reduce the size and weight of a lens while retaining its functionality. The concept was first applied in optics to create large lenses needed in lighthouses [19]. A lens focuses waves through refraction that occurs on the interface of the medium and the lens. Therefore, the bulk of the lens does not contribute to its focusing properties and causes unnecessary attenuation. A Fresnel lens utilizes this concept by strategically removing non-essential material in focusing (Figure 5.2), resulting in a lens with a thinner form and concentric pattern.

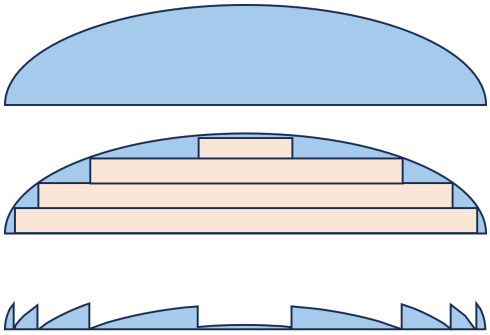

Figure 5.2: Schematic showing the concept of a Fresnel lens: (top) a convex lens, (middle) a convex lens with sections of the lens that don't contribute to the focusing highlighted, (bottom) the geometry of the lens after the highlighted parts are removed, thus making a Fresnel lens.

The Fresnel lens offers several advantages compared to conventional lenses: (1) less material utilized, (2) lighter in weight, (3) higher transmission efficiency. However, Fresnel lenses are susceptible to aberrations due to diffraction that occurs on the edges of the irregularly shaped concentric patterns, making the adoption of Fresnel lenses less popular for imaging applications [20]. Additionally, due to the irregular shape of the lens surface, the practicality of its fabrication is the main barrier to the adoption of the Fresnel lens, especially in a small form factor. One way to realize this complex structure is by utilizing grayscale lithography, which is difficult to optimize due to the complexity of the exposure and development steps [21].

5.1.3. FRESNEL ZONE PLATE

Fresnel zone plates (FZPs) emerged as a solution to the fabrication complexities associated with traditional Fresnel lenses [22]. Unlike previous lenses that rely on the refraction of waves, FZPs utilize the principle of diffraction, where waves spread and bend around obstacles[1]. An FZP consists of alternating 'opaque' and 'transparent' concentric rings, which block and pass waves going through the lens. By carefully controlling the size of each ring, the diffraction of waves through FZP can be manipulated to create constructive interference at a predetermined focal point. The equation in Eq.5.4 describes the n^{th} radius of transition between 'opaque' and 'transparent' zones [23]:

$$r_n = \sqrt{\left(\frac{n\lambda}{2}\right)^2 + n\lambda F_D} \tag{5.4}$$

, where λ is the wavelength in the propagation medium and F_D denotes the desired focal distance of the lens. Figure 5.3(b) shows the cross-section of an FZP. The binary stepped structures of an FZP are much easier to fabricate than a Fresnel lens due to the rectangular shape of each individual ring as opposed to the irregular triangular shape. The use of FZP has been shown by using air as the 'opaque' zone to block the propagation of waves completely [24],[25]. In this work, a Polydimethylsiloxane (PDMS) structure was used to trap air pockets in front of a transducer. However, a reduction of transmission efficiency in a diffracting system is unavoidable because some of the incoming waves will be re-

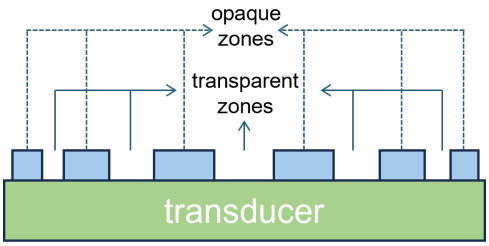

Figure 5.3: Schematic showing the cross-section of an FZP.

flected by the 'opaque' zones. To avoid the loss due to the acoustically blocking zones, other works attempted proposed the direct imprinting of the zone plate pattern on the piezoelectric material through plasma etching [11],[26]. The etching process was done in several steps to make zone plates with multiple levels, thus approximating the shape of a Fresnel lens. However, alterations to the piezoelectric material can lead to changes in the resonance mode that might negatively impact the vibration mode of the transducer. There is also a lack of definitive efficacy in focusing on using this method in the literature. Another way to implement the FZP concept is by patterning the shape of the electrode driving the transducer, therefore selectively driving parts of the transducer to simulate the different zones in FZP [27]. This approach enables programmable focusing, but it still suffers from low efficiency due to parts of the transducer not contributing to the generation of the focal point.

5.1.4. FRESNEL PHASING ZONE PLATE

Fresnel phasing zone plates (FPZPs) offer a more efficient approach compared to traditional FZPs [28]. Unlike FZPs, which utilize opaque zones to block a portion of the sound waves, FPZPs employ translucent zones with a different speed of sound, similar to materials used in conventional convex/concave lenses. These translucent zones introduce a phase shift on the wavefront as the sound travels through the lens relative to the wavefront passing through the transparent zones. Similar to FZPs, diffraction still occurs on the edges of the translucent zones, and the focal distance of the lens can still be determined using the FZP formula. However, unlike in FZP, the thickness of the translucent zones plays a crucial role as it affects the phase difference relative to the transparent zones. Ideally, a complete constructive interference is desired to maximize the energy in the focal area, which can be achieved by imposing a π phase difference between the transparent and the translucent zone. In theory, a π phase difference is achieved when the thickness of the translucent zone satisfies the following [11]:

$$h = \frac{1}{Nf\left(\frac{1}{c_m} - \frac{1}{c_l}\right)} \tag{5.5}$$

,where f, N, c_m, and c_l are the frequency of the ultrasound wave, the number of height levels within the FPZP, the speed of sound in the medium and in the lens, respectively. Several FPZPs have been implemented to focus ultrasound waves at 1 MHz [28],[29],

which utilize a 3D-printed lens made of polylactic acid (PLA) placed a distance from the transducer. These works showed that FPZP improved the output intensity by a factor of 2 when compared to FZP. However, the implementation for higher frequency applications is limited by the resolution of 3D printing techniques and tolerable printing artifacts, such as shrinkage and surface roughness. The use of 3D-printed PLA to create sub-millimeter structures is also prone to warping due to thermal stress that can affect the focusing accuracy of the lens.

5.1.5. ACOUSTIC METAMATERIALS

The focusing strategies presented so far are implemented by geometrically shaping a lens made of conventional materials. The spatial resolution that can be achieved by these techniques is theoretically limited to Abbe's diffraction limit (ADL)[1].

$$ADL = \frac{\lambda}{2NA} \tag{5.6}$$

$$NA = sin(\theta) \approx \frac{r}{F_d} \tag{5.7}$$

, Where NA is the numerical aperture. Artificial materials can be made to have properties that have atypical behavior of wave propagation, which are typically addressed as acoustic metamaterials (AMMs). As an example, these materials can have a negative refractive index, which can generate evanescent waves close to the lens [30],[31]. The presence of evanescent waves allows for a focusing that is able to exceed the diffraction limit. An engineered material can also have a gradient refractive index in a thin-film form factor and, therefore, can naturally focus acoustic waves traveling through it [32]. However, most studies on AMM are still in a proof-of-concept stage conducted at low frequencies at a few kHz [30],[33]. Although some experimental results have been shown, it still requires a large supporting structure to manipulate the lens [34], thus making miniaturization on the system level challenging.

5.1.6. HIGH TRANSMIT EFFICIENCY ACOUSTIC LENS

To summarize, there are several approaches to focusing ultrasound waves using lenses. A convex/concave lens is the most conventional approach, however, it is bulky in terms of size. Therefore, it is susceptible to propagation loss which can reduce its efficiency. Fresnel lens mitigates this propagation loss by removing volume that is not essential in the focusing, thus making the lens more efficient. However, Fresnel lens is not practical to make due to its complex structure. FZP is an approximation of a fresnel lens, which typically consists of alternating concentric rings that pass and block incoming waves. Due to the partial blocking of the incoming waves, the efficiency of the FZP is lower than that of a Fresnel lens. FPZP addresses the drawback of FZP by replacing the blocking zones with phase-shift zones that alter the phase of the wave as it travels through the lens and, therefore, improve the efficiency of the lens. Based on the literature, the FPZP is the most promising approach to implementing a high transmit efficiency acoustic lens. However, there is a lack of quantitative comparative study of the different acoustic lens approaches in terms of their efficiency. Therefore, the next section discusses the use of finite element modeling (FEM) to compare the performance of different acoustic lenses.

5.2. FINITE ELEMENT MODELLING

Finite element modeling in COMSOL Multiphysics was used to simulate the acoustic interaction of materials and structures in a 2D field. The goal of this FEM is to see how the FPZP compares with FZP and conventional convex lenses and also to understand the effect of each design parameter within FPZP and its effect on the eventual fabrication variation. A MATLAB script was used to aid the calculation of a Fresnel structure and the generation of the lens structures within the COMSOL environment.

5.2.1. SIMULATION SETUP

FRESNEL STRUCTURE FORMULA

The lens geometry of a Fresnel structure can be calculated by following the procedure described in [23]. The inputs of these calculations are the focal distance F_D, the frequency of ultrasound f, and the angle of focusing α. Firstly, some intermediary equations have to be solved.

$$k = \frac{2\pi}{\lambda} \tag{5.8}$$

$$X_c = F_D * \tan(\alpha) \tag{5.9}$$

$$Y_{max} = k * X_c * \sin(\alpha) - k\sqrt{{X_c}^2 + {F_D}^2} - F_D \tag{5.10}$$

$$C_n = F_D - \frac{Y_{max} - n\pi}{k} \tag{5.11}$$

, where k is the wavenumber, Y_{max} is the phase that has to be generated by the lens to achieve the desired focusing angle.

$$X_n = \frac{C_n * \sin(\alpha)}{\cos^2(\alpha)} \tag{5.12}$$

$$M_n = \frac{\sqrt{{C_n}^2 - {F_D}^2 + {X_n}^2 \cos^2(\alpha)}}{\cos(\alpha)} \tag{5.13}$$

$$r_{right,n} = X_n + M_n \tag{5.14}$$

$$r_{left,n} = X_n - M_n \tag{5.15}$$

, where X_n is the center point of the n^{th} transition and M_n is the distance of the transition from the center point. When constructing the rings around a center axis perpendicular to the rings, the variables r_{right} and r_{left} denote the position of the n^{th} transition to the left and the right relative to the center axis. Without any focusing angle, X_n will be zero, and the rings in the zone plate will be axisymmetric. The steering angle will make the rings form an oval shape with an off-center central point. Which causes the rings to be denser on one side and sparser on the other side. For a given lens configuration to be simulated, the radii and their central points are calculated and processed in Matlab, such that they can be imported as coordinates into COMSOL to build a 2D geometry for the simulation.

COMSOL SIMULATION

The FEM in COMSOL Multiphysics was performed using a 2D simulation model in the frequency domain. Three modules were used: Pressure acoustics, solid mechanics, and electrostatics. The solid mechanics and electrostatics module were used to simulate the piezoelectric effect. The piezoelectric effect will generate mechanical deformation in the presence of an electric field. The deformation of a piezoelectric material causes displacement of domain boundaries, which is used as a pressure source in the pressure acoustic module. The pressure acoustics module solves the propagation of acoustic waves through materials within its domain. The propagation can be modeled as a linear elastic or attenuating fluid model. A perfectly matched layer (PML) was implemented as the boundary condition on the edges of the pressure acoustic domain to avoid reflection due to the finite simulation space, which affects the accuracy of the simulation. The simulation consists of two structures: a piezoelectric layer, made of lead zirconate titanate (PZT), and a lens structure. The lens structure can be a conventional convex/concave lens, FZP or FPZP. The mesh shape is chosen to be quadrilateral due to the greater stability of the simulation results. There is a trade-off between accuracy and computational speed when deciding on the maximum mesh size. The maximum size of the mesh was kept constant during the simulation as a factor of wavelength within the medium, with ten data points within a single wavelength. The summary of the key parameters and the material properties used during the simulation can be found in Table 5.2 and Table 5.3.

In the context of *in vitro* ultrasound neuromodulation, the transducers were intended to stimulate cell cultures on a substrate such as well plates or microelectrode arrays (MEAs). Ideally, the focused acoustic energy generated by the transducer should be formed on the surface of the substrate at which the cells are positioned. In the case of a well plate, the focal distance is dictated by the well's height, which ranges between 16-17 mm. In practice, the focus will generate a volumetric region with high acoustic pressure that covers a certain depth and lateral area as opposed to a point. The theoretical focal point can then be positioned slightly above the well substrate. This allows the focal depth to encompass the remaining distance and compensate for the variation of the well height. The focal spot was positioned at 15 mm during this simulation to allow compatibility with available well plates. A PZT with a center frequency of 8.5 MHz was chosen based on the material's availability and prior experience with this frequency. However, the model and concept presented here were not limited to this frequency. Acoustic intensity and acoustic pressure were the metrics used to characterize the output of the transducers and lenses.

Table 5.3: Material properties used in the acoustic lens simulation.

Material	Density (kg/m^3)	Speed of sound (m/s)	Acoustic impedance ($MRayl$)	Attenuation coefficient ($dB/cm/MHz$)
Water [35]	1000	1480	1.48	0.0022
PDMS [36]	1077	970	1.04	4.3[16]
PZT-5H*	7500	4600	34.50	-
Air [35]	1.225	343	0.000042	7.5

*Taken from COMSOL material library

Table 5.2: key parameters for the acoustic lens simulations.

Parameter	Value
Frequency	8.5 MHz
Maximum mesh size	$\lambda_{medium}/10$
Mesh shape	Quadrilateral
PZT width	10 mm
PZT thickness	0.27 mm
Simulation space	20 mm x 30 mm
Intended F_D	15 mm

5.2.2. SIMULATION OF CONVENTIONAL LENS

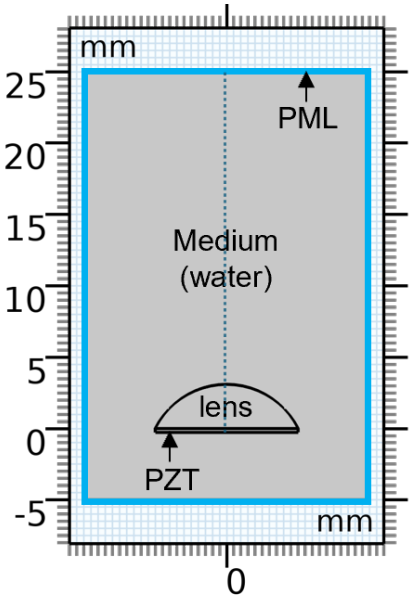

Figure 5.4: The geometrical structure of the conventional convex lens simulation in COMSOL.

A conventional convex lens made of silicone rubber was constructed with an intended focal distance of 15 mm. Silicone rubber is widely used as a lens material in commercial ultrasound transducers. In order to have a fair comparison with microfabricated FZPs and FPZPs, polydimethylsiloxane (PDMS) was chosen as the lens material. PDMS is a type of silicone rubber compatible with the microfabrication process and widely used in biomedical devices [37]. Since sound waves travel slower in PDMS relative to the surrounding propagation medium, waves can be focused with a convex lens. Following Eq.5.2, a lens with a radius of 5.6 mm is required to achieve a 15 mm focal distance. The simulation geometry for the convex lens can be seen in Figure 5.4. Three simulations were performed: an unfocused simulation without any lens, a focused simulation using

a convex lens, assuming elastic propagation, and a focused simulation with attenuation in the model. The material properties used during the simulation can be found in Table 5.3. Using these simulations, the focusing gain can be observed by comparing the intensity at 15 mm between focused and unfocused simulations. To analyze the focusing effects, a 1D plot was extracted from the intensity profile along the perpendicular line drawn from the center of the transducer as shown as a dotted line in Figure 5.4. The unfocused simulation can be seen in Figure 5.5(a), and the intensity normal to the center of the transducer can be seen in Figure 5.6(a). Figure 5.5(b) shows the intensity profile of the convex lens when the propagation was assumed to be linear elastic. A focusing gain of 18.7 dB was achieved with this model when compared to the unfocused simulation. Attenuation was then added to the lens and the medium with attenuation coefficients of 3655 dB/m [16] and 1.87 dB/m [35], respectively. The addition of attenuation in the model affected the intensity amplitude of the transducer.

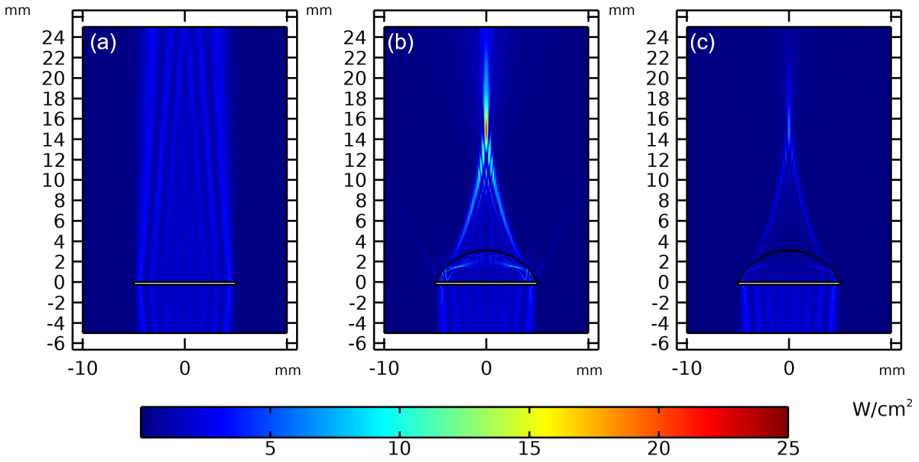

Figure 5.5: 2D intensity profile: (a) unfocused ultrasound transducer as a reference, (b) Convex PDMS lens assuming elastic propagation, and (c) convex PDMS lens assuming propagation attenuation.

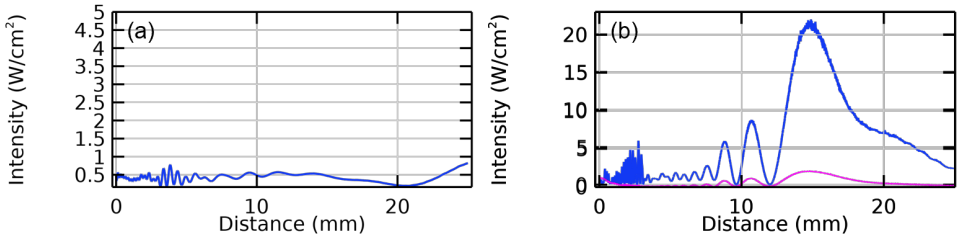

Figure 5.6: 1D intensity profile: (a) unfocused ultrasound transducer, (b) convex PDMS lens without attenuation (blue) and with attenuation (magenta).

However, the beam profile of the lens was preserved, as shown in Figure 5.5(c). The

output intensity of the lens was reduced by 90% due to the attenuation as shown in Figure 5.6(b), which reduced the focusing gain to 8.51 dB. These results showed that the performance of a convex lens is heavily influenced by its thickness and material choice.

5.2.3. SIMULATION OF FZP

An implementation of FZP, as presented by Tang et al. utilized air as the opaque zones [24],[25]. Air presents itself as an effective blocking layer due to its significant acoustic impedance mismatch with water and PZT. This mismatch results in a near-zero acoustic transmission factor, effectively blocking the acoustic wave. The lens was designed with a focal distance of 15 mm and the dimensions of the lens were constructed according to Eq.5.14 and Eq.5.15. The geometry of the model used in the simulation can be seen in Figure 5.7. Two geometries were simulated, the first being an ideal scenario with air as the opaque zones and the second being a practical scenario with air being trapped in place by using PDMS structures as presented in the literature.

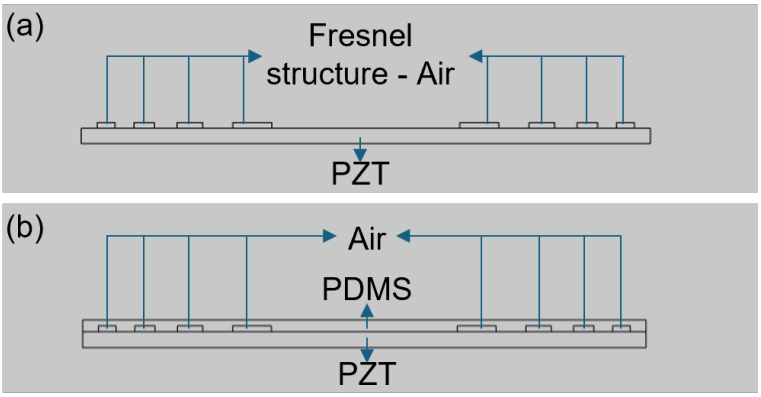

Figure 5.7: The geometrical structure of FZP simulation, (a) ideal air FZP, and (b) practical implementation of air FZP with PDMS trap.

Figure 5.8 shows the comparison between the ideal air FZP with and without attenuation. Although the air has a much higher attenuation coefficient (Table 5.3) compared to PDMS and water, the effect of attenuation of the ideal air FZP lens was negligible, as indicated by the mostly overlapping plot in Figure 5.8(a). Therefore, the attenuation of the waves was dominated by the water, which is relatively small at a short distance. When taking into account a more practical implementation of this technique by having a structure that can hold the air in place (Figure 5.7(b)). Since the attenuation is directly related to the thickness of the PDMS layer, a thickness of 250 μm on the transparent zones was used, as presented in the literature [25]. The peak intensity generated by the practical implementation was lower than the ideal, even when assuming elastic propagation due to the reflection introduced by the additional PDMS interfaces. The effect of attenuation due to the additional PDMS layer was apparent, as shown in Figure 5.8(b), which reduced the focusing gain from 14 dB to 13.1 dB. From a closer look into the intensity and pressure beam profile shown in Figure 5.9, the air-opaque zones were mostly

blocking the transmission of waves through the opaque zone.

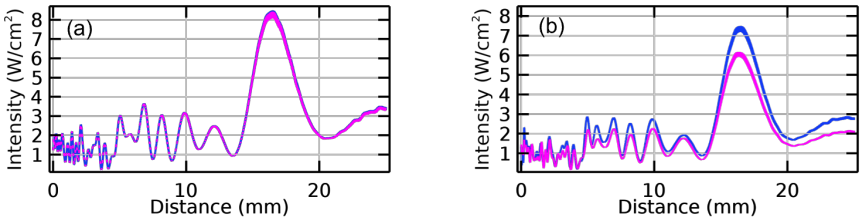

Figure 5.8: 1D intensity profile of ideal FZP without attenuation (blue) and with attenuation (magenta):(a) ideal implementation, (b) practical implementation with PDMS structure as shown in [24].

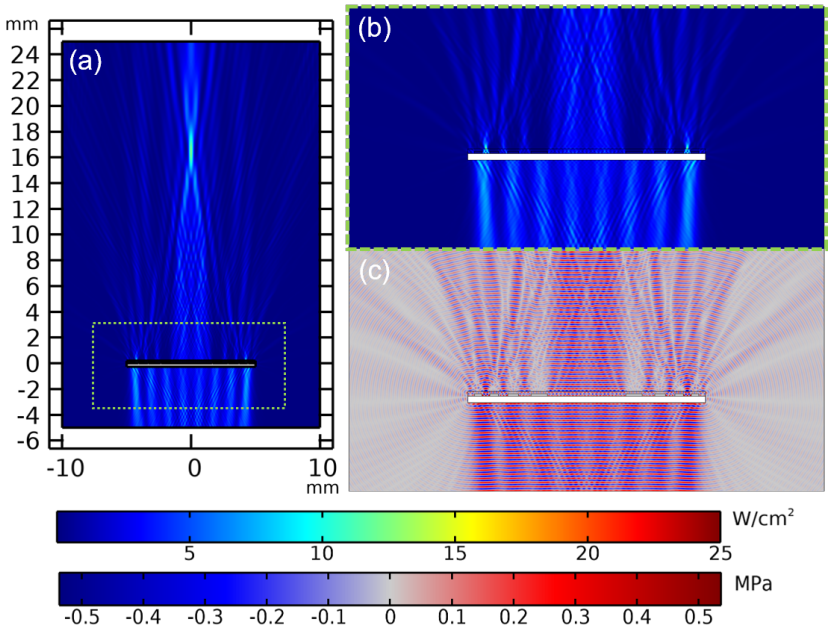

Figure 5.9: 2D profile of practical FZP with PDMS trap: (a) entire intensity profile and (b) close-up of the intensity profile. (c) close-up of the pressure profile.

5.2.4. SIMULATION OF FPZP

A simulation of FPZP was conducted following the geometrical setup as presented in Figure 5.10. For practicality during the implementation, a handle layer was included in the FPZP simulations. A layer of PDMS was incorporated between the PZT and the Fresnel structure to facilitate the handling of the lens. The handle layer and the Fresnel structure were planned to be made in the same process, which simplifies the fabrication process and also reduces reflection due to the material interface.

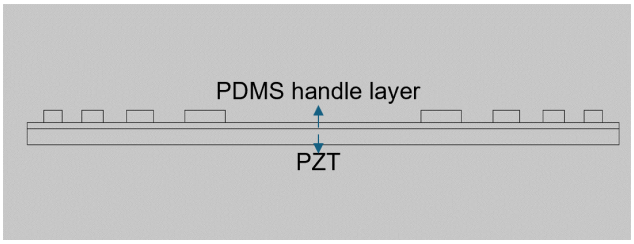

Figure 5.10: The geometrical structure of FPZP simulation.

In order to find the optimum thickness that maximizes the constructive interference, the thickness of the fresnel structure was swept from 50 μm to 350 μm. This range of thickness was chosen based on the calculation of Eq. 5.5. When assuming the number of height levels to be binary, a frequency of 8.5 MHz, the speed of sound in the medium to be 1480 m/s and the speed of sound in the PDMS to be 1077 m/s, the optimum thickness was calculated to be 0.23 mm thick. Figure 5.11 shows the result of the sweep, which is in agreement with the result of the calculation. It is also important to note that the effect of the structure thickness exhibited a broad tolerance, with comparable performance seen between 100 μm and 250 μm thickness. A closer look at the 2D pressure profile showed the effect of phase difference influenced by the FPZP. A π phase difference, signified by complete destructive interference can be observed in the near field. The phase difference in the near field will compensate for the difference in distance of different zones across the FPZP. As the waves travel closer to the focal spot, the phase of the waves can be observed to be more aligned, thus maximizing the constructive interference. The effect of attenuation was also observed on the FPZP. Unlike the FZP, attenuation will occur in the translucent zone due to the passing of the waves. The attenuation introduced by the 100 μm thick handle layer was also taken into consideration.

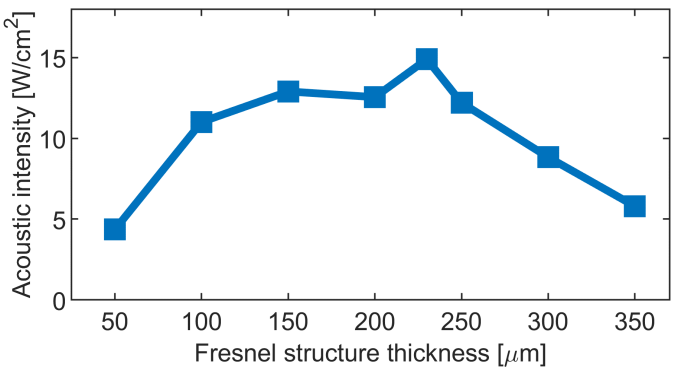

Figure 5.11: Effect of Fresnel structure thickness to the maximum output intensity.

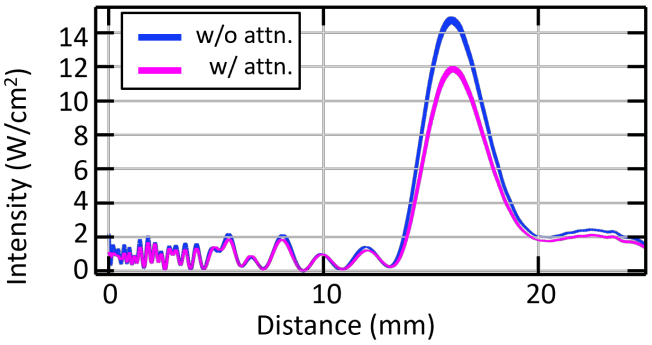

Figure 5.12: Comparison of the 1D intensity profile of FPZP perpendicular to the center of the transducer without attenuation (blue) and with attenuation (magenta).

5

Table 5.4: Comparison of focusing gain of different lenses.

	Convex lens	FZP	FPZP
Gain-elastic (dB)	18.7	14	16.98
Gain-attenuation (dB)	8.51	13.1	16.04

Figure 5.12 shows the influence of attenuation in FPZP. As expected, the influence of material attenuation in FPZP is much larger than in FZP due to the wave traveling through the translucent zones. A reduction of 19.5% in intensity was observed, which was better than the case of convex lens. Although FPZP was more influenced by attenuation compared to FZP, the overall focusing gain was much larger. The comparison of gain of each type of lens can be seen in Table 5.4. The improvement of focal gain around $3dB$ aligned with the result presented in [28].

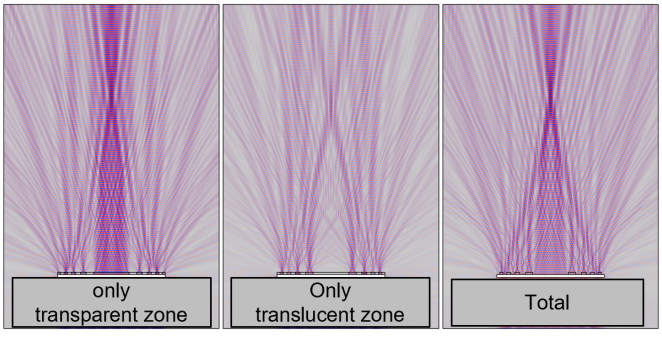

Figure 5.13: The superposition principle on the peak-to-peak pressure from the transparent and translucent zone of FPZP at optimum Fresnel structure thickness.

Table 5.5: Pressure contribution of transparent and translucent zones.

Structure thickness	Transparent zones - pressure	Translucent zones - pressure	Total - pressure
0.23 mm	1.02 MPa	0.54 MPa	1.56 MPa
0.10 mm	0.99 MPa	0.49 MPa	1.13 MPa

SUPERPOSITION OF PRESSURE IN FPZP

The overall improvement of the focusing efficiency of FPZP compared to FZP can be explained by the contribution of the translucent zones in the FPZP. The efficiency of the phase alignment can be seen by observing the contribution of the translucent zones and transparent zones in the pressure domain. When the Fresnel structure was on the optimal value (0.23 mm), the total pressure on the focal spot was the superposition of the pressure on the focal spot by the transparent and translucent zones, signifying a good alignment of phase on the focal spot. However, when the Fresnel structure was not optimum (0.1 mm), the total pressure didn't follow the superposition characteristic due to incomplete constructive interference due to the phase difference.

DESIGN PARAMETERS OF FPZP

Several design parameters were also tested using the simulation model, including the aperture of the transducer, focal distance, and frequency mismatch. Table 5.6 shows the effect of aperture on the performance of FPZP. The FPZP structure can be seen in Figure 5.14, with the FPZP structure covering the extent of the full aperture in each configuration. The FPZP was designed to have a focal distance of 15 mm. The comparison between the three configurations can be seen in Figure 5.15 and Table 5.6. The aperture size improved the output intensity and spatial resolution of the FPZP. However, when observing the focal gain of each aperture, the performance of FPZP was worse at smaller aperture. The focal gain was calculated as the ratio of intensity at the focal distance in the presence and absence of FPZP. The deviation of the actual focal distance from the intended focal distance was also worse in the configuration with 6 mm and 8 mm apertures. On the other hand, the changes in the full width at half maximum (FWHM) followed the changes in the diffraction limit (ADL), which is inversely proportional to the aperture size. The full depth at half maximum (FDHM) measures the focusing resolution along the propagation axis. The FDHM was significantly improved with the aperture size.

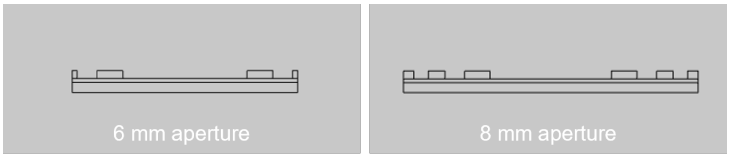

Figure 5.14: The geometrical setup of FPZP simulation with an aperture size of 6mm (left) and 8mm (right).

Table 5.6: Performance of the FPZP with various transducer aperture.

Aperture	6 mm	8 mm	10 mm
Maximum intensity (W/cm^2)	4.66	8.27	12.04
Focal gain (dB)	11.91	14.40	16.04
Focal distance (mm)	16.377	16.269	15.970
FWHM (mm)	0.435	0.332	0.260
ADL (mm)	0.435	0.326	0.261
FDHM (mm)	10.453	5.672	3.320
A/FD	0.4	0.53	0.67

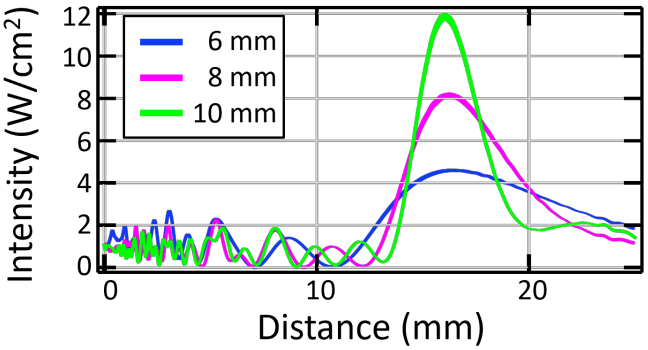

Figure 5.15: 1D intensity profile of FPZP perpendicular to the center of the transducer with the aperture of 6 mm (blue), 8 mm (magenta), and 10 mm (green).

Focal distance is also a factor that influences the diffraction limit. Three focal distances were simulated (10 mm, 15 mm, and 20 mm) at the aperture size of 10 mm. The performance of each configuration can be seen in Table 5.7. Looking at the maximum intensity achieved by each configuration, the configuration with a closer focal distance achieved a higher intensity. However, when comparing with its respective references, the focal gain of each configuration remained relatively constant, which indicates that the difference in maximum intensity was mostly influenced by the difference in unfocused intensity. The deviation of the focal depth from the expected depth was observed to be worse at longer focal distances. This trend was also previously observed in configurations with different apertures. When comparing the ratio of the aperture and intended focal distance, configurations with a lower ratio of aperture and focal distance exhibit higher deviation from the intended focal distance. A similar correlation between the A/FD ratio and FDHM was also observed. Configurations with better A/FD ratio showed a better FDHM. The comparison of the 1D intensity profile can be seen in Figure 5.16.

Table 5.7: Performance of the FPZP with various focal distances.

Focal distance	10 mm	15 mm	20 mm
Maximum intensity (W/cm^2)	16.79	12.04	8.29
Focal gain (dB)	17.48	16.04	14.41
Simulated depth (mm)	10.783	15.970	21.846
FWHM (mm)	0.176	0.260	0.354
ADL (mm)	0.174	0.261	0.348
FDHM (mm)	1.41	3.32	5.91
A/FD	1	0.67	0.5

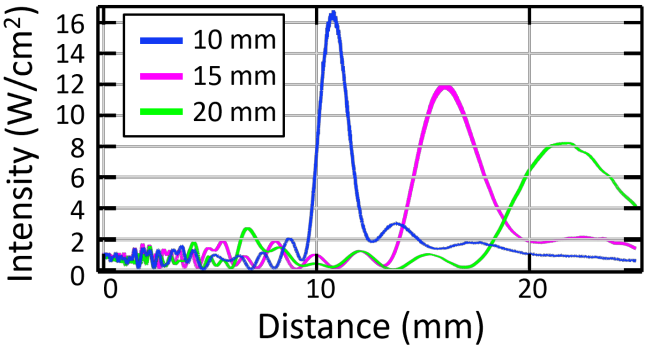

Figure 5.16: 1D intensity profile of FPZP perpendicular to the center of the transducer with the intended focal distance of 10 mm (blue), 15 mm (magenta) and 20 mm (green).

To summarize, optimizing the focal gain can be achieved by maximizing the aperture. The FWHM of the FPZP can be estimated using ADL in Eq.5.6. To maximize the accuracy of the focal distance and the axial focusing resolution, maximizing the ratio between aperture and focal distance has been seen to yield the best result.

EFFECT OF FREQUENCY VARIATION

During the implementation of the FPZP using a PZT piece, there can be a variation of center frequency in PZT pieces sourced from a single sheet due to defects and poling non-uniformity within the sheet. Since wavelength is a factor in the calculation of optimum Fresnel structure thickness, simulations were performed to predict the sensitivity of the FPZP performance against small variations in center frequency. The simulation used an FPZP structure meant for 8.5 MHz center frequency and 15 mm focal distance. The result of the simulations can be seen in Table 5.8. In general, the performance of the FPZP was stable in the range of 8.3 MHz to 9 MHz. The focal gain remained stable between 16.04 dB and 16.95 dB.

Table 5.8: Performance of the FPZP in the case of frequency variation.

Frequency (MHz)	8.3	8.5	9
Focal gain (dB)	16.95	16.04	16.28
FWHM (mm)	0.264	0.260	0.258
ADL (mm)	0.268	0.261	0.247
FDHM (mm)	3.30	3.32	3.54

NON-ZERO FOCUSING ANGLE

A non-zero focusing angle can be achieved within this model. The resulting FPZP will have structures that are no longer symmetrical. As presented in Eq.5.12, the center point of each transition radius X_n will deviate away from the center of the transducer. Thus, the focal angle that can be imposed on the FPZP is limited by the intended focal distance and the aperture of the transducer. The shape of the FPZP geometry in a 2D plane can be seen in Figure 5.17. At a steeper angle, the Fresnel structure on one side should appear outside of the transducer, as seen in the case of a 15-degree and 20-degree focusing angle. Figure 5.18 shows the 2D intensity profile of each configuration.

Table 5.9: The effect of non-zero focusing angles.

Focusing angle	0-degree	5-degree	10-degree	15-degree	20-degree
$F_D(mm)$	15.97	15.42	14.4	13.91	13.25
$\Delta_x(mm)$	0	1.30	2.45	3.68	4.78
Degree	0	4.82	9.655	14.82	19.84
Normalized intensity	1	0.985	0.936	1.111	0.604

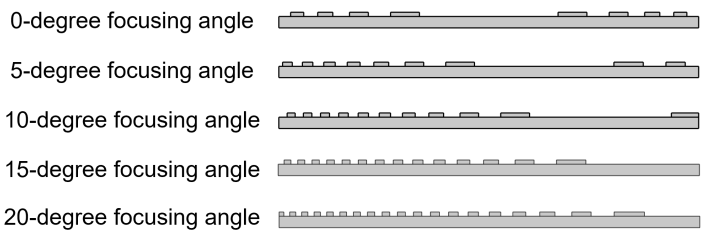

Figure 5.17: The geometrical structure of FPZP with the focusing angle of 0-degree, 5-degree, 10-degree, and 20-degree on a 10 mm wide transducer with a 15 mm intended focal distance.

The focusing angle is then calculated as the $arctan(\Delta_x/F_D)$, with Δ_x as the deviation of the focal spot from the center of the transducer measured in the lateral axis and F_D as the axial distance between the focal spot and the transducer. As the focusing angle increases, the axial focal distance decreases. Up to a 15-degree focusing angle, the FPZP was still able to form a single focal zone and maintain a comparable output intensity. A higher intensity at the 15-degree angle was seen, which could be due to the constructive interference with the stronger intensity zones emitted at the edges of the transducer.

The focusing was compromised at the 20-degree focusing angle as three distinct focal zones were formed. the maximum intensity was also reduced by 40% compared to the 0-degree focusing angle. The summary of the simulation results of the non-zero focusing angle can be seen in the Table 5.9.

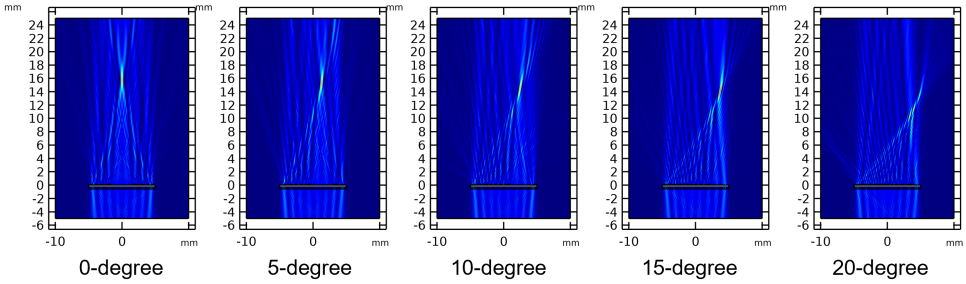

Figure 5.18: 2D intensity profiles of FPZP with 0-degree, 5-degree, 10-degree, 15-degree, and 20-degree focusing angle.

5.2.5. DISCUSSION

To conclude the simulation results, FPZP outperformed the convex lens and FZP when considering the attenuation during wave propagation. The FWHM of an FPZP is limited by ADL. The ratio of A/FD is an important factor to consider in maximizing the focusing resolution of an FPZP. The A/FD ratio affects both the FWHM and FDHM. Configurations with similar A/FD ratio in Table 5.6 and Table 5.7 exhibit similar FWHM and FDHM. The simulation algorithm can also generate a Non-zero focusing angle lens. The FPZP was shown to be able to accurately generate a focal spot up to 15-degree angle without losing much intensity. The FPZP exhibited minimal degradation in intensity across a range of small frequency variations (from 8.3-9.0 MHZ). This observation suggests that the influence of PZT thickness variations on the FPZP's performance may be negligible within this range.

5.3. FABRICATION METHOD

Based on the simulation result in the previous subsection, a proof-of-concept for FPZP was fabricated. The following design parameters will be pursued in order to fit the resulting focused ultrasound transducer in an existing *in vitro* setup. As previously described in the simulation, the FPZP consists of concentric rings with distinct sizes placed on top of a handling layer. The rings and the handling layer were made of a single material of PDMS that has a slightly different speed of sound than the target medium but has a similar acoustic impedance to minimize reflection from the interface. The approach that was taken to manufacture this structure was through a molding process, which utilizes silicon substrate as the molding material. Alternatives such as additive manufacturing using fused deposition modeling (FDM) and digital light processing (DLP) printing were considered in the making of the mold, as was done in the literature. However, FDM printing was limited in the printing resolution required to construct the lens. DLP on resin substrate offers the required printing resolution, which could achieve tens-

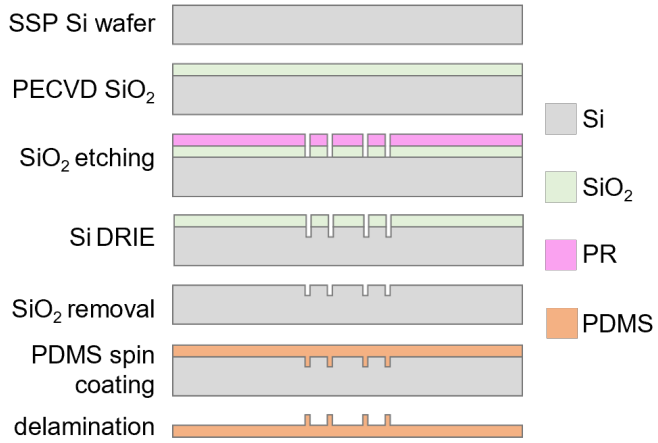

Figure 5.19: The fabrication process of the FPZP using a silicon mold.

of-micrometer in lateral resolution. However, it is sensitive to temperature change and could deformed due to thermal stress during the curing process of the PDMS. A silicon mold offers the advantage of high resolution, which allows for the fabrication of lenses with high frequency or short focal distance and temperature stability.

5.3.1. FABRICATION FLOW

The fabrication process of the PDMS FPZP is described in Figure 5.19. The fabrication starts with a 4-inch 500 μm-thick single-side polished (SSP) silicon wafer. Plasma-enhanced chemical vapor deposition (PECVD) silicon oxide was deposited on the wafer as a hard mask for deep reactive ion etching (DRIE). The thickness of the silicon dioxide can be adjusted to the desired Fresnel structure height. A 2 μm-thick silicon dioxide was used to provide flexibility in fabricating different structure height. Patterning on the hard mask was performed using a 3.5 μm-thick negative photoresist (AZ nLOF2020, MicroChemicals) and wet etching in buffered hydrofluoric acid (BHF 7:1). Afterward, DRIE was performed to remove the silicon (Omega Rapier i2L, SPTS Technologies). This etching step will determine the height of the Fresnel structure. The depth of the trenches was carefully measured during the process using the optical profilometer function of a laser scanning microscope (VK-X250, Keyence). The deposited photoresist would be consumed during the DRIE process, and any remaining photoresist layer was removed using a plasma asher (Plasma 300, PVA TePla America).

The silicon dioxide hard mask was then removed using BHF. The wafer was then cleaned with 100% nitric acid (HNO_3) and rinsed in deionized water. An anti-adhesion layer was then deposited on the wafer to ensure PDMS removal from the mold. Octafluorocyclobutane (C_4F_8) was deposited in a vapor phase in the DRIE machine to create a conformal and uniform anti-adhesive layer. An example of the resulting silicon mold can be seen in Figure 5.20.

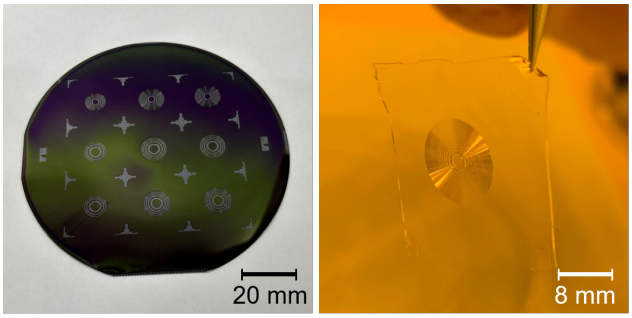

Figure 5.20: (left) The wafer-level mold of FPZP with multiple designs. (right) Free-standing PDMS FPZP.

A layer of PDMS (Sylgard 184, Dow) was spin-coated on the mold. A 2-part PDMS was used, and it was mixed with a 10:1 (monomer:curing agent) weight ratio. The solution was mixed and degassed in a centrifugal mixer (ARE-250, Thinky). The target thickness during spin-coating will determine the thickness of the handle layer of the lens. A thicker handle layer provides additional mechanical support to ease the handling of the lens. However, a thicker layer will reduce the focusing gain of the lens due to attenuation. Assuming an attenuation coefficient of 0.43 dB/mmMHz, every 100 μm PDMS would present 0.37 dB of attenuation at 8.5 MHz frequency. Sufficient mechanical support to easily handle the lens was seen with a handle layer thickness ranging from 1oo to 200 μm.

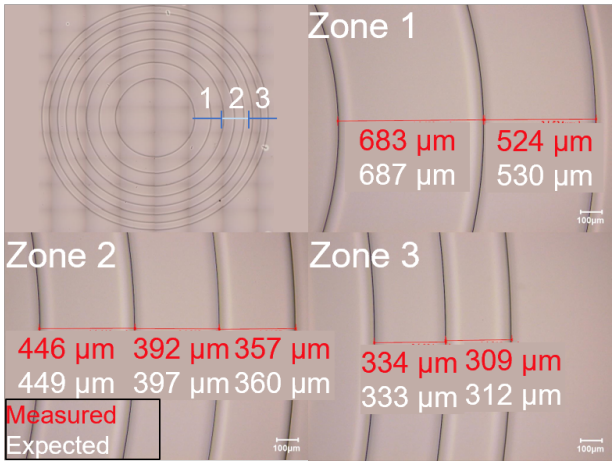

Figure 5.21: Measurement of the PDMS FPZP lateral dimensions. (Top-left) The stitched image is of the full PDMS FPZP. (top-right) The measurement of Zone 1. (bottom-left) The measurement of Zone 2. (bottom-right) The measurement of Zone 3. The number in red and white represent the measured dimension and expected dimension, respectively.

The wafer was degassed in a desiccator for approximately 20 minutes to remove air

bubbles trapped within the structure. Next, the PDMS was cured at 90°C for 1 hour in an oven. After curing, the PDMS was cut into individual lenses using a sharp knife on the lines predefined by the mold. Due to the anti-adhesive layer, the lenses could be removed with a tweezer and a drop of isopropyl alcohol (Figure 5.20). The lateral dimensions of the lens were optically compared with the expected dimensions as shown in Figure 5.21.

5.3.2. CRITICAL STEPS

DEEP REACTIVE ION ETCHING UNIFORMITY

The fidelity of the mold structure is critical, as any deviations in the mold will be directly transferred to the resulting FPZP. Assuming perfect filling of the PDMS into the mold without trapped air bubbles, it is more accurate to measure the dimensions of the resulting structure on the mold rather than directly measuring on the lens structure. The soft and transparent nature of PDMS made it difficult to measure accurately with both physical and optical profilemeter. There are two important points to consider in the shape of the trench, the shape of the bottom of the trench and the depth uniformity of the trenches. The desired shape, in this case is a trench with a rectangular cross-section, namely with a flat bottom side, smooth sidewall with minimal scalloping and sharp corners. In order to do so, a deep reactive ion etching with a high concentration of SF_6 and C_4F_6 was used during the etching and passivating cycle, respectively (details of the recipe used in this process can be found in the appendix). However the recipe for the DRIE still need to be optimized. One of the biggest challenges is the varying sizes of the structure within the FPZP which experience different etch rate and sidewall profile. To test the concept of FPZP, a 100 μm-deep mold was fabricated. The profile of this mold can be seen in Figure 5.22. The difference in mean depth of the largest opening and the smallest opening is around 0.3 μm, which indicates a similar etch rate within this range of opening sizes. However, the average sidewall angle is 81.29 °, thus introducing an error to the structure size at the bottom of the trench, which scales with the depth. The deviation caused by the sidewall angle affects more on the smaller structure as seen in Figure 5.22.

5.3.3. ASSEMBLY OF FPZP ON PMC TRANSDUCER

Individual FPZP can be mounted on top of a transducer with a PMC structure. The application of the FPZP to the PMC can be done by aligning the edges of the FPZP and PMC as shown in Figure 5.23. During the placement of the FPZP to the PMC, it is critical to ensure that there are no air pockets trapped between the two PDMS surfaces. At this step, the mechanical rigidity provided by the handle layer helps to ease the application process. Various methods using adhesive between the two interfaces, such as uncured PDMS and epoxy were explored. However, the additional materials worked detrimentally in achieving a bubble-free bonding. The best result was achieved by directly bonding the two interfaces without the use of adhesive on the interface. A thin layer of uncured PDMS was applied on the sidewall of the PMC and FPZP using a small syringe connected to a pneumatic dispenser. the device was then cured at 50 °C overnight. The resulting device can be seen in Figure 5.24.

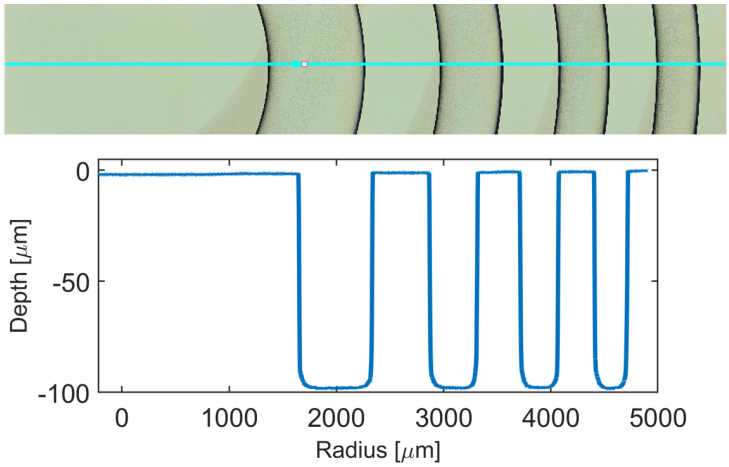

Figure 5.22: Optical surface profiling of the silicon Mold.

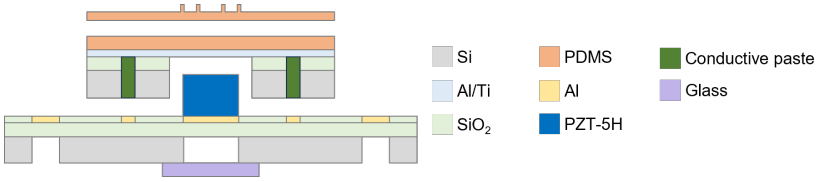

Figure 5.23: The assembly process of FPZP onto PMC and air-backed substrate.

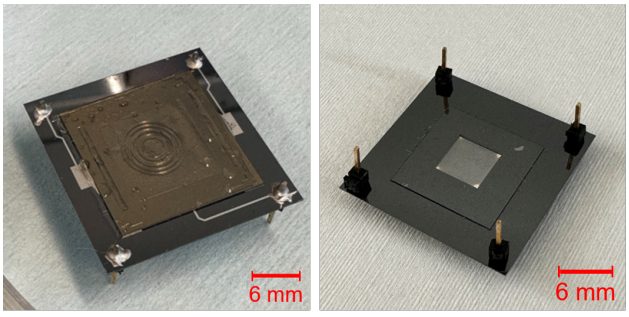

Figure 5.24: A photograph of the assembled FPZP on PMC and air-backed substrate:(left) top view, (right) bottom view.

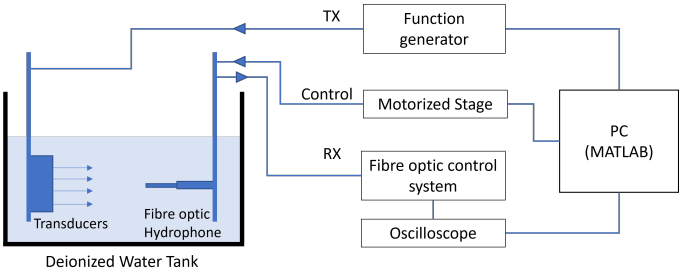

Figure 5.25: Schematic describing the measurement setup of ultrasound characterization.

5.4. ULTRASOUND CHARACTERIZATION

Focused ultrasound transducers with the specifications detailed in Table 5.10 were fabricated as a proof-of-concept for the implementation of the FPZP. In combination with the PMC and the air-backed silicon substrate, ultrasound characterization of the device was performed to experimentally validate the performance of the FPZP.

5.4.1. ULTRASOUND CHARACTERIZATION SETUP

The schematic of the measurement setup can be seen in Figure 5.25. The fabricated transducer was fixed in the tank half-filled with de-ionized water on a 3D-printed holder. The transducer was driven by a function generator (DG4202, RIGOL) which was controlled by a custom MATLAB interface. A fiber optic hydrophone (FOHS V2, Precision Acoustics) was used to measure the ultrasound waves generated by the transducer. The transducer was mounted on an XYZ motorized stage (VK62000, GAMPT mbH) to allow precise movements for capturing 2D ultrasound profiles. The readout of the hydrophone was done by an oscilloscope (DSO-X 3032A, Keysight), and the data was integrated into the MATLAB interface. The voltage readout collected from the oscilloscope was compared to the calibration data of the hydrophone to convert it into acoustic pressure and intensity. The signal used to characterize the transducers was bursts of 10 Vpp-square waves with a pulse repetition frequency (PRF) of 1 kHz; this PRF was chosen to give sufficient delay to avoid interference from the previous burst. Each burst contained 40 waves to allow for the transducer to reach the optimum steady state. Each acoustic field scan was preceded by finding the volumetric spatial intensity peak and resonance frequency to minimize the effect of material variation from sample to sample.

Table 5.10: Specification of the focused ultrasound transducer using FPZP.

PZT size	10 mm
PZT thickness	0.27 mm
Center frequency	8.5 MHz
Focusing angle	0 degree
Focal distance	15 mm
Fresnel structure height	0.1 mm

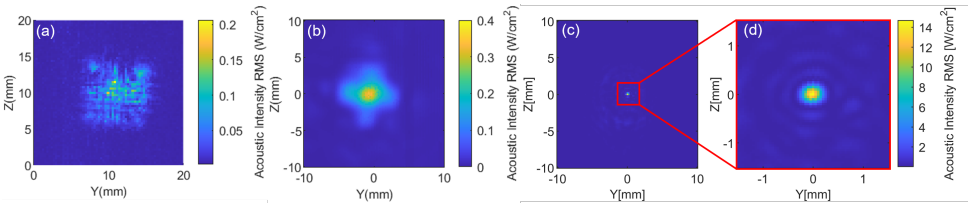

Figure 5.26: (a) The lateral cross-section of the intensity beam profile of unfocused ultrasound transducer at 15 mm distance. (b) The lateral cross-section of the intensity beam profile of the unfocused ultrasound transducer measured at its natural focal distance (c) The lateral cross-section of the intensity beam profile of the focused ultrasound with FPZP at 16.0 mm distance with 0.2 mm scanning resolution. (d) close-up of the focal spot of the focused intensity beam profile with 0.05 mm scanning resolution.

5.4.2. MEASUREMENT RESULTS

The measurement was started by roughly finding the transducer's focal spot. At the provisional focal spot, the frequency response of the transducer was measured by sweeping the driving frequency from 0.1 to 16 MHz with a resolution of 0.1 MHz. It is important to note that a hydrophone has non-constant sensitivity across frequencies. Figure 5.28(a) shows the frequency response of the transducer FPZP adjusted to the sensitivity variation in the frequency of the hydrophone. The transducer's resonance frequency was measured at 9.1 MHz, which was higher than the expected 8.5 MHz for which the lens was designed. The -3 dB bandwidth of the transducer was 0.5228 MHz, which indicates a quality factor of 17.4, calculated as the ratio of the center frequency and the -3 dB bandwidth.

At the resonance frequency, a lateral cross-section of the intensity beam profile of the FPZP at a distance of 16.0 mm away from the transducer can be seen in Figure 5.26(c-d). The distance from the transducer was measured using the time of flight method by assuming the speed of sound in the medium as 1480 m/s. As a reference, the beam profile of the transducer at a 15 mm distance and at its natural focal distance at 150 mm can be seen in Figure 5.26(a-b). The effect of focusing can clearly be seen by comparing the two profiles. The FWHM of the device was measured as 0.25 mm, which aligns with the calculated ADL of 0.244 mm at 9.1 MHz.

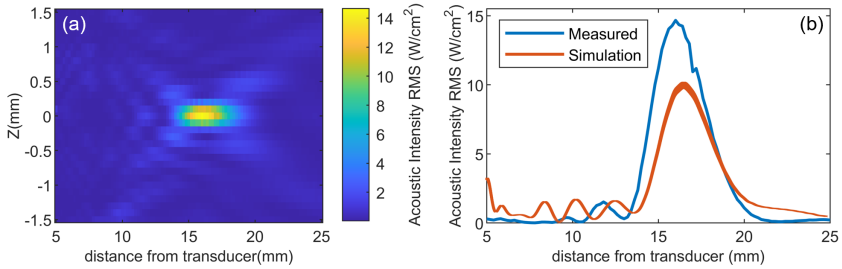

Figure 5.27: (a) The axial cross-section of the intensity beam profile of the FPZP from 5 mm to 25 mm distance from the transducer. (b) Comparison between the simulation and the measurement of the axial intensity profile across the focal spot.

Figure 5.27(a) shows the axial cross-section of the beam profile measured from the distance of 5 mm to 25 mm away from the transducer. The FDHM of the transducer was measured at 3.2 mm. A 1D intensity plot was extracted from the axial cross-section across the focal spot. The 1D intensity plot was then compared to the simulation result as seen in Figure 5.1(b), indicating an agreement between the simulated and the measured results. Focal gain was then calculated by comparing the maximum intensity achieved by the FPZP to the unfocused beam profile Figure 5.28(b). The gain was calculated as 98.847 or 19.95 dB.

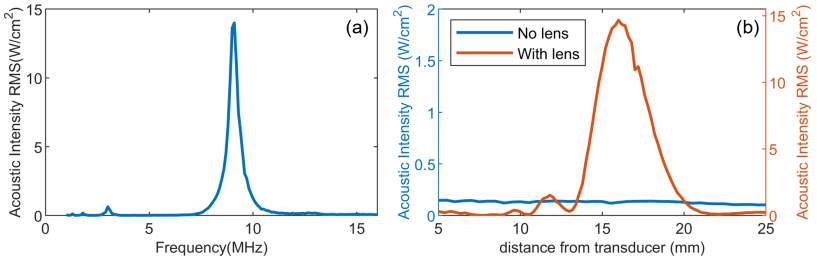

Figure 5.28: (a) The output intensity of the FPZP transducer as a function of frequency, adjusted to account for the sensitivity variance of the hydrophone. (b) The comparison between the intensity of the unfocused and focused ultrasound transducer measured between 5 mm and 25 mm.

5.5. DISCUSSION

Using COMSOL simulation and microfabrication techniques, an FPZP was simulated and fabricated. Table 5.11 compares the results of the unfocused ultrasound transducer, the measurement result of the FPZP and the simulated results. While good agreement was observed between the measured and simulated spatial resolutions, a discrepancy in the focal gain and intensity can be seen. This discrepancy can be attributed to the material characteristics used in the simulation. The difference in focal gain was largely affected by the material properties of the lens, more specifically, the attenuation coefficient, which, unlike density and sound velocity, was under-reported in the literature. The difference in the absolute value of the intensity can be attributed to the difference in the piezoelectric characteristic of the PZT-5H. The simulation should be performed using an extracted parameter of the actual PZT used during the fabrication to achieve a better fit. Nevertheless, even without accurate piezoelectric characteristics, simulation results can provide helpful insight into parameters not affected by the pressure amplitude generated by the transducer, such as spatial resolution.

Compared to other works utilizing a similar principle [28], [34], the work presented achieved the smallest spatial resolution with 0.25 mm and 3.2 mm of FWHM and FDHM, respectively. This improvement in spatial resolution is partly due to the higher frequency that can be achieved by our fabrication technique, which allows for a lower diffraction limit. The difference in transducer size and focal distance could also play a role in the FWHM as described in Eq.5.6 and Eq.5.7.

A few works have presented the focal gain of the lens since it is not as crucial in applications such as imaging [38] and NDT [34]. [28] presented a 3D-printed FPZP made

Table 5.11: Performance of the fabricated FPZP compared to the FEM in COMSOL.

Parameter	Unfocused	Focused	focused-simulation
Peak intensity (W/cm^2)	0.15	14.67	10.22
Focal gain (dB)	-	19.95	15.33
FWHM (mm)	~ 10	0.25	0.258
FDHM (mm)	-	3.20	3.54
Distance (mm)	15	16	16.45
Scan resolution (mm)	0.2	0.05	-

Table 5.12: Performance comparison of the FPZP to other fabricated works.

	Focal gain (dB)	Transmit efficiency (kPa/V)	FWHM (mm)	FDHM (mm)	Aperture (mm)	Frequency (MHz)
This work	19.95	66	0.25	3.2	10	9.1
Tang [24]	-	11	0.7	3.74	36	2.32
Tarrazo-Serrano [28]	21.90	-	1.91	8.81	12.7	1
Dolmatov [34]	-	-	1.475	11.127	25.4	5.55
Wang [38]	-	-	0.65	6.5	25	5

of PLA with a gain of 21.9 dB at 1 MHz frequency. Due to the lower frequency, smaller attenuation was introduced by the lens, resulting in lower loss. The 3D printing approach of the PLA FPZP allows for rapid lens prototyping. However, it is limited to low frequencies due to the printing resolution (0.1 to 0.3 mm). Therefore, our FPZP could achieve a much smaller focal area due to the possibility of utilizing a higher frequency. Another drawback is the difficulty of integrating the 3D-printed FPZP as presented in [28] and [34] in a setup with limited space, such as in an enclosed fluorescence microscope used in *in vitro* studies. Therefore, it is still advantageous to have an FPZP that can be integrated into a transducer in a small form factor.

The fabrication process still needs to be optimized to achieve the optimized thickness of the Fresnel structure using the DRIE process to achieve a better sidewall and bottom profile. The flatness of the bottom side can be improved by having a buried stopping layer of silicon dioxide, which allows for over-etching to achieve a smooth and flat bottom surface. The sidewall profile can be improved by adjusting the combinations of etching parameters, such as pressure, power, and gas flow rate. Using higher flow rate, coil power, and platten power have been shown to improve the sidewall angle in the DRIE process at the cost of lateral accuracy [39],[40]. Further work is required to find the balance between accuracy and sidewall angle and improve the uniformity across different opening sizes.

5.6. CONCLUSION

This chapter presented the simulation, fabrication, and measurement of an FPZP made of PDMS. The PDMS FPZP can be fabricated using a molding process, which involves making the mold using a single photolithography step. The process is suitable for creating FPZP lenses for high-frequency ultrasound by leveraging microfabrication technologies that can provide the required fabrication resolution. The FEM performed in the COMSOL environment allows for the prediction of the performance of the FPZP. The FEM shows the different dependencies of design parameters in influencing the performance of the FPZP. The importance of the transducer's aperture, focal distance, and Fresnel structure thickness was identified to maximize the focusing gain and resolution.

As a proof-of-concept, a focused ultrasound transducer with a frequency of 9.1 MHz was fabricated by building upon the transducer utilizing an air-backed substrate and PMC. The measurement result validated the proposed PDMS FPZP, which demonstrated a FWHM of 0.25 mm and FDHM of 3.2 mm. The focal gain of 19.95 dB was also measured when comparing the intensity at a location with and without the presence of the lens. The focal gain achieved was comparable to the state-of-the-art while providing the advantage of a smaller form factor. The focusing resolution achieved in this work showed the advantage of FPZP fabrication using a microfabrication process compared to additive manufacturing. The work demonstrated in this chapter successfully achieved better-focusing resolution compared to the state-of-the-art utilizing a similar focusing approach.

For future work, optimization of the DRIE process in order to improve the uniformity and sidewall angle of the etching across differently-sized openings can improve the performance of the FPZP as suggested by the simulation results. The FEM of the FPZP can accurately predict the focusing spatial characteristics. However, a more accurate model of the materials used in the simulation can help improve the prediction accuracy of the intensity and the focusing gain of the FPZP. Despite these challenges, this chapter demonstrated a wafer-level approach to fabricating a miniaturized FPZP using a single-photolithography step and a simulation environment that can aid the design of the FPZP for other applications.

BIBLIOGRAPHY

[1] F. Ma, Z. Huang, C. Liu, and J. H. Wu, "Acoustic focusing and imaging via phononic crystal and acoustic metamaterials", *Journal of Applied Physics*, vol. 131, 1 Jan. 2022, ISSN: 10897550. DOI: 10.1063/5.0074503.

[2] H. Baek, D. Lockwood, E. J. Mason, *et al.*, "Clinical intervention using focused ultrasound (fus) stimulation of the brain in diverse neurological disorders", *Frontiers in Neurology*, vol. 13, May 2022, ISSN: 16642295. DOI: 10.3389/fneur.2022.880814.

[3] S. Yang, W. Qin, H. Guo, *et al.*, "Design and evaluation of a compound acoustic lens for photoacoustic computed tomography", *Biomedical Optics Express*, vol. 8, p. 2756, 5 May 2017, ISSN: 2156-7085. DOI: 10.1364/boe.8.002756.

[4] W. Lee and Y. Roh, "Ultrasonic transducers for medical diagnostic imaging", *Biomedical Engineering Letters*, vol. 7, pp. 91–97, 2 May 2017, ISSN: 2093985X. DOI: 10.1007/s13534-017-0021-8.

[5] G. L. Barbruni, P. M. Ros, D. Demarchi, S. Member, S. Carrara, and D. Ghezzi, "Miniaturised wireless power transfer systems for neurostimulation: A review", *IEEE TRANSACTIONS ON BIOMEDICAL CIRCUITS AND SYSTEMS*, vol. 14, 6 2020. DOI: 10.1109/TBCAS.2020.3038599. [Online]. Available: https://doi.org/10.1109/TBCAS.2020.3038599..

[6] Z. Izadifar, Z. Izadifar, D. Chapman, and P. Babyn, "An introduction to high intensity focused ultrasound: Systematic review on principles, devices, and clinical applications", *Journal of Clinical Medicine*, vol. 9, 2 Feb. 2020, ISSN: 20770383. DOI: 10.3390/jcm9020460.

[7] W. Legon, P. Bansal, R. Tyshynsky, L. Ai, and J. K. Mueller, "Transcranial focused ultrasound neuromodulation of the human primary motor cortex", *Scientific Reports*, vol. 8, p. 10 007, 2018. DOI: 10.1038/s41598-018-28320-1. [Online]. Available: www.simnibs.de.

[8] W. Lee, H. Kim, Y. Jung, I. U. Song, Y. A. Chung, and S. S. Yoo, "Image-guided transcranial focused ultrasound stimulates human primary somatosensory cortex", *Scientific Reports*, vol. 5, 2015, ISSN: 20452322. DOI: 10.1038/srep08743.

[9] M. Duque, C. A. Lee-Kubli, Y. Tufail, *et al.*, "Sonogenetic control of mammalian cells using exogenous transient receptor potential a1 channels", *Nature Communications*, vol. 13, 1 Dec. 2022, ISSN: 20411723. DOI: 10.1038/s41467-022-28205-y.

[10] P. S. Balasubramanian, A. Singh, C. Xu, and A. Lal, "Ghz ultrasonic chip-scale device induces ion channel stimulation in human neural cells", *Scientific Reports*, vol. 10, 1 Dec. 2020, ISSN: 20452322. DOI: 10.1038/s41598-020-58133-0.

[11] M. C. Pan, T. A. Bui, Y. C. Nien, and W. C. Shih, "Design and fabrication of fresnel lens and zno thin-film transducer", *Japanese Journal of Applied Physics*, vol. 50, 7 PART 2 Jul. 2011, ISSN: 00214922. DOI: 10.1143/JJAP.50.07HD02.

[12] Z. Hu, Y. Yang, L. Xu, Y. Jing, and H. Chen, "Airy-beam-enabled binary acoustic metasurfaces for underwater ultrasound-beam manipulation", *Physical Review Applied*, vol. 18, 2 Aug. 2022, ISSN: 23317019. DOI: 10.1103/PhysRevApplied.18.024070.

[13] Z. Hu, Y. Yang, L. Yang, *et al.*, "Airy-beam holographic sonogenetics for advancing neuromodulation precision and flexibility", *Proceedings of the National Academy of Sciences*, vol. 121, 26 Jun. 2024, ISSN: 0027-8424. DOI: 10.1073/pnas.2402200121. [Online]. Available: https://pnas.org/doi/10.1073/pnas.2402200121.

[14] H. Rivandi and T. L. Costa, "A 2d ultrasound phased-array transmitter asic for high-frequency us stimulation and powering", *IEEE Transactions on Biomedical Circuits and Systems*, vol. 17, pp. 701–712, 4 Aug. 2023, ISSN: 19409990. DOI: 10.1109/TBCAS.2023.3288891.

[15] T. Costa, C. Shi, K. Tien, J. Elloian, F. A. Cardoso, and K. L. Shepard, "An integrated 2d ultrasound phased array transmitter in cmos with pixel pitch-matched beamforming; an integrated 2d ultrasound phased array transmitter in cmos with pixel pitch-matched beamforming", *IEEE Transactions on Biomedical Circuits and Systems*, vol. 15, 4 2021. DOI: 10.1109/TBCAS.2021.3096722. [Online]. Available: https://www.ieee.org/publications/rights/index.html.

[16] Y. Hosono, Y. Yamashita, and K. Itsumi, "Effects of fine metal oxide particle dopant on the acoustic properties of silicone rubber lens for medical array probe", *IEEE Transactions on Ultrasonics, Ferroelectrics, and Frequency Control*, vol. 54, pp. 1589–1595, 8 Aug. 2007, ISSN: 08853010. DOI: 10.1109/TUFFC.2007.429.

[17] J. Jang and J. H. Chang, "Design and fabrication of double-focused ultrasound transducers to achieve tight focusing", *Sensors (Switzerland)*, vol. 16, 8 Aug. 2016, ISSN: 14248220. DOI: 10.3390/s16081248.

[18] H. Fujii, C. Nakaya, H. Takeuchi, T. Kondo, and Y. Ishikawa, "Acoustic properties of lens materials for ultrasonic probes", *Japanese Journal of Applied Physics*, vol. 34, no. 1R, p. 312, Jan. 1995. DOI: 10.1143/JJAP.34.312. [Online]. Available: https://dx.doi.org/10.1143/JJAP.34.312.

[19] J. Elton, "A light to lighten our darkness: Lighthouse optics and the later development of fresnel's revolutionary refracting lens 1780–1900", *The International Journal for the History of Engineering & Technology*, vol. 79, no. 2, pp. 183–244, 2009. DOI: 10.1179/175812109X449612.

[20] Y. Sato, K. Mizutani, N. Wakatsuki, and T. Nakamura, "Design for an aspherical acoustic fresnel lens with phase continuity", *Japanese Journal of Applied Physics*, vol. 47, pp. 4354–4359, 5 PART 2 May 2008, ISSN: 00214922. DOI: 10.1143/JJAP.47.4354.

[21] Y. H. Huang and J. Y. Jeng, "Forming a fresnel zone lens: Effects of photoresist on digital-micromirror-device maskless lithography with grayscale exposure", *Journal of the Optical Society of Korea*, vol. 16, pp. 127–132, 2 Jun. 2012, ISSN: 12264776. DOI: 10.3807/JOSK.2012.16.2.127.

[22] S. Pérez-López, J. M. Fuster, P. Candelas, D. Tarrazó-Serrano, S. Castiñeira-Ibáñez, and C. Rubio, "Bifocal ultrasound focusing using bi-fresnel zone plate lenses", *Sensors (Switzerland)*, vol. 20, 3 Feb. 2020, ISSN: 14248220. DOI: 10.3390/s20030705.

[23] A. Petosa, S. Thirakoune, and A. Ittipiboon, "Reconfigurable fresnel-zone-plate-shutter antenna with beam-steering capability", *IEEE Antennas and Propagation Magazine*, vol. 49, 5 2007, ISSN: 10459243.

[24] Y. Tang, S. Liu, and E. S. Kim, "Mems focused ultrasonic transducer with air-cavity lens based on polydimethylsiloxane (pdms) membrane", in *2020 IEEE 33rd International Conference on Micro Electro Mechanical Systems (MEMS)*, IEEE, 2020, pp. 58–61. DOI: 10.1109/MEMS46641.2020.9056313.

[25] Y. Tang and E. S. Kim, "Simple sacrificial-layer-free microfabrication processes for air-cavity fresnel acoustic lenses (acfals) with improved focusing performance", *Microsystems and Nanoengineering*, vol. 8, 1 Dec. 2022, ISSN: 20557434. DOI: 10.1038/s41378-022-00407-w.

[26] T. A. Bui, M. C. Pan, C. C. Lee, and W. C. Shih, "Effect of fabrication parameters on the characteristics of fresnel lens and piezoelectric transducers", *Ferroelectrics*, vol. 437, pp. 70–80, 1 2012, ISSN: 00150193. DOI: 10.1080/00150193.2012.741941.

[27] S. Hosseini, K. Laursen, A. Rashidi, T. Mondal, B. Corbett, and F. Moradi, "S-mrut: Sectored-multiring ultrasonic transducer for selective powering of brain implants", *IEEE Transactions on Ultrasonics, Ferroelectrics, and Frequency Control*, vol. 68, pp. 191–200, 1 Jan. 2021, ISSN: 15258955. DOI: 10.1109/TUFFC.2020.3001084.

[28] D. Tarrazó-Serrano, S. Pérez-López, P. Candelas, A. Uris, and C. Rubio, "Acoustic focusing enhancement in fresnel zone plate lenses", *Scientific Reports*, vol. 9, 1 Dec. 2019, ISSN: 20452322. DOI: 10.1038/s41598-019-43495-x.

[29] E. Liu, Y. Liu, X. Wang, *et al.*, "Design of acoustic fresnel zone plate for contact stress measurement of aero-engine rotor mating surface", *Journal of Sound and Vibration*, vol. 500, May 2021, ISSN: 10958568. DOI: 10.1016/j.jsv.2021.116035.

[30] S. Zhang, L. Yin, and N. Fang, "Focusing ultrasound with an acoustic metamaterial network", *Physical Review Letters*, vol. 102, 19 May 2009, ISSN: 00319007. DOI: 10.1103/PhysRevLett.102.194301.

[31] Y. Li, B. Liang, X. Tao, X. F. Zhu, X. Y. Zou, and J. C. Cheng, "Acoustic focusing by coiling up space", *Applied Physics Letters*, vol. 101, 23 Dec. 2012, ISSN: 00036951. DOI: 10.1063/1.4769984.

[32] S. C. S. Lin, T. J. Huang, J. H. Sun, and T. T. Wu, "Gradient-index phononic crystals", *Physical Review B - Condensed Matter and Materials Physics*, vol. 79, 9 Mar. 2009, ISSN: 10980121. DOI: 10.1103/PhysRevB.79.094302.

[33] H. Jia, M. Ke, R. Hao, Y. Ye, F. Liu, and Z. Liu, "Subwavelength imaging by a simple planar acoustic superlens", *Applied Physics Letters*, vol. 97, 17 Oct. 2010, ISSN: 00036951. DOI: 10.1063/1.3507893.

[34] D. O. Dolmatov, D. Tarrazó-Serrano, G. A. Filippov, A. Uris, and D. A. Sednev, "Application of phase-reversal fresnel zone plates for high-resolution robotic ultrasonic non-destructive evaluation", *Sensors*, vol. 21, 23 Dec. 2021, ISSN: 14248220. DOI: 10.3390/s21237792.

[35] H. Shankar and P. S. Pagel, "Potential adverse ultrasound-related biological effects: A critical review", *Anesthesiology*, vol. 115, pp. 1109–1124, 5 2011, ISSN: 15281175. DOI: 10.1097/ALN.0b013e31822fd1f1.

[36] N. N. Liu, Y. D. Cui, B. C. Khoo, and A. M. Zhang, "Damage characteristics of elastic material through a thin membrane using high-intensity focused ultrasound (hifu)", *AIP Advances*, vol. 8, 11 Nov. 2018, ISSN: 21583226. DOI: 10.1063/1.5050432.

[37] I. Miranda, A. Souza, P. Sousa, *et al.*, "Properties and applications of pdms for biomedical engineering: A review", *Journal of Functional Biomaterials*, vol. 13, 1 Mar. 2022, ISSN: 20794983. DOI: 10.3390/jfb13010002.

[38] D. Wang, P. Lin, Z. Chen, *et al.*, "Evolvable acoustic field generated by a transducer with 3d-printed fresnel lens", *Micromachines*, vol. 12, 11 Nov. 2021, ISSN: 2072666X. DOI: 10.3390/mi12111315.

[39] I. U. Abhulimen, S. Polamreddy, S. Burkett, L. Cai, and L. Schaper, "Effect of process parameters on via formation in si using deep reactive ion etching", *Journal of Vacuum Science & Technology B: Microelectronics and Nanometer Structures Processing, Measurement, and Phenomena*, vol. 25, pp. 1762–1770, 6 Nov. 2007, ISSN: 1071-1023. DOI: 10.1116/1.2787869.

[40] T. Xu, Z. Tao, H. Li, X. Tan, and H. Li, "Effects of deep reactive ion etching parameters on etching rate and surface morphology in extremely deep silicon etch process with high aspect ratio", *Advances in Mechanical Engineering*, vol. 9, 12 Dec. 2017, ISSN: 16878140. DOI: 10.1177/1687814017738152.

6

Anti-reflective Microengineered Structure

Poor stimulus-response correlation, caused by acoustic reflections from conventional culture substrates, poses a significant challenge in cellular mechanistic studies of ultrasound neuromodulation. Existing specialized setups that mitigate this interference have limited recording capabilities. This chapter proposes an anti-reflective microengineered substrate (ARMS) that can be incorporated into a standard in vitro platform. The substrate's dimensions and material composition were optimized in simulation. The optimized simulated platform exhibited an 86.3% reduction in reflection amplitude on the substrate surface compared to the conventional glass substrate. Furthermore, the ARMS reduced stimulation signal distortion to a 19.2% deviation from the expected amplitude, a substantial improvement compared to the 76.4% deviation observed with glass.

Parts of this chapter have been published in [1].

6.1. INTRODUCTION

In vitro models are invaluable tools for drug and treatment development, particularly for high throughput screening, safety assessment, and mechanistic studies. Currently, the scientific community has not yet agreed on the exact mechanisms of ultrasound neuromodulation and how different ultrasound parameters could affect the excitation or inhibition of neurons. Efforts to understand the efficacy and mechanism of ultrasound neuromodulation were primarily conducted using *in vitro* and anesthetized small animal models [2]. Ultrasound experiments on small animal models are considered more complex due to the ethical limitation in handling the animals and the influence of the anesthesia on the stimulus-response [3]. *In vitro* models offer a simpler and more controlled system to study the cellular mechanisms of ultrasound neuromodulation, which could avoid the side effects introduced by anesthetization [4]. However, commercially available platforms are not compatible with acoustic stimuli [5]. A typical *in vitro* platform consists of a small well with a plastic or glass substrate that contains the cells, tissues, or slices in a culture medium. In the presence of an acoustic wave traveling within the liquid medium, the enclosed nature of these platforms causes reflection, which echoes within the well (Figure 6.1(a)). This condition is in contrast to the calibration setup of an ultrasound transducer, which provides the stimuli that are typically characterized in a relatively large open space with an echo-free condition. The reflection can interfere with the acoustic stimuli, altering the amplitude and duration of the expected stimuli. The altered stimuli can cause a poor stimulus-response correlation conducted in an *in vitro* platform. For instance, studies conducted on hippocampal slices using an MEA platform have reported varying minimum pressure thresholds ranging from 11.52 kPa to 2.5 MPa [5], [6], [7]. Furthermore, given that the transducer is parallel to the reflective well plate base, this can lead to the occurrence of standing waves, if the distance between the transducer and the well plate base is a multiple of half of the sound wavelength [8]. While this feature is typically explored in particle levitation and manipulation, it is highly undesirable for ultrasound neuromodulation [8].

6.1.1. STATE-OF-THE-ART CELL CULTURE SUBSTRATE FOR *in vitro* ULTRASOUND STUDIES

Studies that reported higher acoustic pressure addressed the issue of reflection by predicting its effect on the stimulus waveform in their reporting [4], [5]. The prediction of the actual stimulus waveform was performed by using a Finite element model (FEM). A pressure amplitude deviation of more than 100% higher than the expected amplitude was seen on a focused ultrasound transducer placed on top of an MEA. The drawback of this method is the difficulty in validating the simulation result. A wave visualization technique such as the Schlieren imaging could be used to validate the wave propagation. However, this required a specialized setup and expertise to interpret the resulting images [4]. The prediction made in FEM also assumed an ideal placement of the transducer relative to the substrate, with the transducer placed perfectly parallel to the surface of the substrate. Interference is sensitive towards the angle of incidence and distance of the transducer due to the reflection and refraction of the waves. Another approach is to create a custom substrate that minimizes ultrasound reflection. Yoo et al. demonstrated a dedicated setup that used mylar film suspended on degassed water as a culture sub-

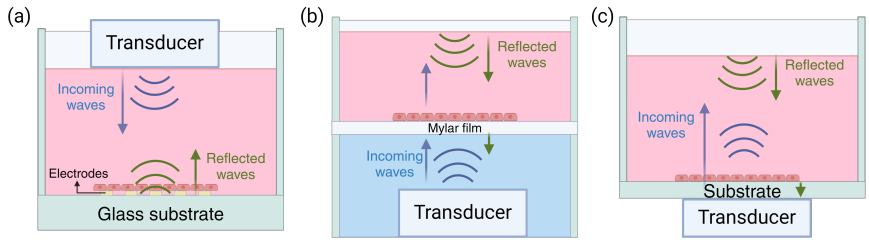

Figure 6.1: Schematics of *in vitro* ultrasound neuromodulation: (a) Ultrasound transducer placed on MEA/microplate platform [6],[4], (b) cell cultured on Mylar film with transducer submerged in degassed water on the backside of the mylar film [9], (c) Ultrasound transducer placed on the bottom of the culture through the substrate [10], [11].

strate (Figure 6.1(b)) [9]. This considerably reduced the reflection due to the acoustic impedance of a mylar film, which is more similar to the culture medium compared to glass. However, this approach limits the adoption of the setup due to its incompatibility with typical *in vitro* instruments. The use of suspended mylar film reduces the options of recording modality to microscopy-based characterization, such as calcium imaging [9]. Since the incorporation of electrodes was not possible on mylar film, this strategy cannot implement electrophysiological characterizations. Another approach was to provide stimulation from below the well plate. An ultrasound transducer was placed directly underneath the culture substrate (Figure 6.1(c)) [10],[11]. Therefore, the culture substrate can be considered part of the transducer, and *in situ* characterization of the transducer can be done by placing a hydrophone on top of the well. Reflection can still occur in the interface between air and medium above the well. However, this can be minimized by having a sufficiently deep well or placing an acoustic absorber [10]. The main drawback of this approach is the low transmit efficiency of the transducer since ultrasound waves have to travel across a glass [10] or silicon [11] before reaching the cells. The resulting transmit efficiency of 1.5 kPa/V was presented [10]. Moreover, this approach cannot utilize focusing techniques to improve its efficiency since the cell culture was placed directly above the transducer [10],[11]. The electrodes containing high voltage (100 V_{pp}) to drive the piezoelectric transducer had to be placed close to the cells, which could induce a risk of cross-sensitivity to the electric field [10].

6.2. PROPOSED CONCEPT: ANTI-REFLECTIVE STRUCTURE

Mitigating acoustic reflections or echoes coming from a certain surface is a topic that has been explored in applications such as sound engineering and sonar stealth [12]. Minimization in reflection was achieved not only through material selection, but these applications also utilize surface structural design by implementing an array of pillars or cavities to further reduce the amplitude of reflection [13]. Taking inspiration from these applications, in this study, we proposed an integrated anti-reflective micro-engineered structure (ARMS) implemented in the substrate of an *in vitro* platform. The ideal platform that was envisioned should fulfill these criteria: (1) It should be able to minimize ultrasound reflection and preserve the stimulation fidelity. (2) it should have a biocom-

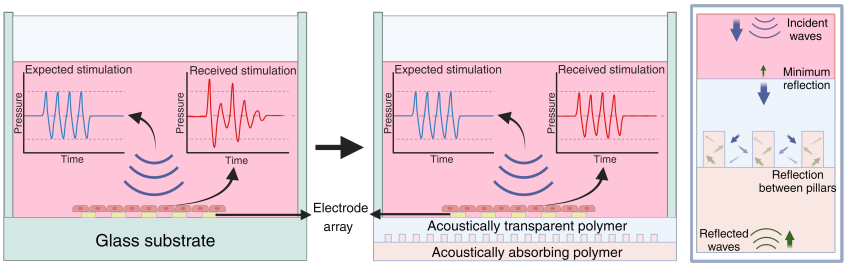

Figure 6.2: Concept of the ARMS compared to conventional *in vitro* platform. The ARMS comprises two layers of polymers with distinct purposes. The first layer acts as a biocompatible interface with an electrode array, and the second layer dissipates the acoustic reflection. The interface between the two polymers is shaped into an array of pillars to distribute the energy across time.

patible interface to contain the biological sample. (3) it should allow for the implementation of electrodes for electrophysiological characterization. (4) the structure should be able to be implemented into a typical *in vitro* platform, such as MEAs and microplates, to offer compatibility with standard laboratory instruments. Polymers, as a family of materials, have an acoustic impedance that is close to water, making them suitable for minimizing reflection in a liquid medium [12]. It is also widely adopted in *in vitro* platform that recapitulates biological physiology [14]. The concept of the proposed ARMS can be seen in Figure 6.2. The concept consists of two polymers that can be placed underneath culture wells. The first layer of polymer acts as a biocompatible interface on which electrodes can be deposited and patterned, and on top of which cells can be cultured. While the second layer of polymer acts as a wave absorber. The interface between the polymers forms an array of pillars that serve as the anti-reflective structure. The structure works by increasing the number of bounces a wave makes on an interface. On each bounce, the wave is partially transmitted and reflected, thus distributing the wave's energy over time.

6.2.1. NUMERICAL SIMULATION

The design of ARMS was explored using numerical simulation in MATLAB using the k-Wave toolbox. The numerical simulation was performed in the time domain to simulate the propagation of waves across a 2D space. The focus of this study is to optimize the dimensions and material composition of ARMS. The material selection in this study is limited to non-composite polymers that don't contain filler materials to limit the complexity of the model.

6.2.2. SIMULATION SETUP OF ARMS

The simulation setup used in the k-Wave toolbox can be seen in Figure 6.3. The model of ARMS consists of 3 main components: the ultrasound source, the first, and the second layer of polymers. The ultrasound source was placed at a fixed distance from the substrate, and a single ultrasound pulse was generated at a desired frequency. Due to the computational burden, the optimization of the ARMS will primarily be focused on 1-2

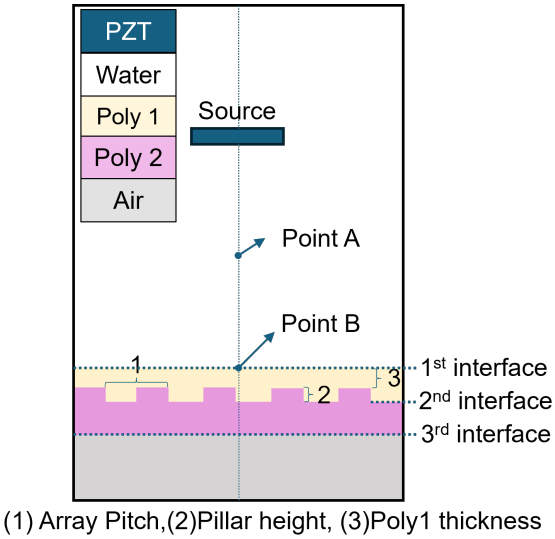

Figure 6.3: The schematic of the simulation setup of ARMS in k-Wave.

MHz. This is also aligned with the typically reported ultrasound frequency used in the literature [2]. Validation of the efficacy of the optimized design was also performed in the frequency band of 1-8 MHz. A perfectly matched boundary condition was applied to the boundary of the simulation space to avoid the reflection of waves due to the finite simulation space. Therefore, reflection within the space can only occur due to the components introduced in the simulation space. On the other side of the polymer layers, an air layer was applied to mimic the worst realistic scenario of the device. There are 3 material interfaces within ARMS, which will be the source of reflection of the incoming waves. The 1^{st} interface is between the propagating medium and the first layer of polymer, Water is widely used as a model for soft tissue and culture medium due to its similarity in acoustic properties. Since this interface was flat, the reflection is solely dependent on the mismatch of the acoustic impedance between the medium and the first polymer. The 2^{nd} interface was between the first and second polymers. This interface is fashioned into pillars as the anti-reflective structure. The 3^{rd} interface was between the second polymers and the air layer. This interface reflected entirely incident waves. Two observation points recording the pressure along the duration of the simulation were established, namely, Point A and Point B. Point A was used to observe the echoes coming from the material interfaces within the substrate, and it was placed at a halfway distance between the source and the reflecting surface. The distance between the reflecting surface and the observation point allowed reflection from each interface to arrive at different times. Therefore, the reflection amplitude of each interface can be identified. Point B was used to observe the fidelity of the stimulation signal, and it was placed on the surface of the substrate (1^{st} interface) where the cells would be positioned. Three dimensions of the ARMS were observed, namely the pillar height, pillar pitch, and first layer thickness as indicated in Figure 6.3.

Table 6.1: Acoustic properties of materials used in numerical simulation in k-Wave [15].

Material	Speed of sound (m/s)	Density (kg/m^3)	Acoustic impedance $(MRayl)$
Water	1480	1000	1.48
glass	5900	2200	1.045
air [16]	331	1.225	0.0004
PDMS [17]	1077	970	1.045
Polyethylene	1950	930	1.814
Polystyrene	2320	1040	2.413
Polylactic acid	2220	1240	2.753
Epoxy [18]	2650	1150	3.05
PMMA	2757	1190	3.28
SU-8 [19]	2917	1200	3.5
Melopas	2900	1700	4.93

6.2.3. CHOICE OF MATERIALS

In choosing the material used as Polymer 1, there are several considerations that have to be taken into account: (1) the acoustic impedance that is similar to water to minimize reflection, (2) the biocompatibility of the material to host cell cultures, (3) the compatibility of the polymer to microfabrication processes. Polydimethylsiloxane (PDMS) is widely used in organ-on-chip and microfluidics applications [20],[21], [22]. Due to its wide adoption, PDMS-based devices have demonstrated biocompatibility with various types of cultures [14]. Compatibility with microfabrication processes allows for electrodes to be deposited directly on the surface of PDMS [20]. Furthermore, the acoustic impedance of the material for polymer 1 is also an important consideration. Since the source-facing surface of the polymer is flat to accommodate cells and electrodes, reflection from this surface is inevitable, and therefore, it is important to minimize the reflection on this interface. In the case of PDMS, its acoustic impedance is similar to water (Table 6.1), and hence has a reflection coefficient of only 0.172 (Eq.2.3), which is far less than polystyrene and glass, with reflection coefficients of 0.24 and 0.795, respectively. Due to these combinations of properties, PDMS was chosen as the first layer of polymer. There are fewer constraints when choosing the material for the second layer of polymer. Since the second layer will not be in contact with the cell culture, biocompatibility is no longer a constraint. Therefore, several materials covering a range of acoustic properties were considered as the second layer of polymer. Table 6.1 contains the properties of the materials used in the simulation, including the polymers used as the second polymer layer. Limitations due to the fabrication have not yet been considered since there is a wide range of manufacturing techniques. Based on the result of the study, the fabrication process of the device can be adapted accordingly. Some polymers, such as polymethyl methacrylate (PMMA) and polylactic acid (PLA), can be deposited using additive manufacturing, while others, such as polystyrene (PS), low-density polyethylene (LDPE), and epoxy, can be shaped through the molding process. The efficacy of these polymers paired with PDMS as the first polymer layer was assessed through the simulation.

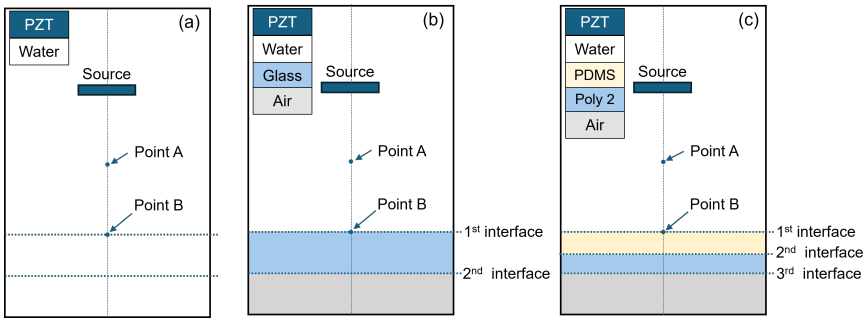

Figure 6.4: Schematic of the simulation setup in k-Wave: (a) echo-free simulation mimicking pressure field characterization of an ultrasound transducer, (b) simulation of ultrasound pressure field with a conventional substrate, and (c) simulation of ultrasound pressure field with a two-polymer stacked substrate.

6.2.4. SIMULATION SETUP OF REFERENCES

Assessment of the ARMS performance was compared to a set of references. The simulation of the references follows the setup shown in Figure 6.4. The first setup was to observe the propagation of waves generated by the transducer in a reflection-free environment (Figure 6.4(a)). This simulation represents the typical characterization condition of an ultrasound transducer. The second setup allowed the simulation of the propagation of waves in the presence of a single-layer material (Figure 6.4(b)). The influence of several materials commonly used as culture substrates on the propagation waves was assessed. The final simulation performed was the effect of stacking two layers of polymers without the use of ARMS to show the contribution of the structure (Figure 6.4(c)).

6.2.5. ASSESSMENT METRIC

Two assessment metrics were used, namely the deviation and the echo reduction. The deviation (Eq. 6.1) was calculated based on the measurement of Point B, which compares the difference in peak-to-peak amplitude of the stimulation signal to the expected stimulation signal.

$$Deviation\,(\%) = \left(\frac{|signal_{P2P,water} - signal_{P2P,measured}|}{signal_{P2P,water}} x100\%\right) \tag{6.1}$$

where $signal_{P2P,water}$ is the peak-to-peak amplitude of the expected stimulation signal measured in a reflection-free environment and $signal_{P2P,measured}$ is the peak-to-peak amplitude of the measured stimulation signal. Echo reduction (Eq. 6.2) shows the changes in echo amplitude compared to the glass reference measured at Point A.

$$Echo\,reduction\,(\%) = 100\% - \left(\frac{Echo_{P2P,measured}}{Echo_{P2P,glass}} x100\%\right) \tag{6.2}$$

where $Echo_{P2P,measured}$ is the peak-to-peak reflection amplitude of the measured configuration and $Echo_{P2P,glass}$ is the peak-to-peak reflection amplitude of the glass substrate.

6.3. SIMULATION RESULTS

6.3.1. REFERENCE SIMULATIONS

ECHO-FREE CONDITION

An echo-free simulation was performed following the simulation setup shown in Figure 6.4(a). As seen in Figure 6.5(a), a single burst of pressure was observed in both Point A and B, which originated from the single pulse applied to the source. The absence of reflected waves validated the effectiveness of the perfectly matched layer implemented on the boundary of the simulation space. The amplitude of the pulse shown in Point B indicates the stimulation signal amplitude that would be applied to the stimulation target on the surface of the substrate.

CONVENTIONAL SUBSTRATES

Substrates were introduced into the simulation space. Several substrate materials were used to see the effect of typical culture substrate material on the acoustic wave. Glass substrate is widely used as the culture substrate in MEA. It is also used in several dedicated ultrasound setups [11], [10]. The acoustic reflection coefficient of glass and water is around 0.796, which indicates that a significant amplitude of acoustic pressure will be reflected in this interface. This can be seen in Figure 6.5(a-b) which shows the pressure across time in Point A and Point B. The amplitude ratio between the incoming wave and the reflected wave in Point A followed the reflection coefficient of glass and water. On the other hand, the large reflection coefficient in the first interface resulted in a small amplitude of the wave being transmitted and reflected by the second interface. This resulted in the worst-case scenario where the energy in the reflection was being concentrated in the time domain. This effect also heavily impacted the stimulation signal on the surface of the substrate which experienced a large deviation from 3.43 to 6.05 amplitude (76.4% deviation).

Polystyrene is widely used in well plates, and it has a much lower reflection coefficient with water (0.240) compared to glass substrates. This results in the reflection amplitude being dominated by the second interface. As seen in Figure 6.5(c), the echo from the second interface was approximately 2 times larger than the first echo.

PDMS and PMMA are widely used as culture substrates in Organ-on-chip applications. As seen in Figure 6.5(d), PDMS has very good acoustic impedance matching with water, resulting in a small reflection amplitude from the first interface and minimum deviation of the stimulation signal. However, this caused the reflection at the second interface to be larger when compared to other substrates. Meanwhile, Figure 6.5(e) showed that PMMA showed a similar reflection pattern as polystyrene. Initial reflection was higher than polystyrene due to the slightly higher reflection coefficient followed by a lower echo from the second interface due to the less amplitude transmitted from the first interface.

STACKED SUBSTRATE

A two-layer polymer substrate represented a step closer to the proposed ARMS design (Figure 6.4(c)). Due to its acoustic properties, biocompatibility, and cleanroom compatibility, PDMS was selected as the top polymer layer in ARMS. As an example, Figure 6.5(f) shows the time-domain measurement at Points A and B of a PDMS-PMMA stack with a

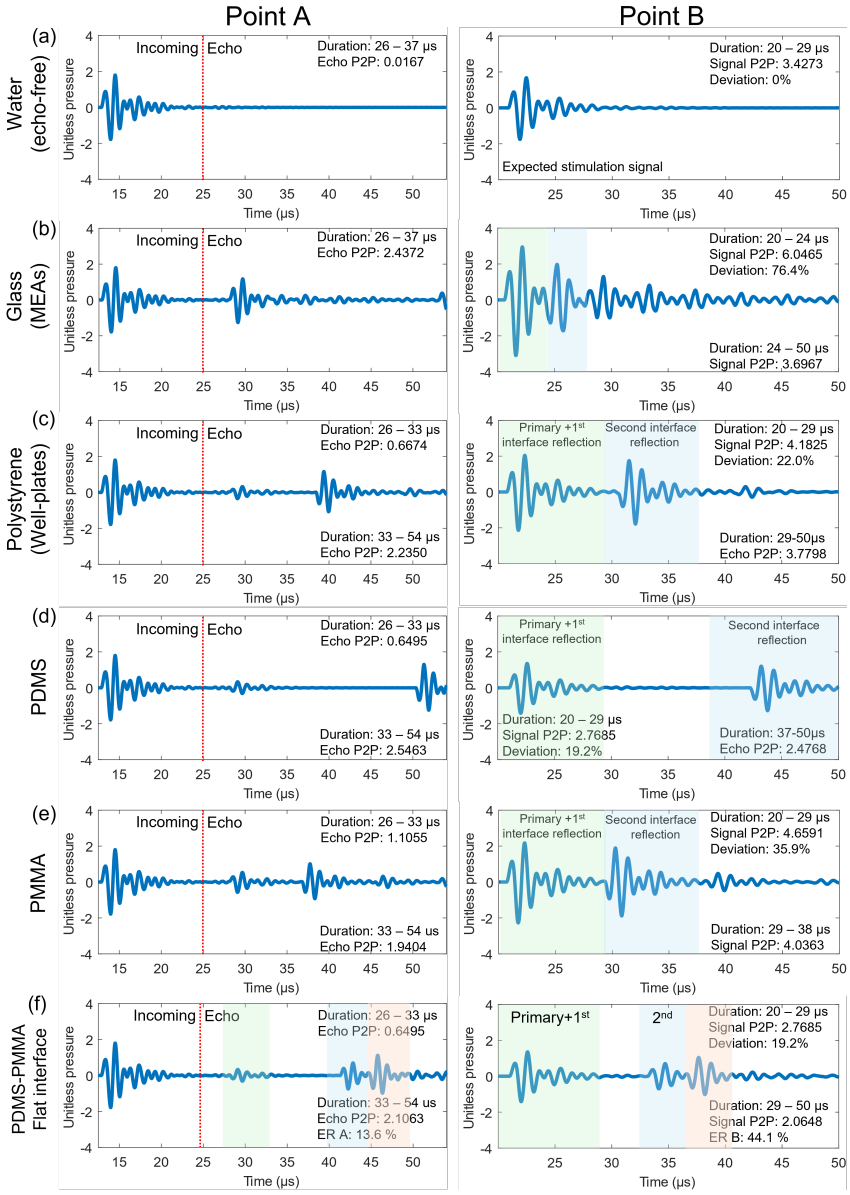

Figure 6.5: Time-domain simulation results comparing echo reduction and deviation performance under various substrate conditions at Point A and Point B. (a) Echo-free condition mimicking typical ultrasound characterization. Simulations with (b) glass, (c) polystyrene, (d) PDMS, and (e) PMMA substrates positioned in front of the transducer. (f) Simulation with a PDMS-PMMA stacked substrate.

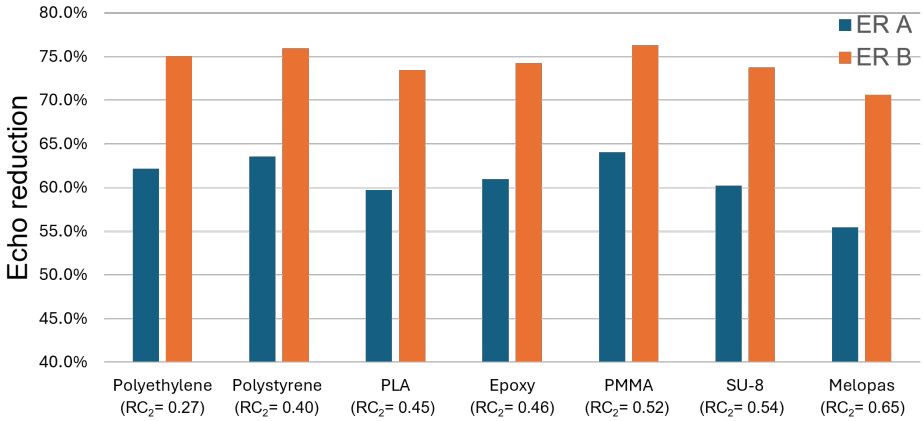

Figure 6.6: Comparison of echo reduction at Point A and Point B of ARMS with various absorbing polymer materials. The RC_2 indicates the reflection coefficient at the interface with PDMS.

flat interface. The PDMS layer was 7 mm thick, followed by a 5 mm PMMA layer. Additional reflection peaks were observed at both observation points. At Point A, reflections from each interface can be clearly distinguished. The reflection from the first interface at around 28 μs was followed by reflections from the second and third interfaces with a 13 μs delay, corresponding to the time needed for sound to travel 14 mm in PDMS. The first echo (highlighted in green) on the stacked substrate is solely determined by the reflection ratio of the first polymer layer. Compared to the single-layer PDMS substrate, the first echo of the stacked substrate was identical. This is also evident at Point B, where an identical deviation was seen with the PDMS substrate, as the stimulation signal at the surface is determined by the amplitude of the incoming wave and the echo from the first interface.

The increased number of interfaces facilitated a distribution of the reflection amplitude. At Point B, the amplitude of the reflection with a stacked substrate was markedly lower than with a single-layer substrate of PDMS and PMMA. Due to the high speed of sound in PMMA, a slight overlap also occurred between the second and third interface reflections in the stacked substrate. This overlap subsequently increased the amplitude of the echo from the third interface. Overall, the stacked substrate design demonstrates an improvement over the conventional single-layer substrate in terms of echo reduction.

6.3.2. OPTIMIZATION OF ARMS

MATERIAL SELECTION FOR THE SECOND LAYER OF POLYMER

The simulation of the ARMS was performed following the setup shown in Figure 6.3. Using this model, we compared the performance of ARMS with several material combinations, maintaining a fixed pillar height of 2 mm, a pitch of 10 mm, and a PDMS thickness of 5 mm. The materials tested as the absorbing layer are listed in Table 6.1. The list covers a range of acoustic properties, from low acoustic impedance materials, such as Polyethy-

lene, to high acoustic impedance materials, such as Melopas, which affect the reflection coefficient of the PDMS-Poly 2 interface (RC2). The performance of ARMS utilizing various absorbing polymers is illustrated in Figure 6.6. The effect of material selection on echo reduction performance appeared minimal, with the lowest reduction at 55.5% with Melopas and the highest at 64.1% with PMMA when observing Point A. This observation was further corroborated by an analytical approach that considered the three flat material interfaces, as seen in Figure 6.7(a). Considering the first-order reflection, the optimal point for minimizing the reflection amplitude occurred at RC2 = 0.5 as shown in Figure 6.7(b). The curve is relatively flat around this value, which is consistent with the ARMS results that show minimal changes in performance between the RC2 value of 0.25 and 0.7. The combination of PDMS and PMMA exhibited the highest echo reduction at both Point A and Point B, which serves as a starting point for further optimization in the dimensions of the ARMS structure.

THE EFFECT PDMS THICKNESS

As shown in Figure 6.8(b), the PDMS thickness was varied from 0.5 mm to 6 mm. The pillar height and pitch were fixed at 2 mm and 10 mm, respectively. Within the observed range, the performance of ARMS was largely independent of PDMS thickness as seen in Figure 6.8(a). The inclusion of propagation attenuation would affect the role of PDMS thickness, however, the model assumed elastic wave propagation. Therefore, the thickness of the PDMS can be kept to a minimum to maintain an overall thin substrate

THE EFFECT PITCH

The effect of the array pitch was optimized while keeping the PDMS thickness constant at 2 mm and the pillar height at 5 mm. The pitch of the ARMS was swept from 0.5 mm to 14 mm (Figure 6.9(b)), which corresponds to about 0.5λ to 14λ in PDMS at 1 MHz frequency. Figure 6.9(a) demonstrates that the array pitch significantly influences the performance of ARMS. At 1 MHz frequency, the optimum performance was achieved at a pitch of 10 mm. When interpolated, the echo reduction reached a performance above 40% between 3.9 mm to 11.64 mm pitch. At 2 MHz, the optimum performance was also achieved at a pitch of 10 mm. However, the echo reduction was less sensitive to the pitch,

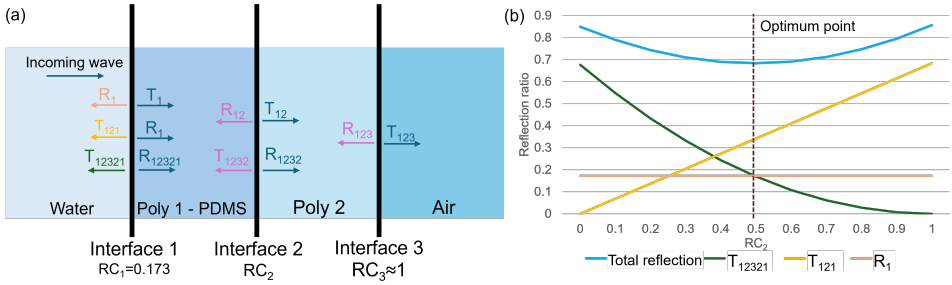

Figure 6.7: (a) A schematic of the acoustic reflection and transmission of water-PDMS-Polymer-air material stack. (b) A plot describing the sum and components of first-order reflection going back to the water medium as a function of reflection coefficient RC_2.

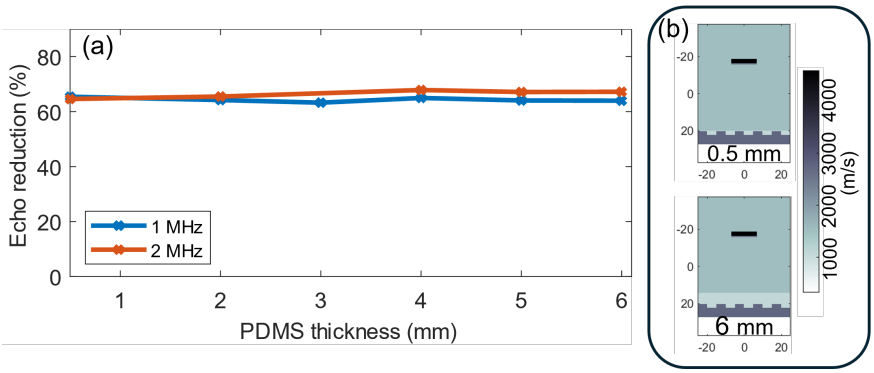

Figure 6.8: (a) The echo reduction of ARMS as a function of PDMS thickness. (b) The simulation setup used during the optimization of the PDMS thickness, the schematics indicate the material boundary by showing the speed of sound.

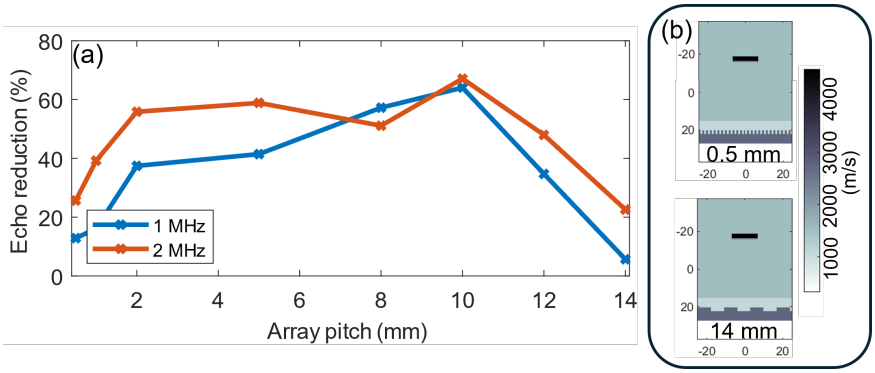

Figure 6.9: (a) The echo reduction of ARMS as a function of array pitch. (b) The simulation setup used during the optimization of the array pitch, the schematics indicate the material boundary by showing the speed of sound.

with ARMS performance going above 40% at array pitches between 1.05 mm and 12.63 mm. Performance decreased sharply at pitches below 2 mm and above 10 mm. At very small and large pitches, the interface between the two materials more closely resembles a flat surface, potentially explaining the reduction in echo reduction performance.

THE EFFECT PILLAR HEIGHT

The pillar height was optimized while keeping the PDMS thickness constant at 2 mm and the array pitch at 10 mm. The pillar height was swept from 0.5 mm to 6.5 mm (Figure 6.10(b)). Within the observed range, echo reduction and pillar height exhibited a positive correlation as seen in Figure 6.10(a). The echo reduction ranged from 52.8% to 65.8% between the shortest and tallest pillar heights. This positive correlation is likely due to the increased number of reflections caused by taller pillars. The correlation was more pronounced at 1 MHz than at 2 MHz ultrasound frequency. Within the observed range, the optimal pillar thickness was 4 mm and 6 mm at 1 MHz and 2 MHz frequen-

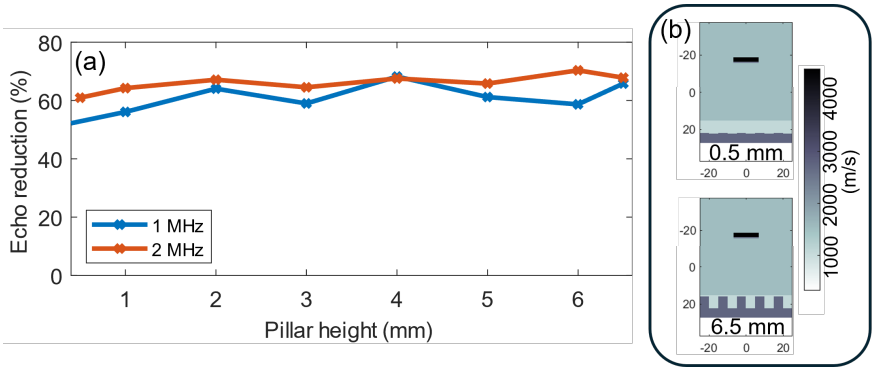

Figure 6.10: (a) The echo reduction of ARMS as a function of pillar height. (b) The simulation setup used during the optimization of the pillar height, the schematics indicate the material boundary by showing the speed of sound.

cies, respectively. Thus, increasing pillar height generally improves echo reduction, with the optimal height depending on the ultrasound frequency.

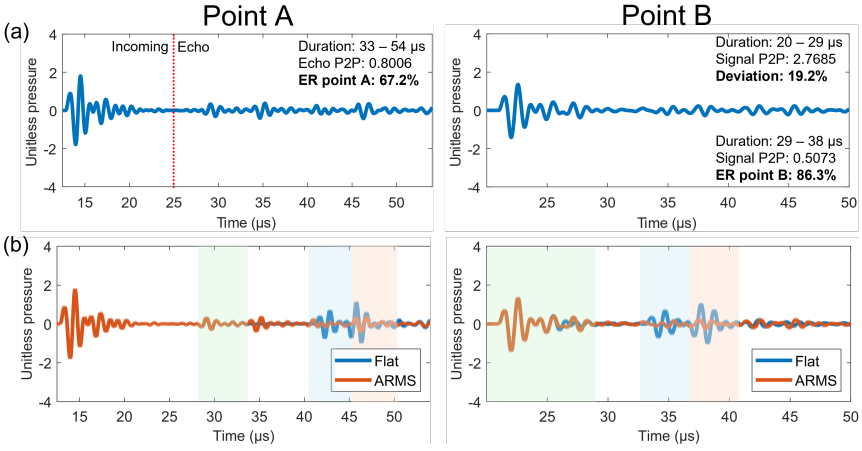

Figure 6.11: (a) The time domain simulation result at Point A and Point B of the optimized ARMS. (b) comparison of the simulation result of PDMS-PMMA stack with optimized ARMS and a flat interface.

6.3.3. OPTIMIZED ARMS

To evaluate the performance of the optimized ARMS design, a simulation was conducted with a PDMS and PMMA stack, 2 mm pillar thickness, 5 mm PDMS thickness, and 10 mm array pitch. The resulting time-domain simulation results at Point A and B are shown in Figure 6.11(a). The performance of the optimized ARMS was compared to that of conventional substrates, including glass, PS, PDMS, and PMMA. As seen in Figure 6.12, the ARMS significantly reduced reflection amplitude in both Point A and B compared

to these substrates. Compared to a glass substrate, the optimized ARMs demonstrated echo reductions of 67.2% and 86.3% at Point A and Point B, respectively. The deviation of stimulation signal on the surface of the substrate was substantially improved, decreasing from 76.4% in glass to 19.2% with ARMS. Compared to a stacked substrate of PDMS and PMMA with flat interface of the same thickness, the effect of ARMS structure can clearly be seen in Figure 6.11(b), where the configuration with a flat interface only exhibited an echo reduction of 13.6% at Point A and 44.1% at Point B. The ARMS optimized for 1 MHz ultrasound frequency was also tested with incident waves up to 8 MHz. ARMS maintained an echo reduction above 50% and a deviation below 23% across this frequency range, demonstrating its potential effectiveness for a variety of ultrasound neuromodulation applications.

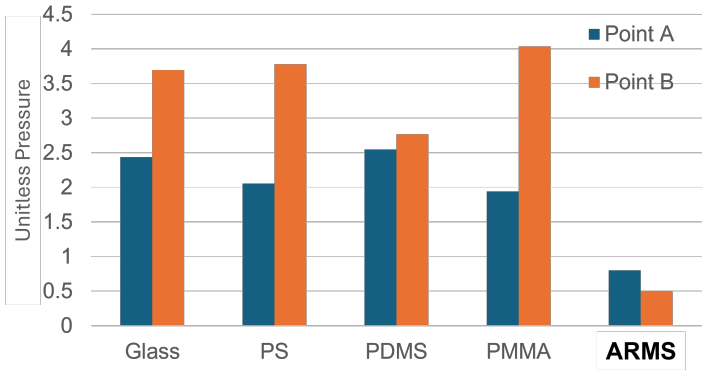

Figure 6.12: Comparison of echo amplitudes at Point A and Point B for conventional substrates (glass, polystyrene, PDMS, PMMA) and an optimized ARMS (PDMS-PMMA) demonstrating significant echo reduction achieved with the optimized ARMS.

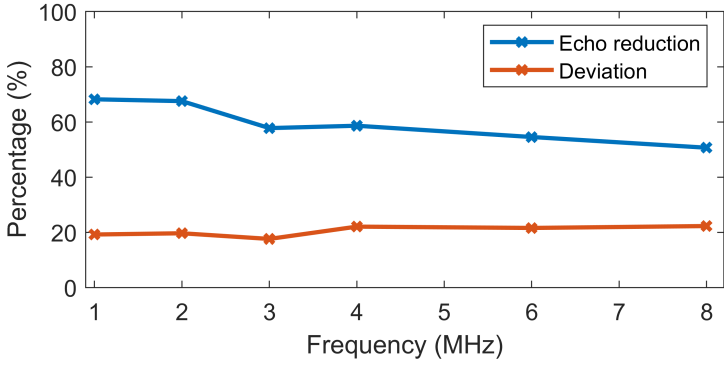

Figure 6.13: The performance of ARMS optimized at 1 MHZ in terms of Echo reduction at Point A and the stimulation amplitude deviation on the substrate surface at different incident frequencies.

6.4. CONCLUSION

This study demonstrated through simulation the potential of ARMS to reduce the reflection in an in vitro ultrasound neuromodulation study, which can help to improve the preservation of stimulation fidelity. The concept can be applied to typical in vitro platforms such as microplates and MEAs, therefore offering more versatility than the state-of-the-art concept [9]. The ARMS design was optimized for 1 MHz and 2 MHz ultrasound frequencies, which found that the combination of PDMS and PMMA yielded the best performance in terms of echo reduction and stimulation signal preservation. Optimization was also performed on the dimensions of the array of pillars, especially in terms of pillar height and pitch. The optimized ARMS was shown to reduce the amplitude of the echo on the surface of the substrate by 86.3% compared to a glass substrate and preserved stimulation signal fidelity with a deviation of 19.2%, a significant improvement from the 76.4% deviation observed on a glass substrate. Incorporating material attenuation into the simulation setup can improve accuracy and is expected to further enhance ARMS performance by attenuating the echo within the polymer. Given the promising simulation results, experimental validation is necessary to confirm the concept's viability. Experimental measurements would also allow for the exploration of composite polymers, which could further enhance ARMS performance but are difficult to simulate.

BIBLIOGRAPHY

[1] G. K. Wardhana, T. L. Costa, and M. Mastrangeli, "Anti-reflective microengineered substrate for in vitro ultrasound neuromodulation", in *Proceedings of 2024 IEEE Ultrasonics, Ferroelectrics, and Frequency Control Joint Symposium (UFFC-JS)*, IEEE, Sep. 2024, pp. 1–4, ISBN: 979-8-3503-7190-1. DOI: 10.1109/UFFC-JS60046.2024.10793577.

[2] J. Blackmore, S. Shrivastava, J. Sallet, C. Butler, and R. Cleveland, "Ultrasound neuromodulation: A review of results, mechanisms and safety", *Ultrasound in Medicine and Biology*, vol. 45, 7 2019, ISSN: 0301-5629. DOI: 10.1016/j.ultrasmedbio.2018.12.015.

[3] H. A. Kamimura, A. Conti, N. Toschi, and E. E. Konofagou, "Ultrasound neuromodulation: Mechanisms and the potential of multimodal stimulation for neuronal function assessment", *Frontiers in Physics*, vol. 8, 2020, ISSN: 2296424X. DOI: 10.3389/fphy.2020.00150.

[4] M. Saccher, S. Kawasaki, M. P. Onori, G. M. van Woerden, V. Giagka, and R. Dekker, "Focused ultrasound neuromodulation on a multiwell mea", *Bioelectronic Medicine*, vol. 8, 1 Dec. 2022, ISSN: 23328886. DOI: 10.1186/s42234-021-00083-7.

[5] I. M. Suarez-Castellanos, E. Dossi, J. Vion-Bailly, *et al.*, "Spatio-temporal characterization of causal electrophysiological activity stimulated by single pulse focused ultrasound: An ex vivo study on hippocampal brain slices", *Journal of Neural Engineering*, vol. 18, 2 Apr. 2021, ISSN: 17412552. DOI: 10.1088/1741-2552/abdfb1.

[6] H. B. Kim, K. M. Swanberg, H. S. Han, *et al.*, "Prolonged stimulation with low-intensity ultrasound induces delayed increases in spontaneous hippocampal culture spiking activity", *Journal of Neuroscience Research*, vol. 95, 3 2017, ISSN: 10974547. DOI: 10.1002/jnr.23845.

[7] H.-S. Han, S. Y. Hwang, F. Akram, *et al.*, "Neural activity modulation via ultrasound stimulation measured on multi-channel electrodes", in *World Congress on Engineering 2014*, Newswood Limited : International Association of Engineers, Jul. 2014, p. 1538, ISBN: 9789881925275.

[8] W. Secomski, K. Bilmin, T. Kujawska, A. Nowicki, P. Grieb, and P. A. Lewin, "In vitro ultrasound experiments: Standing wave and multiple reflections influence on the outcome", *Ultrasonics*, vol. 77, pp. 203–213, May 2017, ISSN: 0041624X. DOI: 10.1016/j.ultras.2017.02.008.

[9] S. Yoo, D. R. Mittelstein, R. C. Hurt, J. Lacroix, and M. G. Shapiro, "Focused ultrasound excites cortical neurons via mechanosensitive calcium accumulation and ion channel amplification", *Nature Communications*, vol. 13, 1 Dec. 2022, ISSN: 20411723. DOI: 10.1038/s41467-022-28040-1.

[10] K. Lee, J. M. Lee, T. T. Phan, C. J. Lee, J. M. Park, and J. Park, "Ultrasonocoverslip: In-vitro platform for high-throughput assay of cell type-specific neuromodulation with ultra-low-intensity ultrasound stimulation", *Brain Stimulation*, Aug. 2023, ISSN: 1935-861X. DOI: 10.1016/J.BRS.2023.08.002.

[11] P. S. Balasubramanian, A. Singh, C. Xu, and A. Lal, "Ghz ultrasonic chip-scale device induces ion channel stimulation in human neural cells", *Scientific Reports*, vol. 10, 1 Dec. 2020, ISSN: 20452322. DOI: 10.1038/s41598-020-58133-0.

[12] H. Bai, Z. Zhan, J. Liu, and Z. Ren, "From local structure to overall performance: An overview on the design of an acoustic coating", *Materials*, vol. 12, 16 Aug. 2019, ISSN: 19961944. DOI: 10.3390/ma12162509.

[13] D. Zhao, H. Zhao, H. Yang, and J. Wen, "Optimization and mechanism of acoustic absorption of alberich coatings on a steel plate in water", *Applied Acoustics*, vol. 140, pp. 183–187, Nov. 2018, ISSN: 1872910X. DOI: 10.1016/j.apacoust.2018.05.027.

[14] G. Singh, A. Mishra, A. Mathur, *et al.*, "Advancement of organ-on-chip towards next generation medical technology", *Biosensors and Bioelectronics: X*, vol. 18, Jun. 2024, ISSN: 25901370. DOI: 10.1016/j.biosx.2024.100480.

[15] A. R. Selfridge, "Approximate material properties in isotropic materials", *IEEE Transactions on Sonics and Ultrasonics*, 3 1985.

[16] H. Shankar and P. S. Pagel, "Potential adverse ultrasound-related biological effects: A critical review", *Anesthesiology*, vol. 115, pp. 1109–1124, 5 2011, ISSN: 15281175. DOI: 10.1097/ALN.0b013e31822fd1f1.

[17] N. N. Liu, Y. D. Cui, B. C. Khoo, and A. M. Zhang, "Damage characteristics of elastic material through a thin membrane using high-intensity focused ultrasound (hifu)", *AIP Advances*, vol. 8, 11 Nov. 2018, ISSN: 21583226. DOI: 10.1063/1.5050432.

[18] Y. Wang, J. Tao, F. Guo, *et al.*, "Magnesium alloy matching layer for high-performance transducer applications", *Sensors (Switzerland)*, vol. 18, 12 Dec. 2018, ISSN: 14248220. DOI: 10.3390/s18124424.

[19] A. Ndieguene, P. Campistron, J. Carlier, S. Wang, D. Callens-Debavelaere, and B. Nongaillard, "Su-8 photoresist and su-8 based nanocomposites for broadband acoustical matching at 1 ghz", in *Journal of Physics: Conference Series*, vol. 195, Institute of Physics Publishing, 2009. DOI: 10.1088/1742-6596/195/1/012005.

[20] H. Aydogmus, M. Hu, L. Ivancevic, *et al.*, "An organ-on-chip device with integrated charge sensors and recording microelectrodes", *Scientific Reports*, vol. 13, 1 Dec. 2023, ISSN: 20452322. DOI: 10.1038/s41598-023-34786-5.

[21] N. Gaio, B. van Meer, W. Q. Solano, *et al.*, "Cytostretch, an organ-on-chip platform", *Micromachines*, vol. 7, 7 Jul. 2016, ISSN: 2072666X. DOI: 10.3390/mi7070120.

[22] C. J. Mandrycky, C. C. Howard, S. G. Rayner, Y. J. Shin, and Y. Zheng, "Organ-on-a-chip systems for vascular biology", *Journal of Molecular and Cellular Cardiology*, vol. 159, pp. 1–13, Oct. 2021, ISSN: 10958584. DOI: 10.1016/j.yjmcc.2021.06.002.

7

Conclusion

If you eventually end up as a dust,
you may as well live like a stardust;
bearing someone else's dream.

Momiyama Kenji

7.1. CONCLUSION

The work presented in this thesis aims to address technological challenges in design, interconnection and interfacing for piezoelectric ultrasound transducer, specifically for *in vitro* neuromodulation studies. The following section summarizes the key contributions of this work.

INTEGRATED AIR BACKING LAYER ON SILICON SUBSTRATE

A novel approach to improve the transmit efficiency of piezoelectric ultrasound transducers (PUTs) integrated on silicon by incorporating an air-backing layer within the silicon substrate was demonstrated. This integrated air-backing is achieved through microfabrication techniques, selectively thinning the silicon substrate beneath the transducers to create a suspended membrane. Key to this achievement is the trade-off between improved output intensity and mechanical stability, optimized at a membrane thickness of 20 μm. This optimized design demonstrated a significant improvement in output intensity (average factor of 5.11 at 8.5 MHz) compared to transducers on a standard 300 μm silicon substrate. Even when accounting for shifts in resonance frequency, the air-backed transducers showed a notable enhancement (average factor of 2.65) at their respective resonance frequencies. The integrated air-backing layer shows promise for enhancing the efficiency of PUTs-on-ASIC for ultrasound neuromodulation.

POLYMER METAL CONNECTION

A novel polymer-metal connection (PMC) method for ultrasound transducers to optimize transmit efficiency was developed. This approach utilizes a microfabricated PDMS /Ti/Al membrane supported by a silicon frame, replacing traditional top connections like thick aluminum foil. The key finding is the significant improvement in preserved output intensity (80%) compared to an ideal reference, contrasting with the state-of-the-art aluminum foil connection, which only achieves 22.5%. The PMC was successfully implemented on a 2x2 transducer array and validated through preliminary biological testing, demonstrating its ability to stimulate neuronal and endothelial cells.

FRESNEL PHASING ZONE PLATE

An acoustic lens with high focal gain by utilizing FPZP made from PDMS was realized. The PDMS-FPZP is advantageous over other lens type due to the thin form-factor which minimize attenuation.The lens was fabricated using single photolithography step which offer cost-effective and reliable way to focus ultrasound wave with different parameters such as frequency and focal distance. A COMSOL Multiphysics model was developed to aid the design of the lens, which was shown to successfully predict the performance of the fabricated lens.Notably, the focusing achieved by the PDMS-FPZP demonstrated a focal gain of 19.95 dB and a high focusing resolution with FWHM of 0.25 mm and FDHM of 3.2 mm.

ANTI-REFLECTIVE MICROENGINEERED STRUCTURE

The potential of ARMS to preserve the fidelity of stimulation signal in an *in vitro* ultrasound neuromodulation studies by reducing the reflection coming from the substrate was demonstrated through simulation. The study shows the optimization of ARMS design in the choice of material and structure dimensions. ARMS significantly reduced

echo coming from the substrate compared to the conventional glass substrate. The ARMS demonstrated 86.3% echo reduction compared to a glass substrate and preserved the stimulation signal on the surface with 19.2% deviation.

7.2. FUTURE WORK

INTEGRATED AIR BACKING LAYER ON SILICON SUBSTRATE

- While CMOS IC thinning without compromising electronics performance has been demonstrated, further investigation is needed to assess the compatibility of ultrasound transducer integration with thinned substrates. The integration process can involve high-stress processes, such as dicing and the use of pressure-sensitive adhesives, which may pose challenges for thinned substrates.

POLYMER METAL CONNECTION

- The use of PMC presents a novel concept for implementing top metal connections using microfabricated structures. While many CMOS implementations utilize a common ground to simplify top-side connections, microfabrication enables patterning of the PMC metal layer. Instead of a single ground connection, multiple vias can create addressable top elements, facilitating row-column array implementation, which can reduce connection routing complexity and increase the number of elements within an array.
- The scalability of the PMC design, particularly for miniaturization, should be investigated to assess its applicability across different size constraints.
- Incorporating a matching layer beneath the PDMS could further enhance performance. However, careful consideration must be given to material selection and deposition techniques to ensure compatibility with the fabrication process and to avoid compromising the mechanical integrity of the membrane.

FRESNEL PHASING ZONE PLATE

- The use of PDMS for FPZP fabrication shows promising results in terms of efficiency and ease of fabrication. The size of the structure used in this study is still far from the limit of the photolithography process. Therefore, a lens for higher frequency ultrasound can still be achieved, which can push the spatial resolution of the focusing even further.
- The same fabrication approach can be applied with 3D-printed molds to create FPZPs for lower frequencies, potentially benefiting from rapid prototyping and lower production costs.
- Given the demonstrated capability of non-zero focusing angles in simulation, experimental validation of this approach would be valuable. This could provide an alternative method for steerable ultrasound focusing by actuating the lens structure, potentially circumventing the need for expensive IC development associated with phased array transducers. Such steerable focusing could be valuable in applications like ultrasound imaging and therapy, where precise control of the focal point is crucial.

ANTI-REFLECTIVE MICROENGINEERED STRUCTURE

- ARMS addresses a primary challenge in *in vitro* ultrasound studies, including but not limited to ultrasound neuromodulation. While simulations have shown promising results, experimental validation of the ARMS concept is still needed. This validation may present fabrication challenges but also allows for the exploration of micro-/nanoparticle fillers and porous materials that are difficult to simulate, similar to the non-homogeneous materials used in anechoic tiles. These materials could further enhance the echo reduction capabilities of ARMS by increasing acoustic absorption and scattering.

- In addition to reducing substrate echo, incorporating in the same substrate an acoustic sensing element could enable better prediction of actual stimulation parameters or even a close-loop control of the stimulation, improving the quality of stimulus-response in ultrasound neuromodulation studies.

A

APPENDIX A: FABRICATION FLOWCHARTS

A.1. AIR-BACKED SUBSTRATE FABRICATION FLOWCHART

ALIGNMENT MARKERS

- Starting material: 4-inch double-sided-polished p-type silicon wafer <100> with thickness of 300 μm.
- Lithography for alignment markers
  - Spin coating: EVG120; HMDS; SPR3012; 1.4-μm thick.
  - Exposure: ASML PAS 5500/80; COMURK Mask; 140 mJ/cm^2.
  - Development: EVG120; PEB 90 secs at 115°C ; 60 secs MF322 developer; HB 90 secs at 100°C.
- Etching of alignment markers: Trikon Omega 201; silicon etching; URK_NPD; 120 nm deep.
- Cleaning procedure - silicon line:
  - Plasma ashing: TePla; 1000 W; end-point detection.
  - Organic cleaning: 10 minutes of HNO_3 100% at ambient temperature.
  - Rinsing: Quick Dump Rinser; until water resistivity is 5 $M\Omega$.
  - Metal Cleaning: 10 minutes of HNO_3 65% at 110°C.
  - Rinsing: Quick Dump Rinser; until water resistivity is 5 $M\Omega$.
  - Drying: Avenger Ultra Pure Rinser Dryer.

INTERCONNECTS FABRICATION

- PECVD silicon oxide deposition; Novellus PECVD reactor; 2 μm thickness at 400°C.
- Aluminum deposition; Trikon Sigma Sputter Coater; AlSi 400 nm at room temperature.
- Lithography for aluminum interconnects:
  - Spin coating: EVG120; HMDS; SPR3012; 2.1-μm thick.
  - Exposure: SUSS Microtec MA/BA8 Mask Aligner; 155 mJ/cm^2.
  - Development: EVG120; PEB 90 secs at 115°C ; 60 secs MF322 developer; HB 90 secs at 100°C.
- Plasma etching of aluminum; Trikon Omega 201; aluminum etching; Al04_350; 400 nm deep.
- Cleaning procedure - green metal line:
  - Plasma ashing: TePla; 1000 W; end-point detection.
  - Organic cleaning: 10 minutes of HNO_3 100% at ambient temperature.
  - Rinsing: Quick Dump Rinser; until water resistivity is 5 $M\Omega$.
  - Drying: Avenger Ultra Pure Rinser Dryer.

PASSIVATION AND CONTACT OPENINGS

- PECVD silicon oxide deposition; Novellus PECVD reactor; 400 nm thickness at 400°C.
- Lithography for contact openings:
  - Spin coating: EVG120; HMDS; SPR3012; 2.1-μm thick.
  - Exposure: SUSS Microtec MA/BA8 Mask Aligner; 155 mJ/cm^2.
  - Development: EVG120; PEB 90 secs at 115°C ; 60 secs MF322 developer; HB 90 secs at 100°C.
- wet etching of silicon oxide: 1 min of Triton x-100 surfactant; BHF (7:1); 3 minutes etch time.
- Rinsing: Quick Dump Rinser; until water resistivity is 5 $M\Omega$.
- Cleaning procedure - green metal line:
  - Plasma ashing: TePla; 1000 W; end-point detection.
  - Organic cleaning: 10 minutes of HNO_3 100% at ambient temperature.
  - Rinsing: Quick Dump Rinser; until water resistivity is 5 $M\Omega$.
  - Drying: Avenger Ultra Pure Rinser Dryer.

SILICON CAVITY FABRICATION

- Lithography for silicon etching on the backside of the wafer:
  - Spin coating: Manual; HMDS; AZ-12XT-20PL-10; 8 μm thick.
  - Exposure: SUSS Microtec MA/BA8 Mask Aligner; 50 seconds exposure time.
  - Development: EVG120; PEB 90 secs at 115°C ; 2x60 secs MF322 developer; HB 90 secs at 100°C.
- Silicon etching: SPTS Omega Rapier; $0\text{EKL}_s mooth_2 0C_x x; etchratei s 0.9\mu m/$ loop; depth can be adjusted.
- Cleaning procedure - green metal line:
  - Plasma ashing: TePla; 1000 W; end-point detection.
  - Organic cleaning: 10 minutes of HNO_3 100% at ambient temperature.
  - Rinsing: Quick Dump Rinser; until water resistivity is 5 $M\Omega$.
  - Drying: Avenger Ultra Pure Rinser Dryer.

PZT MOUNTING AND PASSIVATION

- Dicing: wafer is diced into 3x3 cm^2 dies.
- Cavity seal: glass cover slip is placed on top of the silicon cavity on the back of the wafer; EPO-TEK 301-2FL is used to bond the two surface; Epoxy is dispensed using pneumatic dispenser; curing for 3 hours at 80°C.
- PZT placement: PZT is placed on top of contact pads; EPO-TEK H20e is used to electrically connect the PZT to the pads; curing for 3 hours at 80°C.
- Wire bonding; 50-μm diameter Tungsten wire placed on the contact pads and the top of the PZT; EPO-TEK H20e is used to create electrical connection; curing for 3 hours at 80°C.
- Passivation using Parylene-C: SCS Labcoater 3; 5 μm target thickness.

A

A.2. POLYMER METAL CONNECTION FABRICATION FLOWCHART

WAFER THINNING

- Starting material: 4-inch double-sided-polished p-type silicon wafer <100>; wafer thickness is adjusted to the thickness of the PZT; for 8 MHz PZT (270 μm) a 300-μm-thick wafer is used.
- Thinning of silicon wafer: SPTS Omega Rapier; $0EKL_s mooth_2 0C_x x; etchrate is 0.9 \mu m/$ loop; target etch depth is 50 mum.
- Cleaning procedure - silicon line:
  - Plasma ashing: TePla; 1000 W; end-point detection.
  - Organic cleaning: 10 minutes of HNO_3 100% at ambient temperature.
  - Rinsing: Quick Dump Rinser; until water resistivity is 5 $M\Omega$.
  - Metal Cleaning: 10 minutes of HNO_3 65% at 110°C.
  - Rinsing: Quick Dump Rinser; until water resistivity is 5 $M\Omega$.
  - Drying: Avenger Ultra Pure Rinser Dryer.

DEPOSITION OF LAYERS

- PECVD silicon oxide deposition as landing layer: Novellus PECVD reactor; 4000 nm thickness at 400°C.
- AlSi deposition (400 nm) followed by Ti deposition (50 nm): Trikon Sigma Sputter Coater; AlSi_400nm_Ti_50nm_50C; deposition temperature of 50°C.
- Cleaning procedure - green metal line:
  - Plasma ashing: TePla; 1000 W; end-point detection.
  - Organic cleaning: 10 minutes of HNO_3 100% at ambient temperature.
  - Rinsing: Quick Dump Rinser; until water resistivity is 5 $M\Omega$.
  - Drying: Avenger Ultra Pure Rinser Dryer.

SILICON REMOVAL

- Lithography for silicon etching on the backside of the wafer:
  - Spin coating: Manual; HMDS; AZ-12XT-20PL-10; 8-μm thick.
  - Exposure: SUSS Microtec MA/BA8 Mask Aligner; 50 seconds exposure time.
  - Development: EVG120; PEB 90 secs at 115°C ; 2x60 secs MF322 developer; HB 90 secs at 100°C.
- Silicon etching: SPTS Omega Rapier; 1EKL_flat_bottom_20C; etch rate is 1.8 $\mu m/$ loop; etch until lands on silicon oxide with overetching (170 loops).

- Cleaning procedure - green metal line:
  - Plasma ashing: TePla; 1000 W; end-point detection; wafer is placed horizontally to prevent rupture of membrane.
  - Organic cleaning: 10 minutes of HNO_3 100% at ambient temperature.
  - Rinsing: Quick Dump Rinser; until water resistivity is 5 $M\Omega$.
  - Drying: Avenger Ultra Pure Rinser Dryer.
- PDMS deposition:
  - PDMS mixing and degassing; THinky ARE 250; Sylgard 184 10:1 weight ratio
  - Spin coating: Manual; Sylgard 184; 100-μm thick.
  - Baking: Memmert Oven; 1 hour at 90°C.

TEMPORARY SUPPORT REMOVAL

- Wet etching of silicon oxide: 1 min of Triton x-100 surfactant; BHF (7:1); 16 minutes etch time; perform electrical testing to confirm silicon oxide removal.
- Rinsing: Quick Dump Rinser; until water resistivity is 5 $M\Omega$.
- Dicing: wafer is diced into 22x22 mm^2 dies; membrane side is placed on the UV dicing foil to prevent rupture during dicing.

A

A.3. FRESNEL PHASING ZONE PLATE FABRICATION FLOWCHART

SILICON MOLD ETCHING

- Starting material: 4-inch single-sided-polished p-type silicon wafer <100> with thickness of 500 μm.
- PECVD silicon oxide deposition; Novellus PECVD reactor; 2 μm thickness at 400°C.
- Lithography for silicon etching:
  - Spin coating: EVG120; HMDS; AZ nLOF2020; 3.5-μm thick.
  - Exposure: SUSS Microtec MA/BA8 Mask Aligner; 155 mJ/cm^2.
  - Development: EVG120; x-link bake 60 secs at 110°C ; 120 secs MF322 developer; HB 90 secs at 100°C.
- Wet etching of silicon oxide: 1 min of Triton x-100 surfactant; BHF (7:1); 8 minutes etch time.
- Rinsing: Quick Dump Rinser; until water resistivity is 5 $M\Omega$.
- Silicon etching: SPTS Omega Rapier; 1EKL_flat_bottom_20C; etch rate is 1.8 μm/loop; target depth is 100 μm.
- Plasma ashing: TePla; 1000 W; end-point detection.
- wet etching of silicon oxide: 1 min of Triton x-100 surfactant; BHF (7:1); 8 minutes etch time.
- Rinsing: Quick Dump Rinser; until water resistivity is 5 $M\Omega$.
- Cleaning procedure - silicon line:
  - Plasma ashing: TePla; 1000 W; end-point detection.
  - Organic cleaning: 10 minutes of HNO_3 100% at ambient temperature.
  - Rinsing: Quick Dump Rinser; until water resistivity is 5 $M\Omega$.
  - Metal Cleaning: 10 minutes of HNO_3 65% at 110°C.
  - Rinsing: Quick Dump Rinser; until water resistivity is 5 $M\Omega$.
  - Drying: Avenger Ultra Pure Rinser Dryer.

PDMS MOLDING

- C_4F_8 deposition: SPTS Omega Rapier; EKL_FC_depo_xx.
- PDMS deposition:
  - PDMS mixing and degassing; THinky ARE 250; Sylgard 184 10:1 weight ratio
  - Spin coating: Manual; Sylgard 184; 100-μm thick.

  - Degassing: Vaccuum desiccator; 20 minutes.
  - Baking: Memmert Oven; 1 hour at 90°C.

- Lens Peeling: cut the edges of the lens with a sharp blade and peel using a tweezer while dispensing Isopropyl alcohol.

ACKNOWLEDGEMENTS

To say my PhD journey was unconventional would be a significant understatement. Between the pandemic that now seemed like a faraway memory came knocking just two months after the start of my contract, an unexpected building renovation due to a fire hazard, and a Cleanroom facility that can be closed down depending on where the wind blows, this journey was a like an odyssey, a trial by fire, that undeniably shaped me and one I will forever cherish. Much like the epic journeys of Odysseus or the characters in 'Journey to the West,' this adventure was never meant to be undertaken alone.

First and foremost, I could not imagine this journey without the involvement of the two distinguished gentlemen, Tiago and Massimo. The two became scientific role models. Revealing the multifaceted nature of a scientist. Massimo provided the bedrock, instilling in me the importance of scientific discipline. Tiago ignited my scientific passion and ambition to push boundaries. I am deeply grateful for the pivotal roles they played in this chapter of my life. While to them, I may be one student among many that is yet to come, I sincerely hope I've left a lasting impression in return.

For a significant portion of my life, the Bioelectronics section has been my academic home, evolving from my time as a Master's student to an honorary member, then back to a PhD candidate, and now, full circle, to honorary status once more. Over the past four years, the people in this section have been a constant presence in my life. They infused my challenging journey with laughter and curiosity, punctuated by memorable moments: 'kroketten' lunch meetings, fish lunches, movie nights, the BE day out, Christmas potlucks, and, of course, the BELCA festival. While these social events may seem numerous, they were a vital counterbalance to the inherent stress of a PhD. I extend my deepest gratitude to Wouter for welcoming me into this remarkable section. And to the members of the Bioelectronics group, whom I've had the pleasure of working alongside, I offer my sincere thanks: Vasso, Dante, Leon, Frans, Achilleas, Alessandro, Sampi, Gustavo, Kambiz, Samaneh, Merlin, Vivo, Marion, Esther, Kellen, Rosario, Amin, Anna, Can, Andra, Konstantina, Raphael, Gonzalo, Maria, Nerea, Samatha, Yihan, Rui, Brian, Tarique, Chris, Suman, Christos, Peng, Xiao, Bakr, Kimia, Arash, Niloufar, Johan, Ronald, Bea, Chunyan, Patricia, Patricija, Hsukang, Remy, Arnau, Niels van Lith, Christiaan, Joost, Chenyan, Masoumeh, Diogo, Eshani, Ignasi and Samuel.

A special thanks to my office mates: Ronaldo, for whom I still feel terrible about forgetting to water Chiquinha, your plant; Nasim, my go-to for engaging in socio-political discussions; Limitha, whose presence always brightened the office; and Liwen, my indispensable foodie companion. (Hopefully, the three of us can grab some hotpot again one day.)

I am also grateful to my paranymphs, Hassan and Cesc, my longest-standing colleagues and friends during my PhD. Cesc consistently pushed me beyond my comfort zone, and Hassan's trust in me to co-found a company is deeply appreciated.

One of the most rewarding aspects of my PhD journey was the opportunity to collaborate with exceptional students on their graduation projects. Each student brought unique perspectives and challenges, contributing significantly to my scientific growth in ways they may not fully realize. I extend my sincere gratitude to Niels Burghoorn (Swagger Niels), Reka Savundranayagam, Niels van Damme, Hidde Woerdman, and Eduardo Puchol Morejón for their invaluable contributions.

EKL cleanroom was indispensable to my research, and I would like to thank the current and past staff of EKL, Silvana, Tom, Mario, Johannes, Koos, Joost, Robert, Paolo, Burno, Aleksandar, Hitham, Mariana, Daniel, and Francesco. Although I sometimes complain about the long downtime of machines, I can certainly say that without their help, this thesis would not have been finished. I also extend my thanks to the people in the ECTM section, Shin and Marta, with who I had the pleasure of sharing conference trips and discussions on ultrasound, and Sten and Roberto, who are always helpful with troubleshooting problems in the cleanroom. The Organ-on-chip group, of which I had the pleasure of being part of: Clementine, Tim, Pratik, Alireza, Elena, Feyza, Friso, Ramón, Bram, and Bjorn. This group helped me grow in a field initially foreign to me during the start of my PhD. I expanded my horizons on creating devices that interface with biological tissue and learned diverse fabrication techniques.

My collaboration with Leiden University Medical Center—JP, Arn, Michel, Vasiliki, and Wendy—was a unique and enriching experience. I never imagined conducting biological experiments, especially with devices I had created. Witnessing the effects of ultrasound stimulation on neurons firsthand was remarkable. Their contributions made this project truly special, and I hope our collaboration yields further scientific fruits.

My time in the cleanroom was made infinitely more enjoyable by my cleanroom compatriots, Milica, Hande, and Paul. Their technical assistance, life rants, and welcoming coffee breaks were invaluable, as were the shared experiences at conferences, which always ended with a lot of drinks.

With my little time outside of the university, I was fortunate enough to have a little 'family' in the Netherlands, who reminded me of life beyond work and academia. My sincere thanks to Angel, Ayunda, Dimas, and Vendy for providing that vital balance. I couldn't imagine having better friends, especially through the challenges of the pandemic.

To my family, my Mom and Dad, thank you for your unwavering patience with my career choices, even if they remain a mystery to you. In retrospect, you shaped my worldview and made me who I am today. Thank you to Tasha, my steadfast supporter since childhood, and to Thania, whose courage continues to inspire me. Finally, words cannot express my gratitude to Melani, who made countless sacrifices to support me throughout this thesis. The long workdays, delayed life plans, and missed vacations—your unwavering support made this achievement possible. I hope to repay your sacrifices in the next chapters of our life.

Gandhika K. Wardhana

List of Publications

Patent

- **G.K. Wardhana**, H. Rivandi, T.L. Costa, "*Electrical Pulser for a Load Having a capacitance,*" patent pending, 2024

Journal publications

- **G.K. Wardhana**, N.J. Burghoorn, M. Mastrangeli, T.L. Costa, "*Silicon-integrated Piezoelectric Focused Ultrasound Transducers with PDMS-based Phasing Fresnel Lens for in vitro Ultrasound Neuromodulation,*" submitted to TechRxiv.

- C. Van Damme, **G.K. Wardhana**, A.l. Velea, V. Giagka, T.L. Costa, "*Feasibility Study for a High-Frequency Flexible Ultrasonic Cuff for High-Precision Vagus Nerve Ultrasound Neuromodulation,*" IEEE Transactions on Ultrasonics, Ferroelectrics, and Frequency Control, vol. 71, no. 7, pp. 745-756, July 2024, doi: 10.1109/TUFFC.2024.3381923.

- S. Desmarais, H.j. Woerdman, **G.K. Wardhana**, T.L. Costa, "*A Novel Flexible Ultrasound Neurostimulator featuring a pitch-matched 2D array,*" in preparation.

Conference proceedings

- **G.K. Wardhana**, T.L. Costa, M. Mastrangeli, "*Anti-Reflective Microengineered Substrate for In vitro Ultrasound Neuromodulation* ," Proceedings of 2024 IEEE Ultrasonics, Ferroelectrics, and Frequency Control Joint Symposium, Taipei, Taiwan, 2024.

- **G.K. Wardhana**, T.L. Costa, M. Mastrangeli, "*An Acoustically Transparent Electrical Cap for Piezoelectric Ultrasound Transducers on Silicon,*" Proceedings of XXXV EUROSENSORS Conference, Lecce, Italy, 2023.

- **G.K. Wardhana**,M. Mastrangeli, T.L. Costa, "*Maximization of Transmitted Acoustic Intensity from Silicon Integrated Piezoelectric Ultrasound Transducers,*" Proceedings of 2022 IEEE International Ultrasound Symposium, Venice, Italy, 2022.

Conference contributions

- H. Rivandi, **G.K. Wardhana**, E. Sarkar, M. Aqamolaei, S. Desmarais, T.L. Costa, "*Miniaturized and Conformable Focused Ultrasound Neurostimulators,*" Proceedings of Bioelectronics Interfaces: Materials, Devices and Applications (CyBioEl), Limassol, Cyprus, 2024.

- N.J. Burghoorn, **G.K. Wardhana**, A.J.W. Hartel, T.L. Costa, "*Integrated Lipid Bilayer Membranes for Investigating Biophysical Mechanisms of Ultrasound Neuromodulation*," 2022 International Symposium on Biomolecular Ultrasound & Sonogenetics (ISBUS), Pasadena, California, 2022.

- **G.K. Wardhana**, M. Hu, J.P. Frimat, A.M.J.M Van den Maagdenberg, T.L. Costa, M. Mastrangeli, "*A Brain-on-chip Platform to Study the Optimal Parameters of Ultrasound Neuromodulation*," 2022 EUROoCS conference, Grenoble, France, 2022.

- **G.K. Wardhana**, M. Mastrangeli, T.L. Costa, "*Brain-on-Chip Platform for Studying the Optimum Parameters of Ultrasound Neuromodulation*," MRS Spring Meeting 2022, Honolulu, Hawaii, 2022.

- **G.K. Wardhana**, T.L. Costa, M. Mastrangeli, W.A. Serdijn, "*Brain-on-chip Platform to Study the Optimal Parameters of Ultrasound Neuromodulation*," BioEl 2022 winter school, Kirchberg in Tirol, Austria, 2022.